

WL-TR-95-4081

Engine Hybrid Ceramic Bearings



M. Rhoads and Dr. M. Bashyam

**GE Aircraft Engines
One Neumann Way
Cincinnati, OH 45215-6301**

November 1994

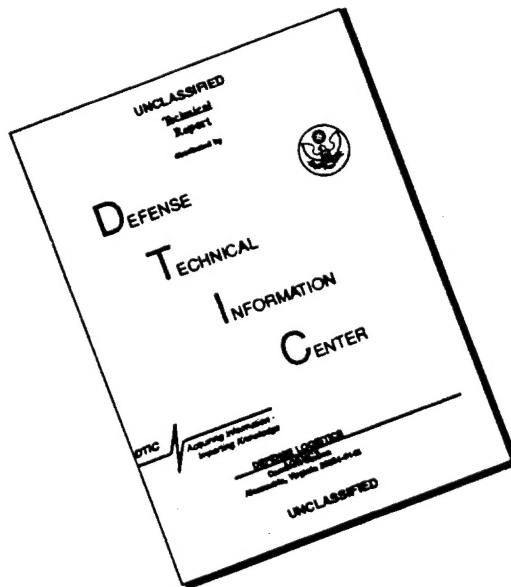
Final Report for the Period 23 May 1992 – 23 November 1994

Approved for public release; distribution unlimited

19961028 049

**Materials Directorate
Wright Laboratory
Air Force Materiel Command
Wright-Patterson AFB, OH 45433-7251**

DISCLAIMER NOTICE



THIS DOCUMENT IS BEST
QUALITY AVAILABLE. THE COPY
FURNISHED TO DTIC CONTAINED
A SIGNIFICANT NUMBER OF
PAGES WHICH DO NOT
REPRODUCE LEGIBLY.

NOTICE

When government drawings, specifications, or other data are used for any purpose other than in connection with a definitely related government procurement operation, the United States Government thereby incurs no responsibility nor any obligation whatsoever; and the fact that the government may have formulated, furnished, or in any way supplied the said drawings, specifications, or other data, is not to be regarded by implication or otherwise as in any manner licensing the holder or any other person or corporation, or conveying any rights or permission to manufacture, use, or sell any patented invention that may in any way be related thereto.

This report is releasable to the National Technical Information Service (NTIS). At NTIS, it will be available to the general public, including foreign nations.

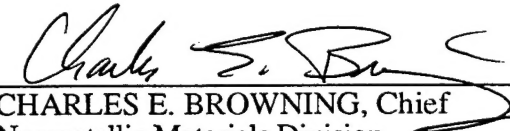
This technical report has been reviewed and is approved for publication.



KARL R. MECKLENBURG, Project Engineer
Nonstructural Materials Branch
Nonmetallic Materials Division



KENT J. EISENTRAUT, Chief
Nonstructural Materials Branch
Nonmetallic Materials Division



CHARLES E. BROWNING, Chief
Nonmetallic Materials Division
Materials Directorate

If your address has changed, if you wish to be removed from our mailing list, or if the addressee is no longer employed by your organization, please notify WL/MLBT, Bldg 654, 2941 P Street, Suite 1, Wright-Patterson AFB OH 45433-7750 to help maintain a current mailing list.

Copies of this report should not be returned unless return is required by security considerations, contractual obligations, or notice on a specific document.

REPORT DOCUMENTATION PAGE			Form Approved OMB No. 0704-0188
<p>Public reporting burden for this collection of information is estimated to average 1 hour per response, including the time for reviewing instructions, searching existing data sources, gathering and maintaining the data needed, and completing and reviewing the collection of information. Send comments regarding this burden estimate or any other aspect of this collection of information, including suggestions for reducing this burden, to Washington Headquarters Services, Directorate for Information Operations and Reports, 1215 Jefferson Davis Highway, Suite 1204, Arlington, VA 22202-4302, and to the Office of Management and Budget, Paperwork Reduction Project (0704-0188), Washington, DC 20503.</p>			
1. AGENCY USE ONLY (Leave Blank)	2. REPORT DATE	3. REPORT TYPE AND DATES COVERED	
	November 1994	Final Report; 23 May 1992 – 23 November 1994	
4. TITLE AND SUBTITLE		5. FUNDING NUMBERS	
Engine Hybrid Ceramic Bearings		C F33615-92-C-5926	PE 62712
		PR 8355	TA 00
		WU 08	
6. AUTHOR(S)		8. PERFORMING ORGANIZATION REPORT NUMBER	
M. Rhoads, Dr. M. Bashyam		R94AEB276	
7. PERFORMING ORGANIZATION NAME(S) AND ADDRESS(ES)		10. SPONSORING/MONITORING AGENCY REPORT NUMBER	
GE Aircraft Engines One Neumann Way Cincinnati, OH 45215-6301		WL-TR-95-4081	
9. SPONSORING/MONITORING AGENCY NAME(S) AND ADDRESS(ES)		11. SUPPLEMENTARY NOTES	
Materials Directorate Wright Laboratory/MLBT Air Force Materiel Command Wright-Patterson Air Force Base, OH 45433-7750			
12a. DISTRIBUTION/AVAILABILITY STATEMENT		12b. DISTRIBUTION CODE	
APPROVED FOR PUBLIC RELEASE; DISTRIBUTION IS UNLIMITED			
13. ABSTRACT (Maximum 200 words)			
<p>The objective of this program was the development of additional performance data and condition-monitoring techniques for silicon nitride (Si_3N_4) bearings. Induced-defect testing was performed to assess the ability of silicon nitride balls to withstand the high shock loads experienced during the growth of a race spall. The defect was placed in the outer ring of a hybrid bearing. Conclusions were made as to the survivability of ceramic balls under such severe conditions. High-speed thermal performance was compared between an all-steel bearing, a hybrid with the same internal geometry, and a hybrid with tightened internal geometry to lower the hertzian contact stress. Conclusions were made as to whether the hybrid bearings offer any improvement in thermal performance over an all-steel bearing. A condition-monitoring methodology was developed for early detection of an impending bearing failure. A technique was developed to find both metallic and ceramic debris from bearings. A monitoring device was developed, constructed, and demonstrated.</p>			
14. SUBJECT TERMS			15. NUMBER OF PAGES
Hybrid bearing; ceramic bearing; rolling elements; electrical-discharge machining; EDM; induced-defect testing; condition monitoring; high speed			117
			16. PRICE CODE
17. SECURITY CLASSIFICATION OF REPORT	18. SECURITY CLASSIFICATION OF THIS PAGE	19. SECURITY CLASSIFICATION OF ABSTRACT	20. LIMITATION OF ABSTRACT
Unclassified	Unclassified	Unclassified	SAR

NSN 7540-01-280-5500

Standard Form 298 (Rev. 2-89) Prescribed
by ANSI Std. Z39-18298-102

Contents

	<u>Page</u>
1.0 Summary	1
2.0 Introduction	2
3.0 Task 1 – Induced-Defect Testing	3
3.1 Objective	3
3.2 Test Procedure	3
3.3 Results and Discussion	4
3.3.1 Test 1 Results	4
3.3.2 Test 2 Results	10
3.3.3 Test 3 Results	10
3.3.4 Test 4 Results	13
3.4 Bearing Debris Analysis	20
3.5 Task 1 Conclusions	23
3.6 Recommendations for Future Tests	23
4.0 Task 2 – High-Speed Testing	24
4.1 Objective	24
4.2 Test Procedure	24
4.3 Results and Discussion	24
4.3.1 All-Steel Bearing (P04) Data, Points 1 – 36	24
4.3.2 Open-Curvature Hybrid Bearing (P05) Data, Points 37 – 72	29
4.3.3 Tight-Curvature Hybrid Bearing (P06) Data, Points 73 – 90	31
4.3.4 Reduced Oil-Flow Rate Data (P04 and P05), Points 91 Through 101	37
4.4 Task 2 Conclusions	41
4.5 Recommendations	41
5.0 Task 3 – Bearing Condition Monitoring	43
5.1 Objective	43
5.2 Technology Assessment	43
5.3 Risk-Reduction Experiments	44
5.4 Selection of Prototypes	44
5.5 Prototype 1 Evaluation: UT Device	45
5.5.1 Overview of Technique	45
5.5.2 Description and Operation	45
5.5.3 Experiments	48
5.6 Prototype 2 Evaluation: Infrared Photoelectric Sensing (IR)	52
5.6.1 Overview	52
5.6.2 Experiments	53
5.7 Decision Analysis (Technique for Bearing Rig)	57
5.8 Fourth Induced-Defect Bearing Test/Prototype Demonstration	58
5.8.1 Preliminary Results	58
5.8.2 Final Results	60
5.9 Other Bearing Condition-Monitoring Devices Evaluated	60
5.9.1 Philtec (Fiber-Optic Bearing Monitor)	60
5.9.2 SKF Device	60

Table of Contents (Concluded)

	<u>Page</u>
5.10 Task 3 Conclusions	60
5.11 Recommendations for Future Work	62
6.0 Overall Program Conclusions	63
6.1 Task 1	63
6.2 Task 2	63
6.3 Task 3	63
7.0 References	64
Appendix A – Task 2 High-Speed Test Data	65
Appendix B – Ceramic-Chip Detector Technology Selection Matrix	72
Appendix C – Ultrasonic Scattering by Ceramic Debris in Oil	75
Introduction	75
Ultrasonic Scattering Calculations	75
Experimental Measurements	78
Summary	79
Appendix D – Radioisotopic Detection of Si₃N₄ Bearing Chips	82
Objective	82
Isotopic Labelling	82
Feasibility	83
Conclusions	85
Appendix E – Risk-Reduction Experiments	86
Effect of Mesh Material on UT	86
UT Attenuation of New and Used Oil	86
Sensitivity of IR	87
IR Attenuation of New and Used Oil	89
Appendix F – SKF Condition-Monitoring Application	90
History	90
Introduction	90
Measurement Theory	90
Results	92
General Conclusions	92
Measurement Results Overview	92
Bearing Defect Frequencies at 8,700 RPM	94
Bearing Defect Frequencies at 14,100 RPM	94
Bearing Defect Frequencies at 14,250 RPM	95
Bearing Defect Frequencies at 14,800 RPM	95
Gearmesh Frequencies at 8,700 RPM	96
Gearmesh Frequencies at 14,100 RPM	96
Gearmesh Frequencies at 14,250 RPM	96
Gearmesh Frequencies at 14,800 RPM	97
GE Ceramic Test Bearing Dimensions (Test RFM L 275669)	97
Test Cycle Conditions	97
Examples of Spectrums	97

List of Illustrations

Figure	Title	Page
1.	EDM Notch in Outer Race, Used to Initiate Spalling in a Short Time	3
2.	Control Console for Induced-Defect Tests	5
3.	Barrel-Type Rig Used for Induced-Defect Testing of Large Hybrid Bearings ...	5
4.	Pretest Hybrid Bearing with Cerbec NBD-200 Silicon Nitride Balls and AISI M50NiL Races	6
5.	Cage with Integral Cerbec NBD-200 Silicon Nitride Balls in the Pretest Condition	6
6.	Typical Failure Mode of an All-Steel Bearing	7
7.	M50 Ball with Minor Distress from Induced-Defect Test	7
8.	M50 Ball with Moderate Distress from Induced-Defect Test	8
9.	M50 Ball with Significant Distress from Induced-Defect Test	8
10.	Posttest Bearing Components from Induced-Defect Test 1	9
11.	Spall in Outer Race	9
12.	Typical Condition of Silicon Nitride Ball After Completion of the First Induced-Defect Test	10
13.	Components from the Second Induced-Defect Test	11
14.	Cage and all 20 Balls from the Second Induced-Defect Test	11
15.	Spalled Area on Ball from Second Induced-Defect Test	12
16.	SEM Photo of Spalled Area on Ball from Second Induced-Defect Test	12
17.	Typical Condition of 19 Unspalled Balls After Second Induced-Defect Test	13
18.	Components from the Third Induced-Defect Test	14
19.	Fractured Cage with all 20 Silicon Nitride Balls from Third Induced-Defect Test	14
20.	Spalled Outer Race	15
21.	One of the Three Silicon Nitride Balls from Test 3 that Experienced Minor Surface Distress	15
22.	Second of Three Balls to Suffer Minor Surface Distress in Third Induced-Defect Test	16
23.	Third of Three Balls to Show Surface Distress	16
24.	SEM Photo of Spalled Area on Ball from Third Induced-Defect Test	17
25.	Components from Fourth Induced-Defect Test	17
26.	Fractured Cage from Fourth Induced-Defect Test	18

List of Illustrations (Continued)

Figure	Title	Page
27.	Five Balls that Spalled During the Fourth Induced-Defect Test	18
28.	SEM Photo of Spalled Area on Ball from Fourth Induced-Defect Test	19
29.	Outer Ring with Spall Initiating at the EDM Notch	19
30.	Debris Caught in the Chip Collector During the Final Induced-Defect Test	20
31.	SEM Photo of Representative Chips from Figure 30	21
32.	Nonmagnetic Debris Caught in Chip Collector During Final Induced-Defect Test	21
33.	Silicon Nitride Chip from Final Induced-Defect Test	22
34.	Silicon Nitride Chip from Final Induced-Defect Test	22
35.	Silicon Nitride Chip from Final Induced-Defect Test	23
36.	ITBC's 120-mm Bearing Test Machine	25
37.	Control Panel of 120-mm Bearing Test Machine at ITBC	25
38.	Schematic of 120-mm Bearing Test Rig	26
39.	Bearing P04 Outer-Ring Temperature as a Function of Shaft Speed	26
40.	Bearing P04 Rig Power Consumption as a Function of Shaft Speed	28
41.	Bearing P04 Separator Speed Ratio as a Function of Shaft Speed	28
42.	All-Steel 120-mm Bore Bearing After Completion of 36 Test Points	29
43.	Bearing P05 Outer-Ring Temperature as a Function of Shaft Speed	31
44.	Bearing P05 Rig Power Consumption as a Function of Shaft Speed	32
45.	Bearing P05 Separator Speed Ratio as a Function of Shaft Speed	32
46.	Hybrid Bearing with Silicon Nitride Balls After Completion of Test Points 37 Through 72	33
47.	Comparison of Bearing P05 and P06 Outer-Ring Temperatures	34
48.	Comparison of Bearing P05 and P06 Rig Power Consumption	35
49.	Comparison of Bearing P05 and P06 Separator Speed Ratios	35
50.	Tight-Curvature Hybrid Bearing After Completion of Test Points 73 Through 90	36
51.	Historical Plot of Test Point 99 Variables	38
52.	Historical Plot of Test Point 101 Variables	38
53.	Hybrid Bearing with Silicon Nitride Balls (P05) After Completion of Test Points 91 Through 101	39
54.	Disassembled Bearing After Test Point 101	40

List of Illustrations (Continued)

Figure	Title	Page
55.	Inner Ring of P04 Bearing	40
56.	Cage from Bearing P04	42
57.	Assembled P04 Bearing After Completion of Test Point 101	42
58.	Schematic of UT System	45
59.	Engineering Drawing of UT System	46
60.	Chip Catcher	47
61.	Chip Injector and Chip Catcher Assembly	47
62.	Block Diagram of Lube System Used for Bench Testing	48
63.	Uncompensated Signal from the Screen at Various Test Conditions	50
64.	Ratio of Signal from the Screen to the Reference Signal for Various Test Conditions	50
65.	Sample Strip Chart Data Showing Reference and Screen Signals at 568 cm ³ /s (9 gpm) After 100 Chips Were Injected	51
66.	Schematic of IR Setup Showing Arrangement of Fiber-Optic Bundles and Location of the Chip Catcher	52
67.	Drawing of the Complete Flow Setup with the Chip Collector and IR Sensors ..	54
68.	Detection Capabilities of the IR Prototype for Various Flow Rates and Chip Counts	55
69.	IR Response from 20 Chips on Stainless Steel Screen at 568 cm ³ /s (9 gpm) as a Function of Oil Temperature	56
70.	IR Response from 20 Chips on Stainless Steel Screen at 568 cm ³ /s (9 gpm) as a Function of Oil Flow and Temperature	56
71.	Induced-Defect Chips on Chip Collector	61
72.	Induced-Defect Chips on Magnetic Plugs	61
73.	Calculated Scattering Amplitude of a 1-MHz Ultrasonic Frequency for Four Aspect Ratio Debris Particles	77
74.	Calculated Scattering Amplitude at a 5-MHz Frequency for Four Aspect Ratio Debris Particles	77
75.	Calculated Scattering Amplitudes Ratio at a 10-MHz Frequency for Three Aspect Ratio Particles	78
76.	Experimental Test Setup used to Measure Lubricant Attenuation	79
77.	New 7808K Lubricant: Ultrasonic Amplitude (0.2 V/Division) versus Time (5 μ s/division) for Measurement of Attenuation at 5 MHz	80
78.	New 7808J Lubricant: Ultrasonic Amplitude Verses Time at 5 MHz	80

List of Illustrations (Concluded)

Figure	Title	Page
79.	Used 7808J Lubricant: Ultrasonic Amplitude Versus Time	81
80.	Measured (Average of 10 Tests) Ultrasonic Attenuation at Different Frequencies for Three Aircraft Engine Lubricants	81
81.	Schematic of Sensor Concept	83
82.	UT Experiment	86
83.	Attenuation vs Frequency for New and Used Oil	88
84.	Schematic of Sensitivity Measurement	88
85.	Infrared Transmission vs Wavelength for New and Used Oil	89
86.	Single-Spectrum Plot: Frequency = 231.25, Amp = 6.0834 OV, Order = 0.933 ..	98
87.	Single-Spectrum Plot: Frequency = 2106.25, Amp = 5.5837 OV, Order = 8.776 ..	99
88.	Time Record Plot	100
89.	Single-Spectrum Plot: Frequency = 2037.50, Amp = 3.8027, Order = 8.820 ..	101
90.	Single-Spectrum Plot: Frequency = 2193.75, Amp = 6.3091, Order = 9.028 ..	102
91.	Single-Spectrum Plot: Frequency = 2103.75, Amp = 14.762	103
92.	Single-Spectrum Plot: Frequency = 105.00, Amp = 0.341	104
93.	Single-Spectrum Plot: Frequency = 240.00, Amp = 2.7647	105

List of Tables

Table	Title	Page
1.	Summary of Induced-Defect Testing.	20
2.	First 36 Points of 120-mm Bore Test, Bearing P04	27
3.	Test Points 37 through 72 of 120-mm Bore Test, Bearing P05	30
4.	Test Points 73 through 90 of 120-mm Bore Test, Bearing P06	33
5.	Test Points 91 through 104 of 120-mm Bore Test, Bearing P04 and P05	37
6.	UT Device Sample Test Results	48
7.	Effect of Air Injection on UT Detection Capability	49
8.	Performance of the UT Device when the Oil Temperature was Varied	51
9.	Sample Data from IR Prototype	53
10.	Results of Aeration Test with the IR Prototype	53
11.	“Must Have” Criteria for Prototype Testing	57
12.	“Wants” for Prototype Testing	57
13.	Summary of Results from Fourth Induced-Defect Test	59
14.	Thermal, Cage Speed, and Power Data for All-Steel Bearing (P04)	66
15.	Thermal, Cage Speed, and Power Data for Hybrid Bearing (P05)	67
16.	Thermal, Cage Speed, and Power Data for Tight Hybrid Bearing (P06)	68
17.	Thermal, Cage Speed, and Power Data for All-Steel and Hybrid Bearings (P04 and P05)	68
18.	Test Data for All-Steel Bearing (P04)	69
19.	Test Data for Hybrid Bearing (P05)	70
20.	Test Data for Tight Hybrid Bearing (P06)	71
21.	Test Data for All-Steel and Hybrid Bearings (P04 and P05)	71
22.	Ceramic-Chip Detector Technology Selection Matrix	73
23.	Loss of Reflection Due to Irregular Scatterers in Ultrasonic Beam	87
24.	CCD Response	87
25.	Maximum Acceleration, Acceleration Enveloping, and SEE Measurements for Eight Different Cycles	93

Nomenclature

AFBMA	Anti-Friction Bearing Manufacturers Association
AISI	American Iron and Steel Institute
ARPA	Advanced Research Projects Agency
CCD	Ceramic-chip detector
DOE	Design of experiments
DTIC	Defense Technical Information Center
ECD	Electronic chip detector
EDM	Electrical-discharge machined
EHD	Elastohydrodynamic (lubricant)
FFT	Fast Fourier transform
GEAE	GE Aircraft Engines
HD	Hydrodynamic
HPSN	Hot-pressed silicon nitride
Hybrid bearing	Bearing with ceramic rolling elements and steel races
IR	Infrared (test method)
ITBC	Industrial Tectonics Bearing Corporation
LED	Light-emitting diode
M50	Bearing material
M50NiL	Bearing material (case-hardened, fracture-tough tool steel)
Man-rated engine	An engine used on aircraft used to transport humans
MDN	Bearing speed measured by bore diameter in mm \times speed in rpm (millions)
MRC	Marlin Rockwell Company
OR	Outer race
ORC	Outer-race coolant (cooling)
RMS	Root mean square
SEE	Spectral emitted energy
SEM	Scanning electron microscope
SKF	SKF Condition Monitoring; corporate entity affiliated with MRC
SR	Ratio of screen signal to reference signal
TDC	Thin dense chrome
UT	Ultrasonic test method
V/L	Volume % of liquid in an air + liquid mixture

Preface

The authors acknowledge the many contributors and supporters to this program. They include Bill Crecelius (General Motors) for his genuine interest and guidance throughout this program, Eric Schueler (Ford Motor) for his support in the induced-defect and condition-monitoring parts of this program, Malcom Ashby for laying the groundwork for the condition-monitoring task, Roger Madden for all his support in the Component Test area, Dave Kroeger for all his support with the posttest bearing documentation, and the late Ted Atkinson for his leadership and enthusiasm for advanced bearing technologies. All of the above contributed at one time or another to advancement of bearing material technologies and had an influence on this program.

Appreciation is also given to Hans R. Signer and Stanley Pinel of ITBC for great support of the high-speed testing effort (Task 2).

Special thanks go to Dr. Haydn N.G. Wadley of the University of Virginia for his support and guidance in the areas of radioactive doping and ultrasonic debris monitoring in oils (Task 3).

Thanks also go to André Smulders of SKF Condition Monitoring for his contributions to bearing health monitoring during the final induced-defect test; to Dr. Richard Menzies, Mike Johnson, and John Clark of GEAE; and to Mike Price of GE Medical Systems for continued interest and guidance throughout the entire program and for always interjecting a dose of reality when it was needed.

Finally, the authors thank Karl Mecklenburg of WPAFB for his continued enthusiastic support which made doing all of this not only important but also fun.

1.0 Summary

GE Aircraft Engines (GEAE), under a contract from the Advanced Research Projects Agency (ARPA) and administered by the Materials Directorate of Wright Laboratory, Wright-Patterson Air Force Base, has demonstrated the ability of ceramic rolling elements to withstand shock-loading conditions experienced during race spalling, performed a series of full-scale tests directed at showing the thermal benefit of large hybrid (ceramic balls with steel races) bearings at speeds up to 3.0 MDN, and developed a condition-monitoring device that detects both ceramic and metallic bearing debris. The details of the three Tasks are presented in this report.

Task 1 involved testing a hybrid bearing operating under severe shock-loading conditions, with comparisons to an all-steel bearing used in production engines. It was concluded from this testing that silicon nitride balls are capable of withstanding the high shock loads experienced during race spalling. It was further concluded that the failure mode and time to failure are similar to those of an all-steel bearing, and the silicon nitride balls exhibit no greater, and potentially less, distress from this condition than do AISI M50 balls.

Task 2 involved back-to-back comparison of an all-steel, high-speed bearing to a hybrid bearing of the same geometry and to a hybrid bearing of tighter race curvatures, showing differences between outer ring temperatures, power consumption, and cage kinematics of all-steel and hybrid bearings. It was concluded that the hybrid bearing offers an advantage when operating under reduced oil-flow conditions compared to the all-steel bearing, but under normal engine operating conditions the advantage is minimal.

Task 3 dealt with the bench testing of new condition-monitoring devices designed to collect and detect both ceramic and metallic debris. It has been shown that methods involving ultrasonic inspection of a debris-collection screen or vibration analysis can warn of impending failure in a hybrid bearing.

GEAE has prepared a supplement (Ref 1) presenting selected color photos corresponding to certain illustrations in this report. Figures represented in that supplement are indicated by the following notation in this document:

A color image is presented in Reference 1.

2.0 Introduction

Silicon nitride bearing materials have been under evaluation for several decades. The trend toward higher thrust-to-weight ratios in aircraft gas turbine engines has prompted the evaluation of these lightweight bearing materials. Additionally, as the speed of engines increases, centrifugal forces on the outer race from the rolling elements also increase, reducing rolling-contact fatigue (RCF) life and further supporting the use of lightweight rolling elements.

Numerous reports have been written over the last three decades on ceramic bearing materials. Most of the reports have concentrated on the relative RCF behavior of the ceramic materials, with comparison to bearing steels. Prior to the mid-1970's, most data on ceramic bearings or hybrid bearings were not overly encouraging due to the low RCF life and low reliability exhibited by these materials (Ref 2). Since that time, significant advances have been made in the field of ceramic bearing materials, most of them being with silicon nitride (Si_3N_4). Testing by Parker and Zaretsky (Ref 3), Wheildon et al. (Ref 4), and Valori (Ref 5) all reported significant improvements in the RCF resistance of silicon nitride.

Reddecliff and Valori (Ref 6), using a 35-mm bore angular-contact bearing, illustrated that the outer-race temperature of a hybrid and an all-steel bearing were essentially the same over a wide variation in speeds and oil-flow rates. Reddecliff also concluded that the lower thermal coefficient of expansion of the silicon nitride ball should result in longer survival time after lubricant interruption. The primary economic advantage of a hybrid bearing may reside in this longer survival time in an oil-off situation, especially in single-engine aircraft.

Element, rig, and engine tests demonstrated that hot-pressed silicon nitride (HPSN) materials make viable rolling elements in areas of high speed or extreme environments — as reported by Weinberg and Bersch (Ref 7).

Ebert (Ref 8) concluded that high-quality silicon nitride could provide fatigue life at least the same as that of steel bearings. He also illustrated the improvements in oil-out performance of a hybrid bearing, compared to an all-steel bearing, and the ability of the hybrid bearing to survive the high loads encountered during a blade-out simulation test. His results also indicated that silicon nitride damage propagation was slow, and no problems were encountered at speeds up to 3.4 MDN.

Nishihara et al. have shown that the primary factors affecting RCF life include metallic inclusion content, porosity, segregation, and surface defects from finishing techniques (Ref 9). Once again, it was concluded that the RCF life of ceramic rolling elements was equal to or greater than that of steel bearing material.

Although all of these papers have contributed significantly to the advancement of ceramic bearing knowledge, additional testing remained before these bearings could be considered for man-rated engines. These tests include: determining the ability of the ceramic rolling elements to withstand the high shock loads of a bearing undergoing race spalling, demonstrating the thermal benefits of a full-scale hybrid bearing, and evaluating new chip-detection techniques capable of sensing both steel and ceramic chips. Although SAE lists numerous oil-system monitoring techniques (Ref 10), most would not have the capability to detect silicon nitride chips on-line in an aircraft engine.

3.0 Task 1 – Induced-Defect Testing

3.1 Objective

Although hybrid and all-ceramic bearings have been evaluated over the last several decades, application in a man-rated engine will require successful passing of many key tollgates. One of these is that a slow and stable failure rate must be exhibited by a bearing undergoing distress. A hybrid bearing with relatively brittle Si_3N_4 rolling elements had to demonstrate ability to perform under severe loading conditions before it could be considered a viable candidate for a man-rated engine. Even if the balls have a fatigue life greater than that of AISI M50, the silicon nitride material must be able to tolerate, for reasonable periods of time, the high shock loads of a bearing undergoing spall growth. In other words, the silicon nitride rolling elements must not disintegrate when subjected to the early stages of bearing failure. It is of prime importance that the failure rate of the entire bearing be slow, increasing the probability of bearing failure detection before catastrophic failure occurs.

The purpose of this task was to evaluate a hybrid bearing of AISI M50NiL races (both inner and outer) and silicon nitride balls (Cerbec, NBD-200, Si_3N_4), under realistic shock-loading conditions, and determine if this critical criteria could be achieved. The configuration used in this task was a split-inner-ring, angular-contact bearing with a bore diameter of approximately 133 mm and containing twenty 22.2-mm (7/8-in) diameter balls. The balls used in this study were consistent with AFBMA Class 10 specifications. The cage used in this testing is a commonly used, silver-plated, AISI 4340 cage. The four bearings used in this task were manufactured by the Torrington Company.

3.2 Test Procedure

This task was performed by placing an artificial defect, an electrical-discharge machined (EDM) notch, 0.5-mm wide by 0.25-mm deep), as shown in Figure 1, across the outer race of a bearing (jet engine main-shaft size) and running the bearing through a series of simulated idle, takeoff, climb, and cruise conditions.

The purpose of the artificial defect is to accelerate the time to initial race spalling. Without an induced defect, it could take several thousand hours and a large expenditure just to start a spall. The

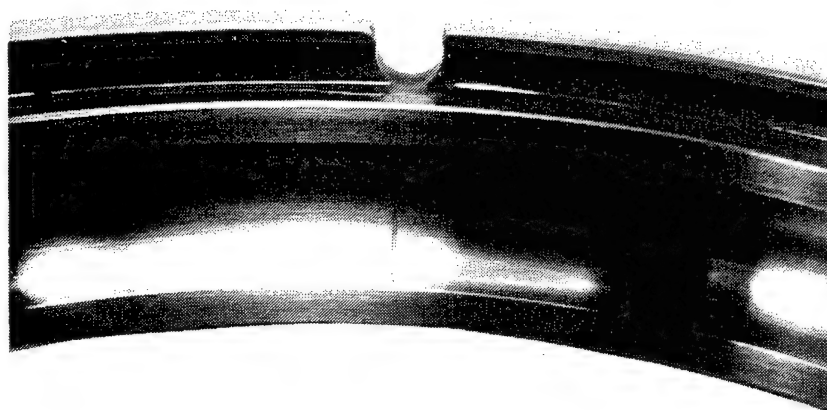


Figure 1. EDM Notch in Outer Race, Used to Initiate Spalling in a Short Time

cycle included axial loads of 4 kN (900 lbf) to 40 kN (9000 lbf) at speeds between 8,700 and 14,800 rpm (1.2 to 2.0 MDN). Each cycle represented a condition of idle, takeoff, climb, and cruise, and lasted for 30 minutes. The test bearings were lubricated with Mil-L-7808 synthetic engine oil, and lubrication was adequate to keep the operating temperature of the bearing between 121°C (250°F) and 149°C (300°F) during normal operation. This cycle was repeated until metal spall debris was detected with an electronic chip detector (ECD). This point, representing a time of $t = 0$, is when the first chance of detecting an impending bearing failure would occur with the ECD or commonly used magnetic plug. The test was then continued through the automatic 30-minute cycle until a preset operating condition (such as bearing outer ring temperature or rig power draw) was exceeded. Once the bearing ceased operation, it was disassembled, the components were examined, and the results were documented. The degree of success was determined by:

- a. the number of cycles the hybrid bearing was able to withstand after the initial race spall,
- b. a failure mode similarity to an all-steel bearing, and
- c. the condition of the silicon nitride balls after final failure.

3.3 Results and Discussion

Four induced-defect tests were performed within this task. Figures 2 and 3 show the typical control console and the barrel-type test rigs used in this set of experiments. Figures 4 and 5 show the as-received, pretested, hybrid bearing and the cage with the integral silicon nitride balls. All four tests were performed in the same manner, so a reasonable degree of confidence could be established about the data.

It's important to note that similar tests have been run with an all-steel bearing, and the typical failure mode is the cage splitting in half after approximately 50 cycles or greater (25 hours or greater) after the first indication of race spalling. Figure 6 shows a typical all-steel bearing failure mode from this type of induced-defect test. Note that the cage has been split in half, and at least one ball (as indicated by the white arrow) has sustained surface distress. The AISI M50 balls are often in various stages of distress, but it is not uncommon to have balls looking like those shown in Figures 7 (minor damage), 8 (moderate damage), and 9 (significant damage).

3.3.1 Test 1 Results

The first hybrid bearing test ran for a total of 43 cycles (21.5 hours) before the test rig automatically shut down due to an over-temperature condition. This test was not taken to complete lockup because it was desired to determine what condition the balls were in at some intermediate stage of failure. Upon disassembly, it was evident that the primary failure mode was that of cage fracture, and the balls appeared to be in relatively good condition. This is consistent with the mode of failure seen in the all-steel bearings in which the cage fractures due to the repeated pounding of the balls. After the cage separation, it generally wipes out the lube jets, causing the bearing to overheat and shut off the rig. Figure 10 shows the posttest bearing with the fractured cage. The spall in the outer race had initiated at the EDM notch and grown to a length of roughly 6.3 cm (2.5 in), as shown in Figure 11. Careful visual examination failed to reveal any signs of ball distress, and the balls looked as if they were new, as depicted in Figure 12. The test was terminated at this point since reassembly of a fractured cage with 20 loose balls was impractical.



A color image is presented in Reference 1.

Figure 2. Control Console for Induced-Defect Tests

A color image is presented in Reference 1.

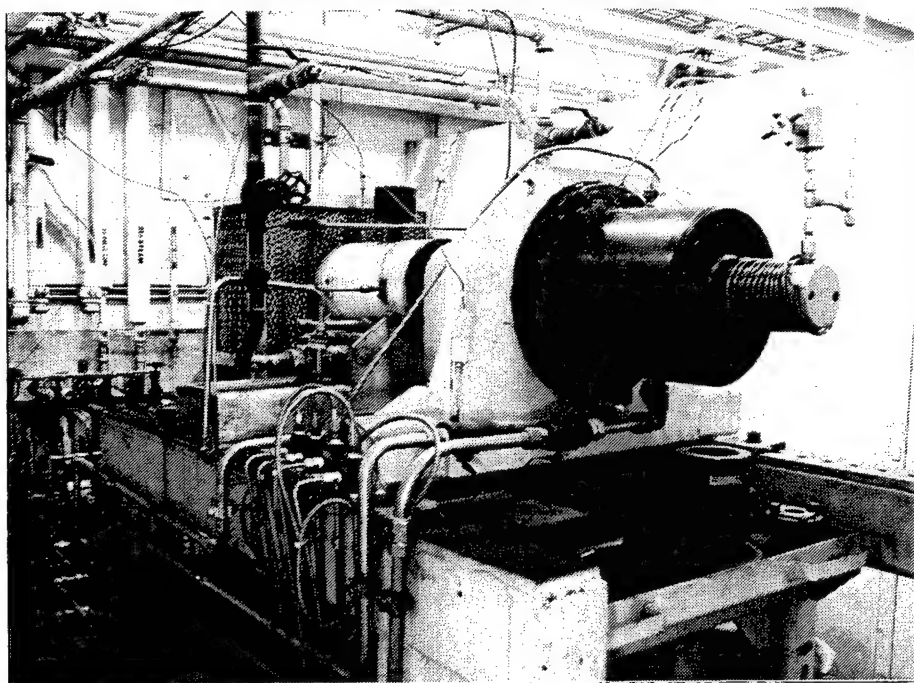


Figure 3. Barrel-Type Rig Used for Induced-Defect Testing of Large Hybrid Bearings

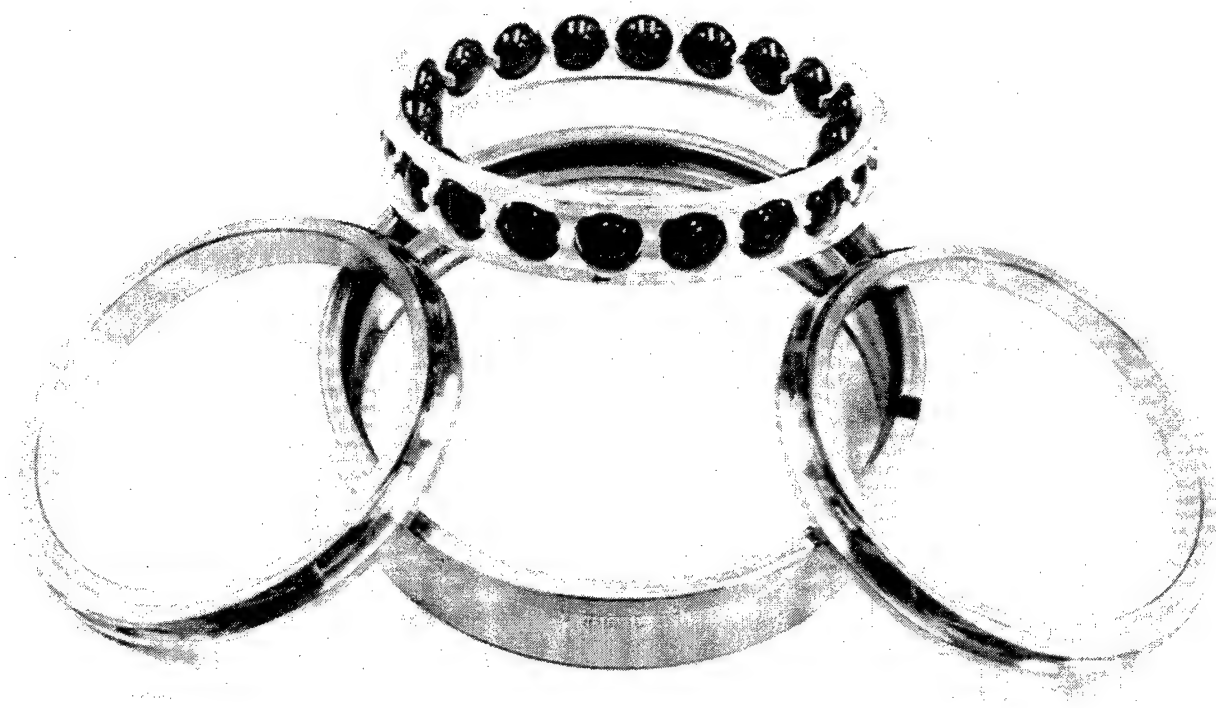


Figure 4. Pretest Hybrid Bearing with Cerbec NBD-200 Silicon Nitride Balls and AISI M50NiL Races

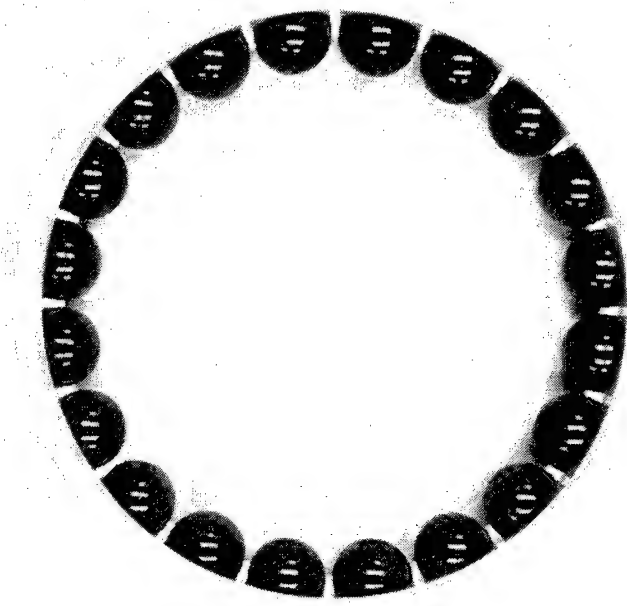


Figure 5. Cage with Integral Cerbec NBD-200 Silicon Nitride Balls in the Pretest Condition

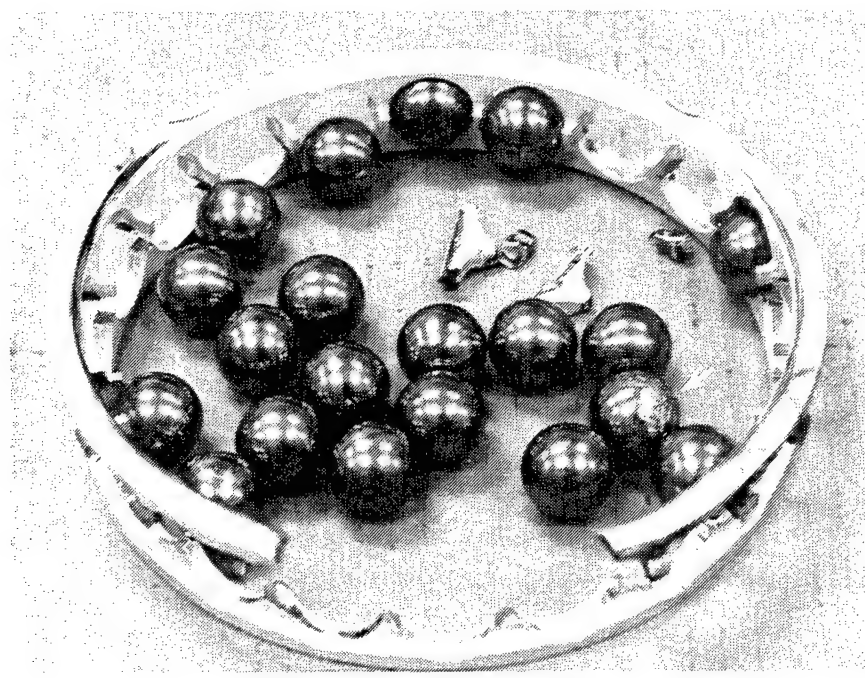


Figure 6. Typical Failure Mode of an All-Steel Bearing *The cage has split in half, and at least one M50 ball has sustained damage (white arrow).*

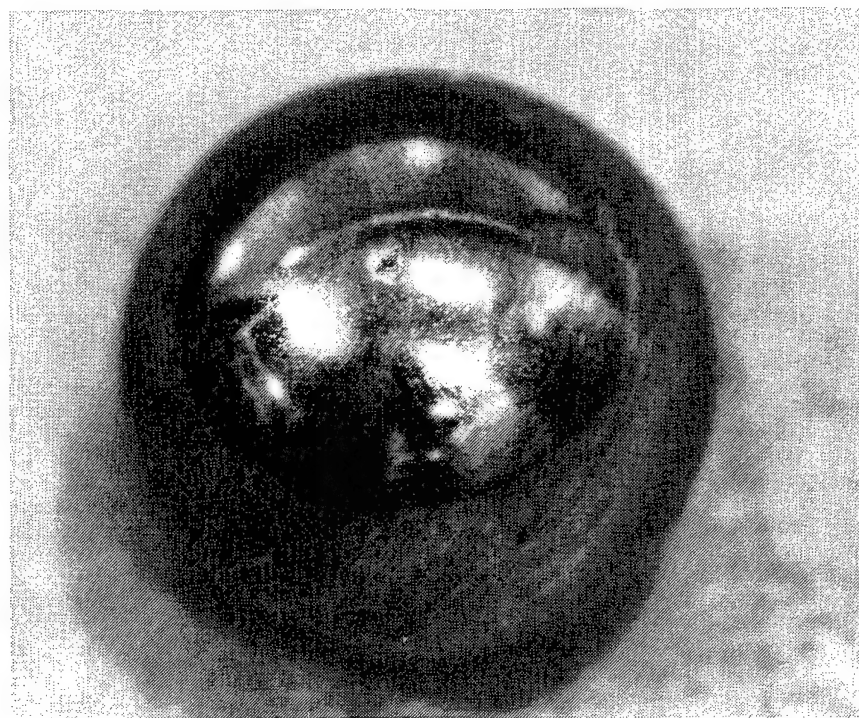


Figure 7. M50 Ball with Minor Distress from Induced-Defect Test

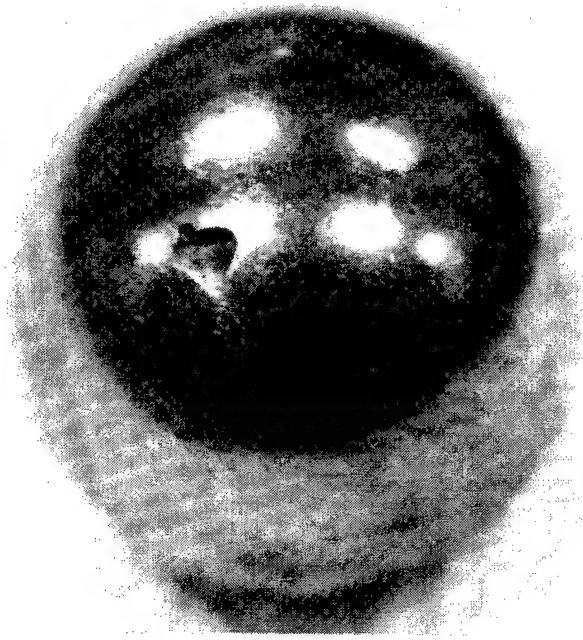


Figure 8. M50 Ball with Moderate Distress from Induced-Defect Test

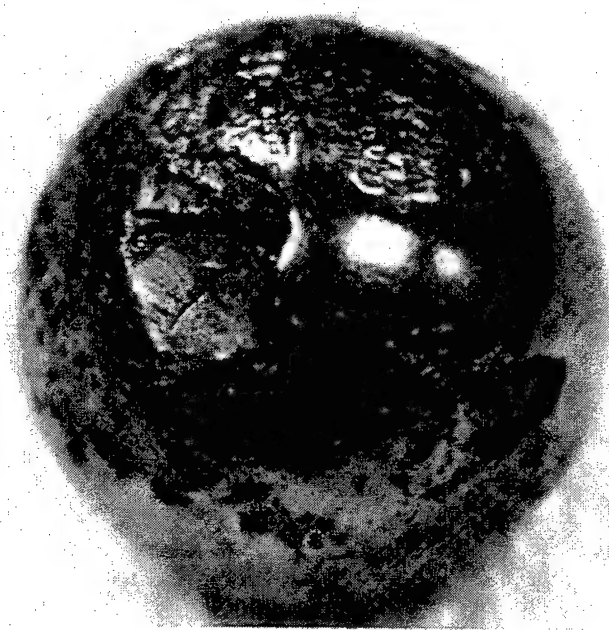


Figure 9. M50 Ball with Significant Distress from Induced-Defect Test

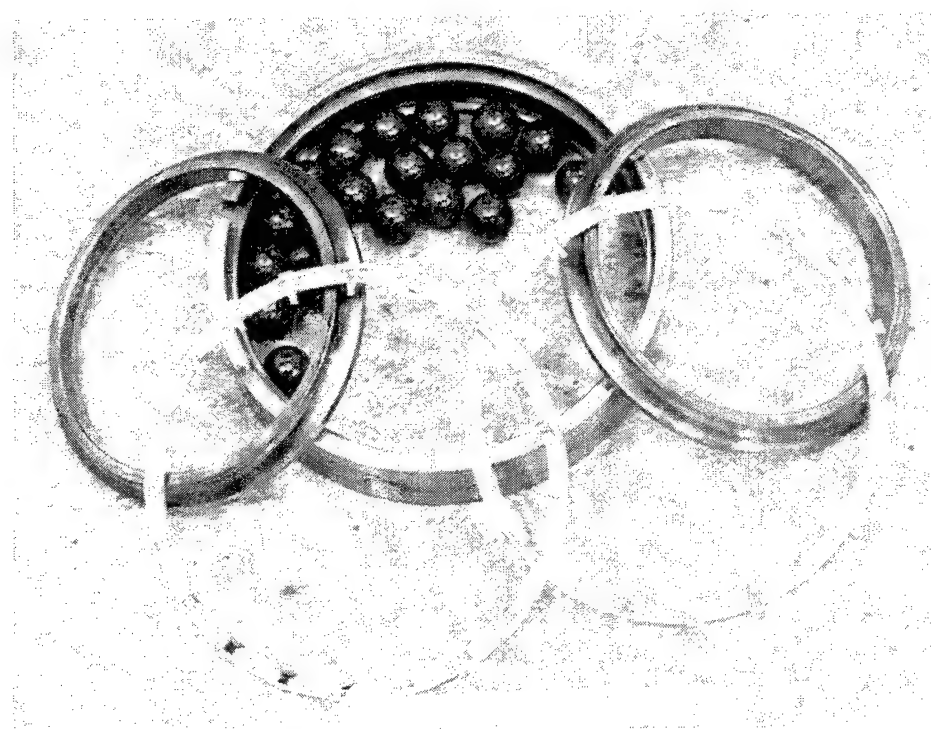


Figure 10. Posttest Bearing Components from Induced-Defect Test 1 The cage has fractured in half, while the Si₃N₄ balls show no signs of distress. The test completed forty-three 30-minute cycles before the cage fractured.



Figure 11. Spall in Outer Race The spall initiated at the EDM notch and propagated roughly 6.3 cm (2.5 in) before the cage fractured.

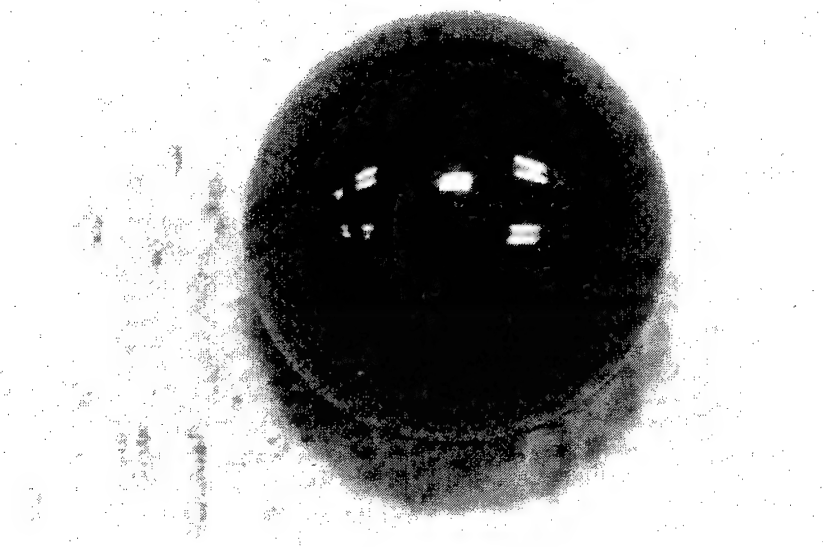


Figure 12. Typical Condition of Silicon Nitride Ball After Completion of the First Induced-Defect Test
No visible signs of distress are evident; all 20 balls look like new.

3.3.2 Test 2 Results

The second induced-defect test ran for a total of 50 cycles (25 hours) before the rig shut down due to an over-temperature, $>193^{\circ}\text{C}$ (380°F) and high-amperage-draw (>180 amps) condition. As in the first test, the cage was the primary component that failed, due to the repeated pounding it took as the balls passed over the growing fatigue spall in the outer race. Figure 13 shows the components from this second test. The spall again initiated at the EDM notch, but this time it propagated roughly 19.0 cm (7.5 in) before the cage failed. Note the cage is not only split in half but is also severely bent. Figure 14 is a higher magnification of the cage and the balls from this test. This test, unlike the first, contained a single ball with surface distress as indicated by the white arrows in Figures 14 and 15. Figure 16 is a scanning electron microscope (SEM) photo of this spall. Note that it is made up of numerous smaller spalls ranging from 500 to 1000 μm in diameter. The entire spall is roughly 0.30 mm (0.012 in) deep, 4.7 mm (0.18 in) in diameter, and — as already noted — is made up of numerous smaller spalls. This indicates that not only are the silicon nitride balls capable of withstanding the severe conditions of a bearing undergoing spall growth, but when the balls do themselves spall, the growth of that spall is stable and slow. The other 19 balls looked like new, as shown in Figure 17. Once again, the silicon nitride balls held up rather well under such severe operating conditions.

3.3.3 Test 3 Results

The third test ran for a total of 128 cycles (64 hours) from the first ECD indication to final failure. Again the over-temperature protection device shut the rig off. Once again, the primary failure mode

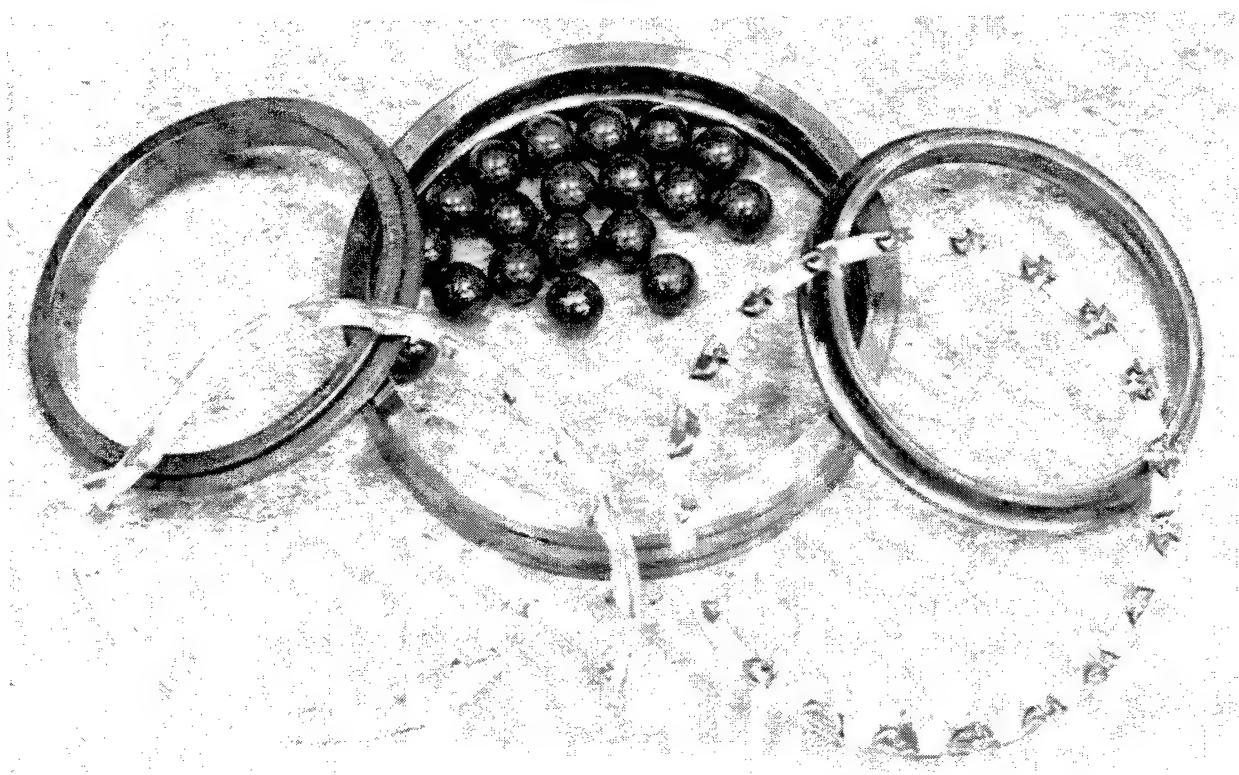


Figure 13. Components from the Second Induced-Defect Test Again, the cage fracture in half was the primary failure mode. This time the test ran for 50 cycles, and the spall in the outer race grew to 19 cm (7.5 in). As in the first test, the balls held up quite well.

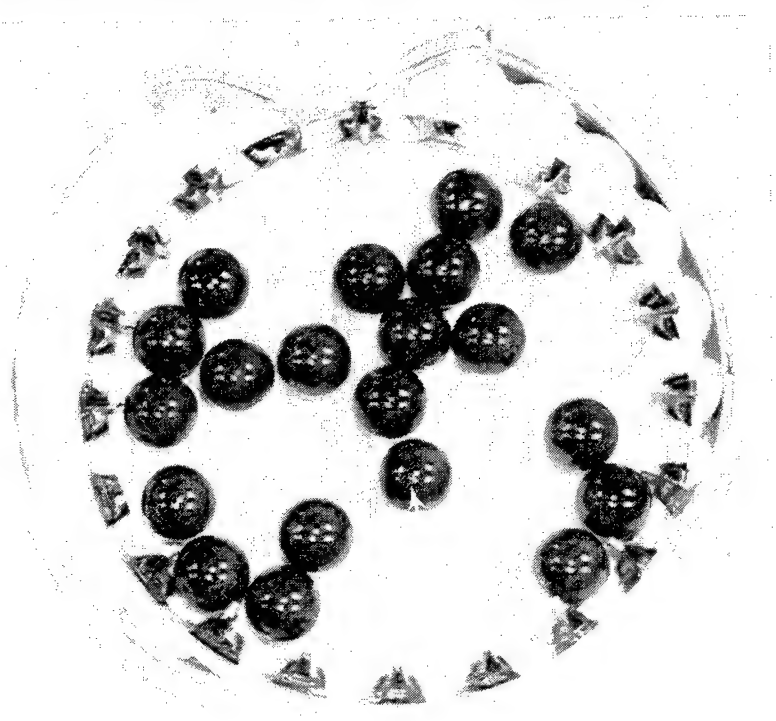


Figure 14. Cage and all 20 Balls from the Second Induced-Defect Test The white arrow points to the only ball with any visible surface distress; the remaining 19 looked like new.

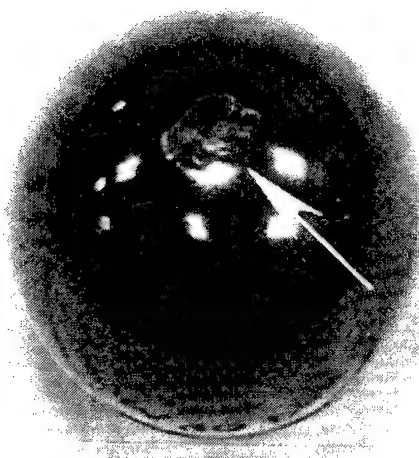


Figure 15. Spalled Area on Ball from Second Induced-Defect Test This was the only ball with any visible distress. The spall is shallow and appears to be made up of numerous smaller spalls.

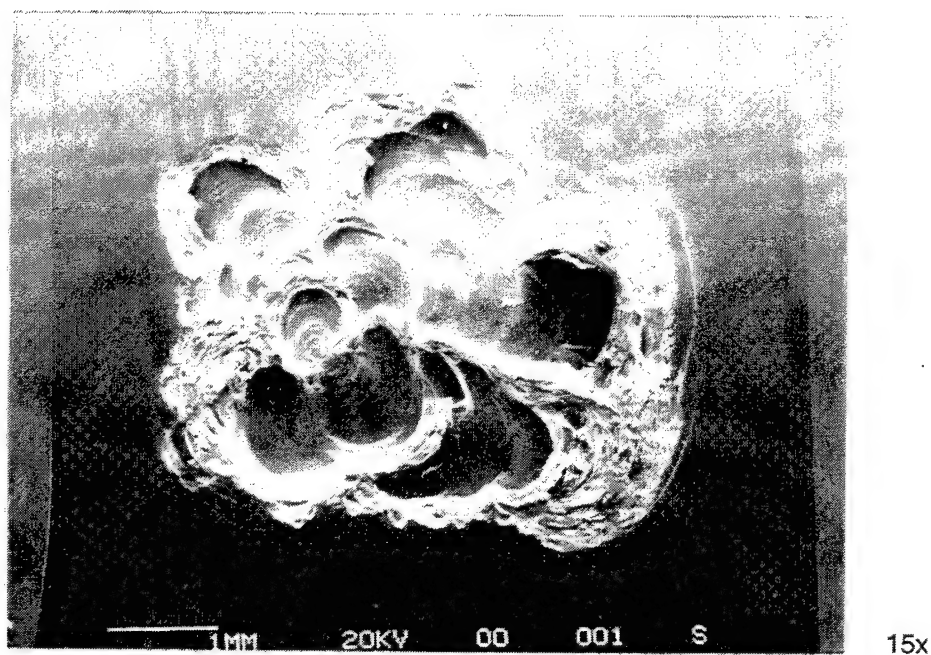


Figure 16. SEM Photo of Spalled Area on Ball from Second Induced-Defect Test The spall is made up of smaller spalls ranging from 500 to 1000 μm diameter.

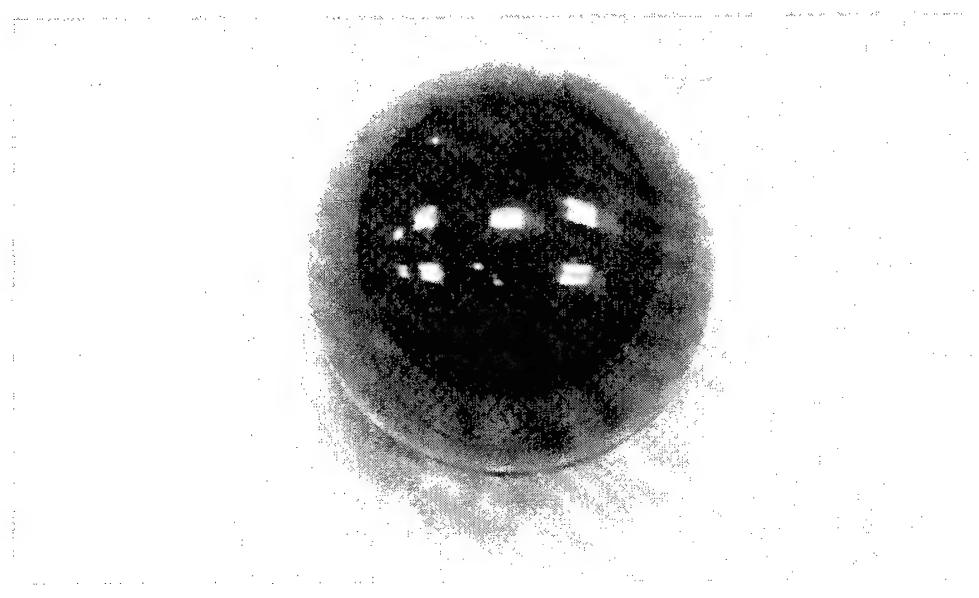


Figure 17. Typical Condition of 19 Unspalled Balls After Second Induced-Defect Test *Note the new-like appearance of the surface.*

was that of the cage splitting, as shown in Figure 18. Figure 19 shows all 20 balls in the fractured cage, with white arrows pointing to two of the three balls which spalled during this test. Figure 20 shows the spall initiating out of the EDM notch as well as wrapping around 360° to join back up with the EDM notch. This is a strong indicator of the severity of the test. In addition to the outer ring containing numerous spalls, the load side of the inner ring also contained numerous small spalls, most likely initiated by the large amount of debris being rolled over during this test. The spall from the EDM notch was roughly 12.7 cm (5.0 in) long with spotty spalls through 360° of the outer ring. Figures 21, 22, and 23 are higher magnifications of the three spalled balls. Again the spalls are relatively small with depths of 0.22 to 0.35 mm (0.009 to 0.014 in) and diameters of approximately 6.3 mm (0.25 in). In these three figures, it is evident that the spalls are made up of a series of smaller spalls. Figure 24 is an SEM photo of one of the spalls from this third induced-defect test. It also indicates that the larger spall is made up of numerous smaller spalls which range in size from 500 to 1000 μm .

3.3.4 Test 4 Results

Test 4 was similar to the first three, except that it ran for a total of 143 cycles (71.5 hours), and five balls had minor spalls at the end of the test. Figure 25 shows the components from this final induced-defect test. The five balls with spalls are separated from the remaining 15 without any visible damage. The fractured cage is shown in Figure 26. Figure 27 shows the five balls that spalled during the fourth induced-defect test. Again, the spalls are relatively benign compared to damage which has been seen in M50 balls. The spalls on the silicon nitride balls from this test are again shallow, 0.3 mm (0.012 inch), roughly 6.3 to 12.7 mm (0.25 to 0.50 in) oval or round, and appear to be made up of between 15 and 30 smaller spalls, as shown in Figure 28 (SEM photo of spall). The outer ring spall originated from the EDM notch, as shown in Figure 29. Spalls were evident through the entire 360° arc of the outer race.

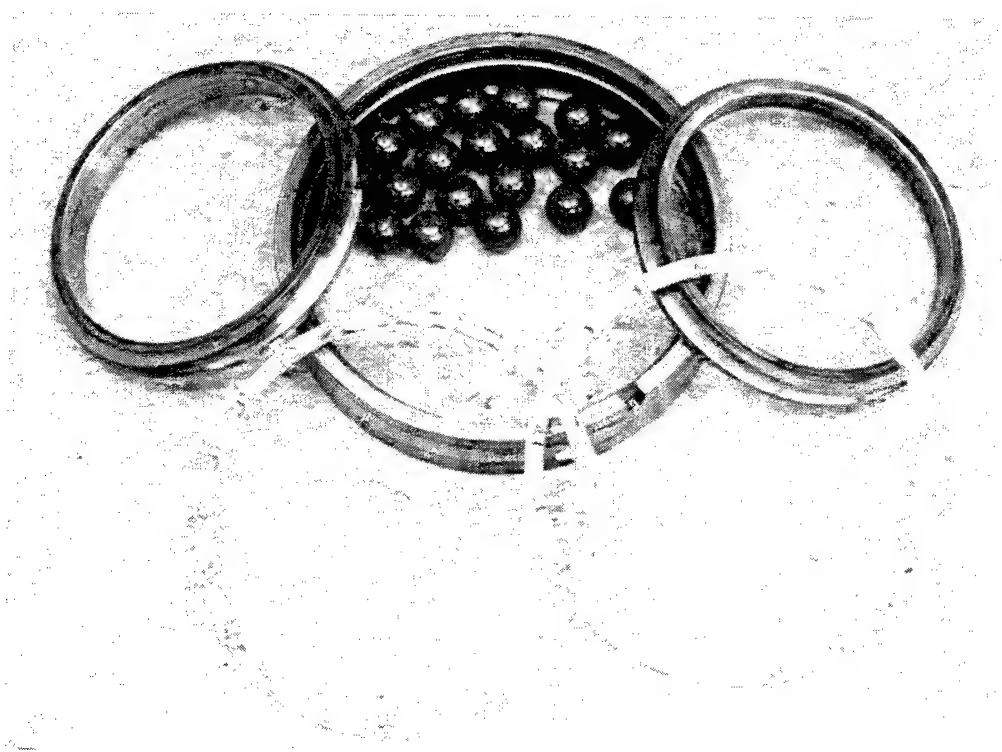


Figure 18. Components from the Third Induced-Defect Test Once again the balls held up well, and the cage fracturing in half was the primary mode of failure. At the conclusion of this test, three balls had minor spalls.



Figure 19. Fractured Cage with all 20 Silicon Nitride Balls from Third Induced-Defect Test The two white arrows indicate two of the three balls that ended up with minor spalls.



Figure 20. Spalled Outer Race The spall initiated at the EDM notch and wrapped around 360° to join back up with the initiation point. This is a strong indication of the severity of the test and the amount of bearing steel that was liberated before final failure occurred.

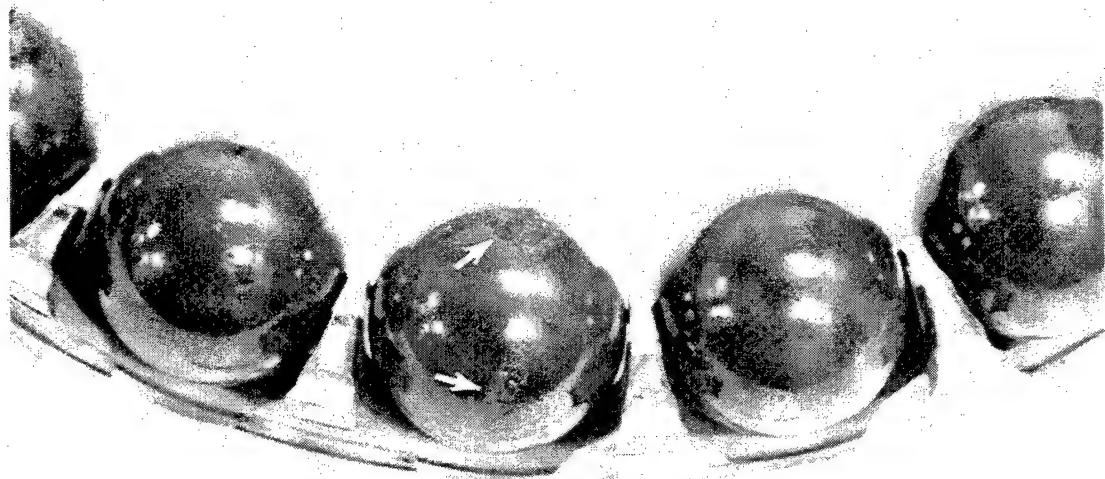


Figure 21. One of the Three Silicon Nitride Balls from Test 3 that Experienced Minor Surface Distress The white arrows indicate areas of shallow spalls that, as in prior tests, appear to be made up of numerous smaller spalls.

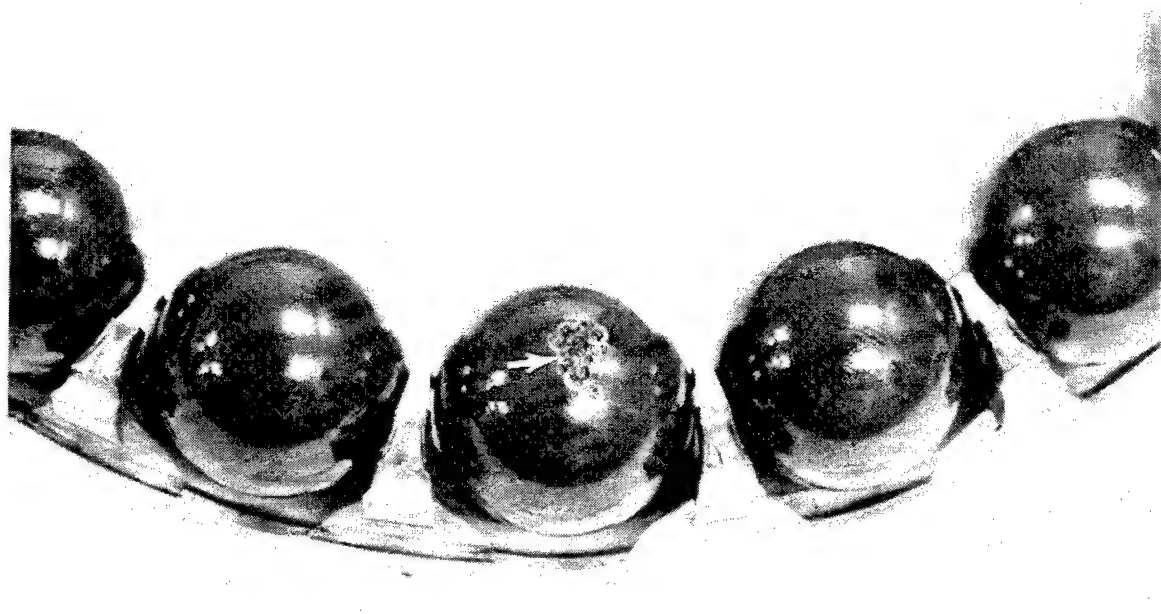


Figure 22. Second of Three Balls to Suffer Minor Surface Distress in Third Induced-Defect Test
As with the other silicon nitride balls with spalls, this spall seems to be made up of numerous smaller ones. This is an indication of stable, slow spall growth even under the severe test conditions.

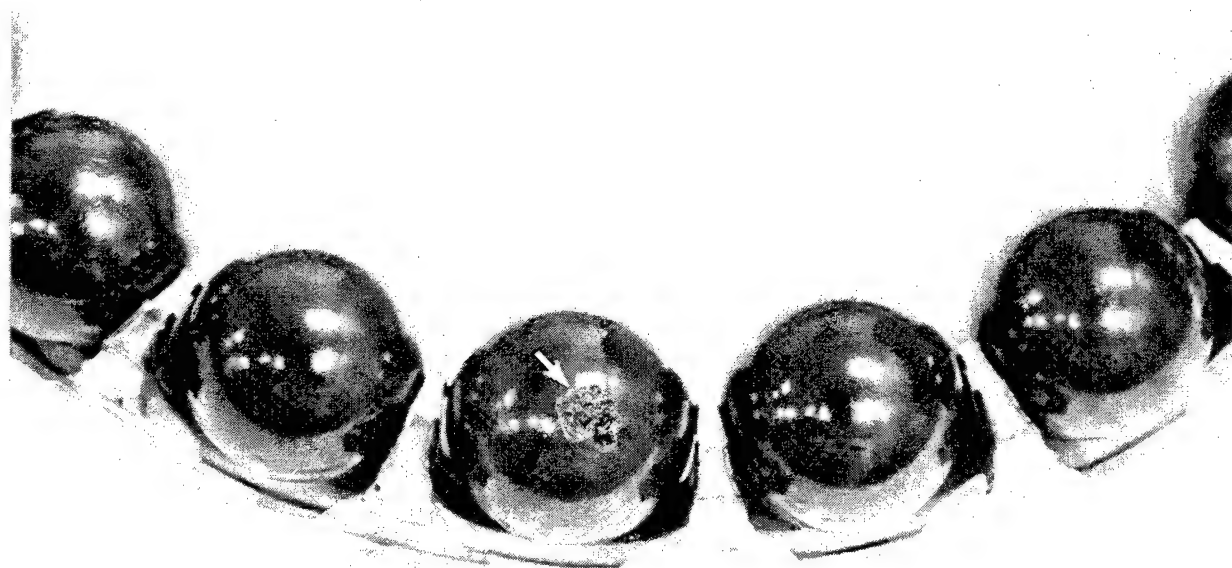


Figure 23. Third of Three Balls to Show Surface Distress *As in the others, the small spall appears to be composed of numerous smaller spalls.*

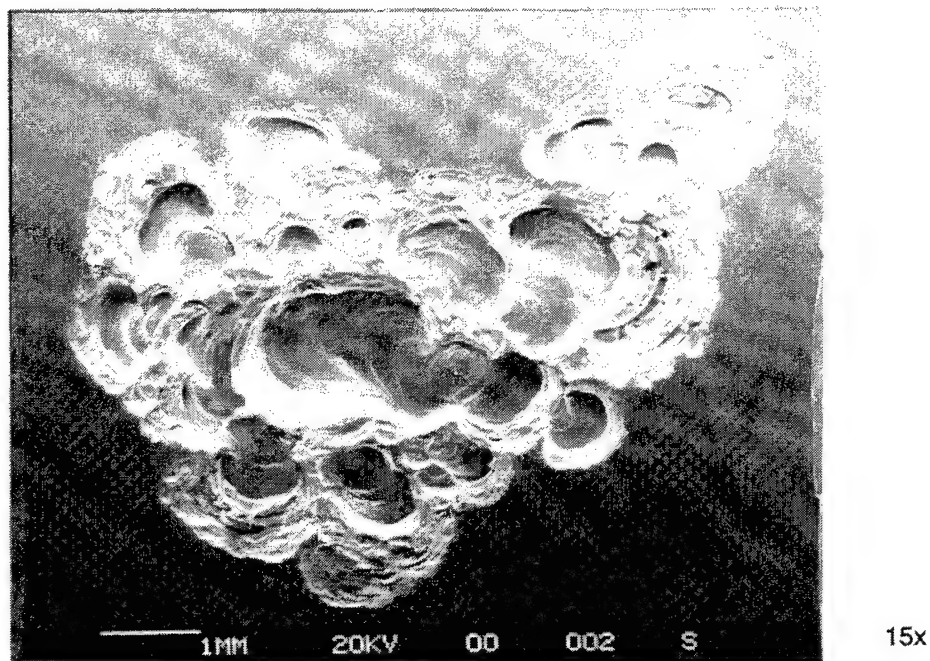


Figure 24. SEM Photo of Spalled Area on Ball from Third Induced-Defect Test *The spall is made up of smaller spalls ranging from 500 to 1000 μm diameter.*

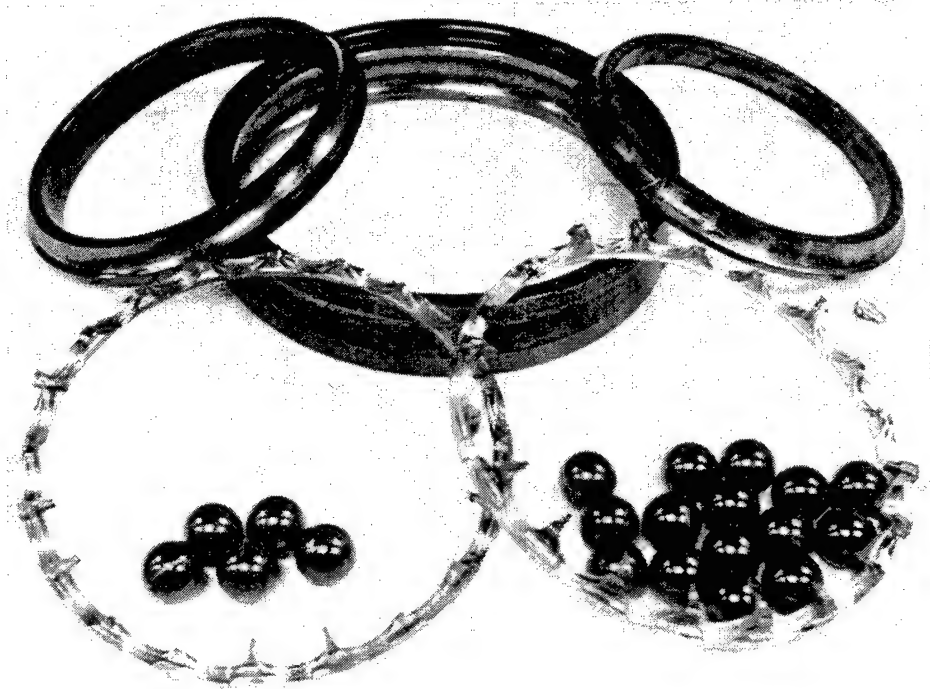


Figure 25. Components from Fourth Induced-Defect Test *As in the prior tests, the cage fracturing in half was the primary mode of failure. However, this test ran for 143 cycles after race spalling occurred, and five silicon nitride balls show minor spalls.*

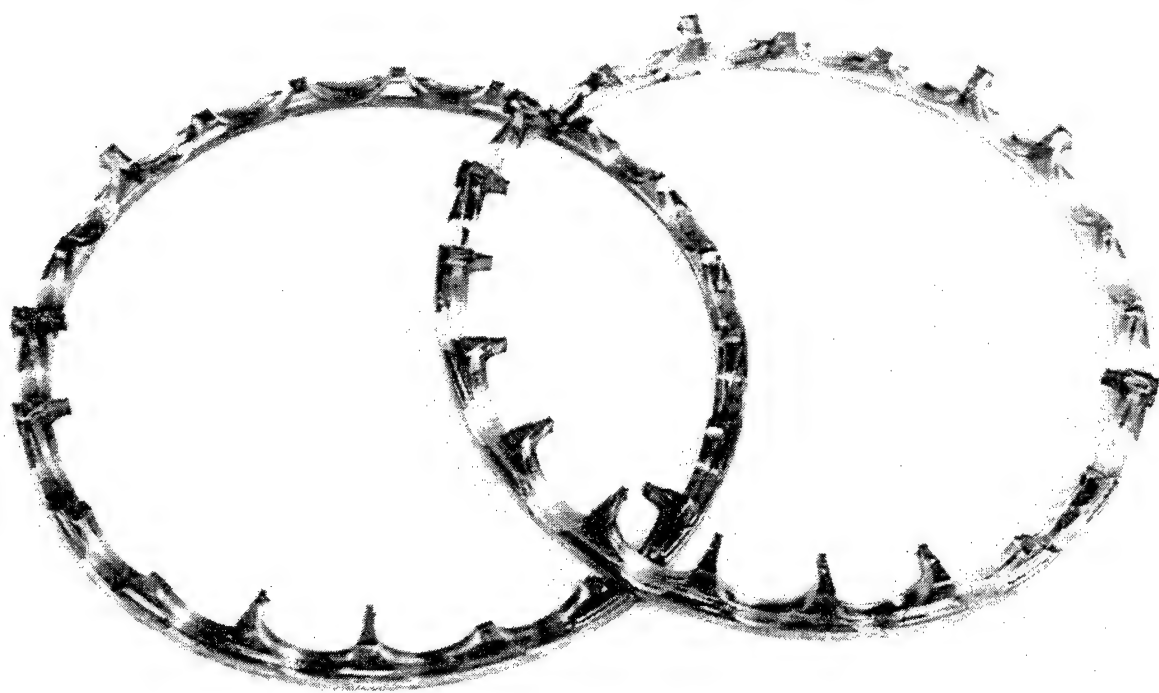


Figure 26. Fractured Cage from Fourth Induced-Defect Test

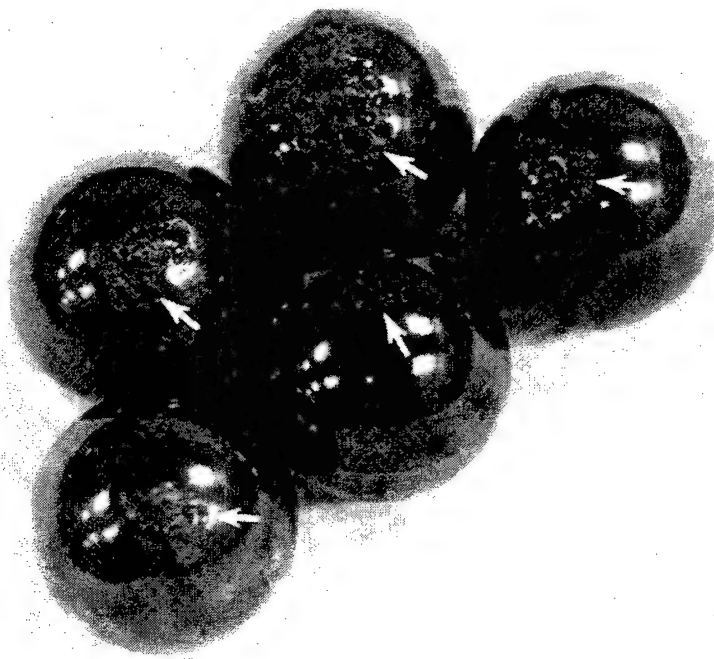


Figure 27. Five Balls that Spalled During the Fourth Induced-Defect Test
Once again, the shallow spalls appear to be made up of numerous smaller spalls.

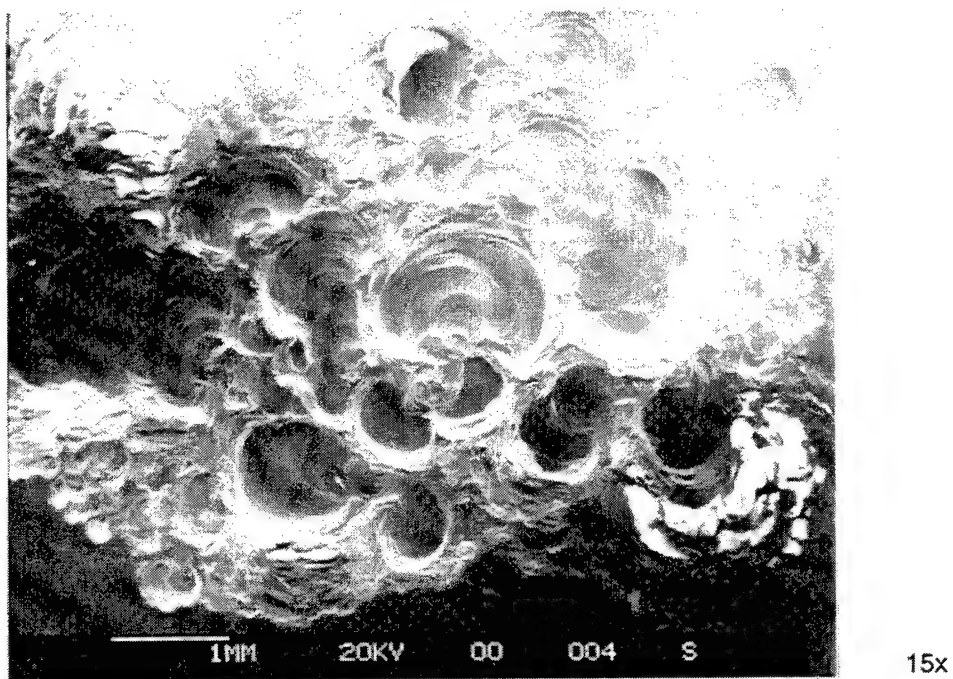


Figure 28. SEM Photo of Spalled Area on Ball from Fourth Induced-Defect Test The spall is made up of smaller spalls ranging from 500 to 1000 μm diameter.

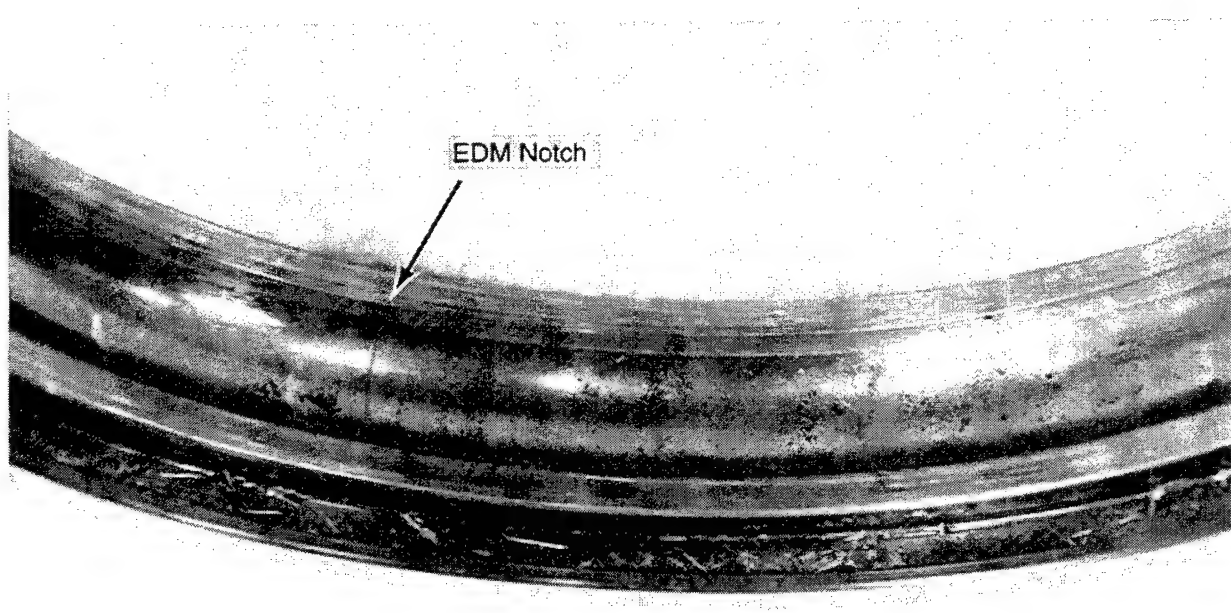


Figure 29. Outer Ring with Spall Initiating at the EDM Notch The large amount of debris in the puller groove indicates the severity of the test.

3.4 Bearing Debris Analysis

Metallic and nonmetallic debris were collected during the fourth induced-defect test, from both the M50NiL steel rings and the silicon nitride balls. Figure 30 shows a petri dish with approximately 5.5 grams of M50NiL chips that were caught in the chip collector (described in the discussion of Task 3, Section 5). Examination of the M50NiL chips indicated they averaged 1.25 mm in diameter, as shown in Figure 31. Figure 32 shows the nonmagnetic debris collect during this test. Figures 33 through 35 show debris identified as silicon nitride. The particles ranged in size from 0.08 by 0.16 to 0.3 by 0.6 mm. This indicates that, although the silicon nitride chips appear to be smaller than the steel chips, they are of reasonable size for detection and do not disintegrate after spalling off the ball.

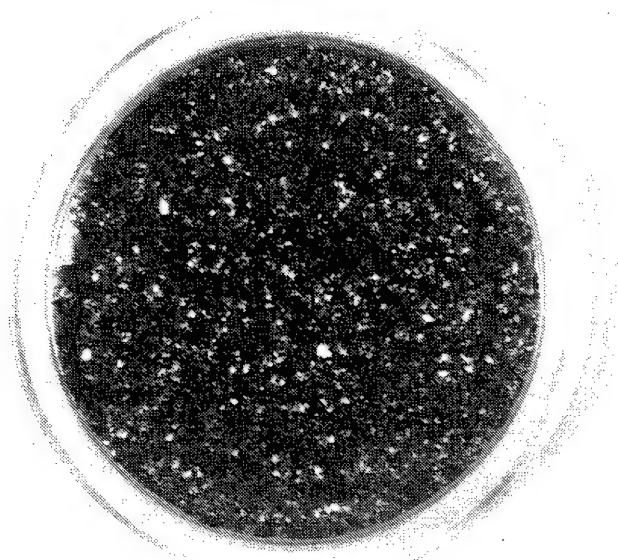


Figure 30. Debris Caught in the Chip Collector During the Final Induced-Defect Test *The petri dish contains 5.5 grams of M50NiL chips, an appreciable amount of debris.*

Comparison of the amount of debris liberated by the hybrid bearings versus that of an all-steel bearing indicates that up to 5 to 10 times more metallic debris can be liberated by the hybrid bearing. This could be significant if magnetic plugs or ECD are used to indicate bearing problems; the larger amount of debris would increase the likelihood of detecting a bearing undergoing distress.

Table 1 summarizes the results of the induced-defect testing.

Table 1. Summary of Induced-Defect Testing.

Test Number	Primary Failure Mode	Hours from 1st Chip	Number of Cycles	Ball Condition
1	Fractured Cage	22	43	20/20 Excellent
2	Fractured Cage	25	50	19/20 Excellent, 1 Small Spall
3	Fractured Cage	64	128	17/20 Excellent, 3 Small Spalls
4	Fractured Cage	71	141	15/20 Excellent, 5 Small Spalls

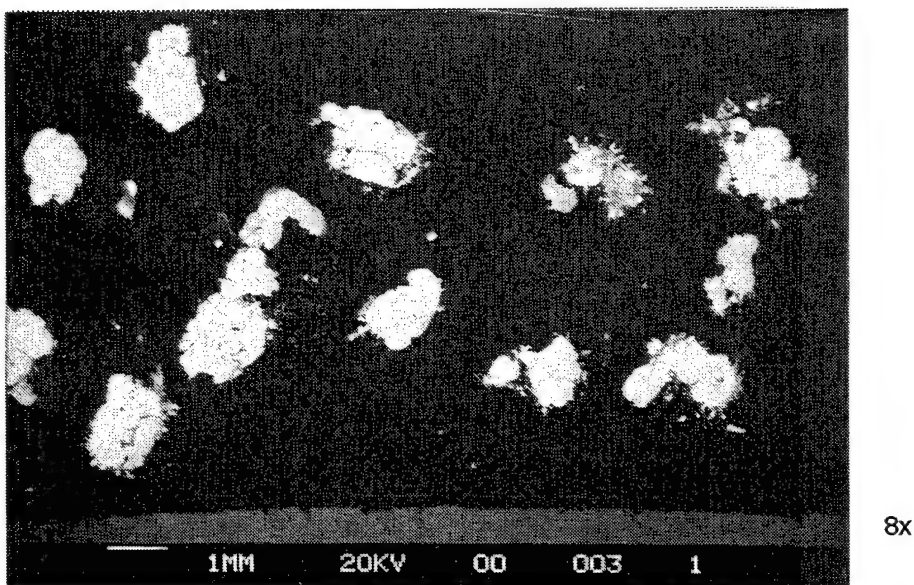


Figure 31. SEM Photo of Representative Chips from Figure 30
Chips average 1.25-mm diameter and are relatively flat.

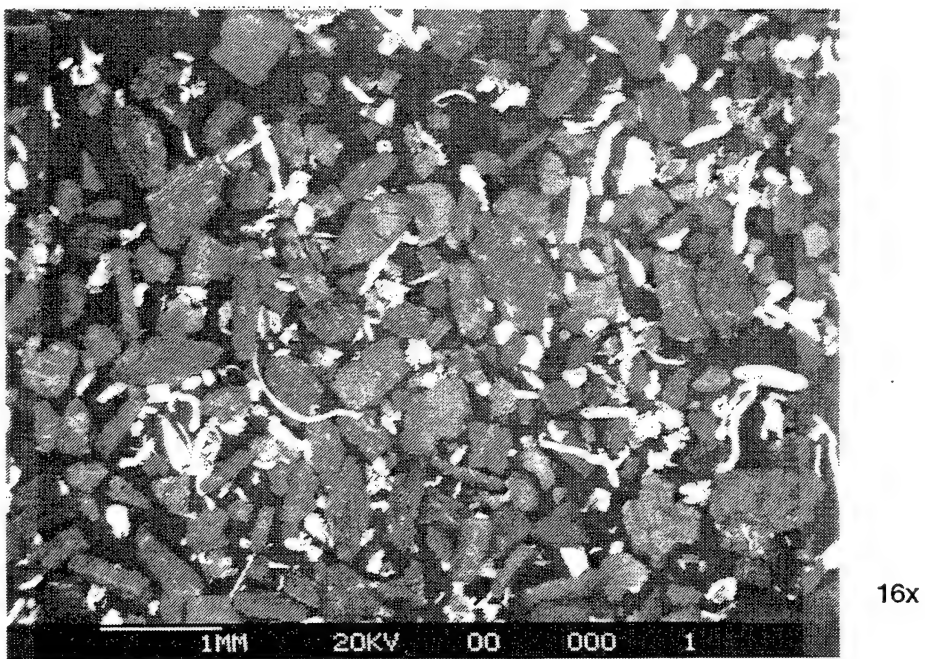


Figure 32. Nonmagnetic Debris Caught in Chip Collector During Final Induced-Defect Test
Most of the debris is coke product and silver from the cage; however, a few silicon nitride chips were discerned.

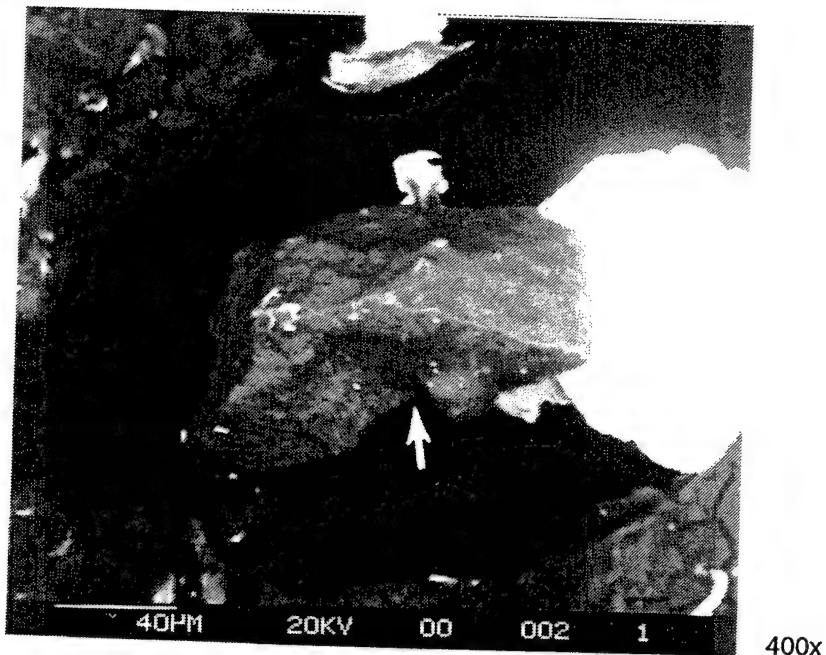


Figure 33. Silicon Nitride Chip from Final Induced-Defect Test
This chip is approximately 80 by 160 μm .

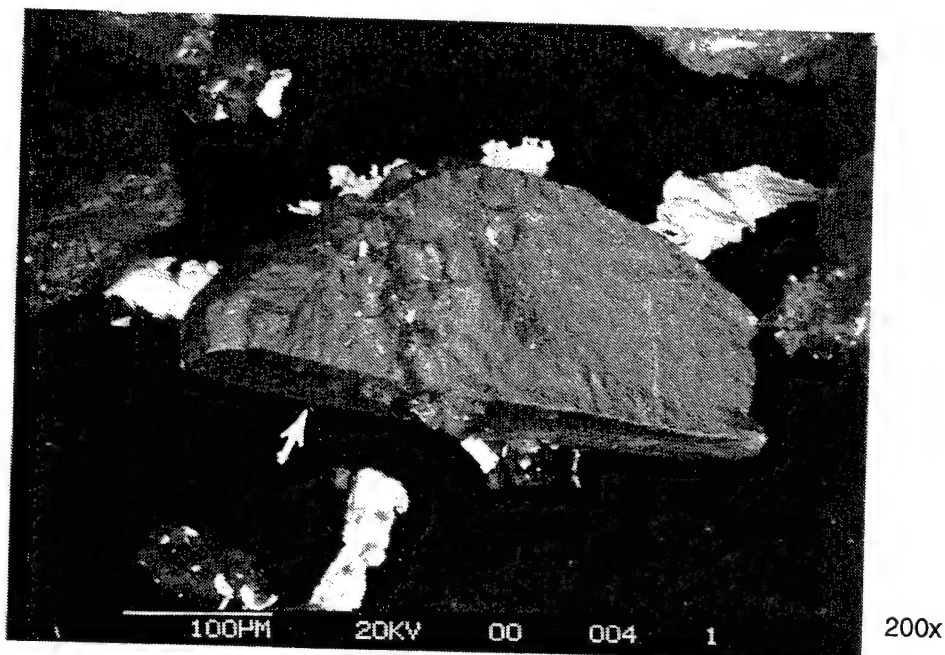


Figure 34. Silicon Nitride Chip from Final Induced-Defect Test
This chip is approximately 150 by 400 μm .

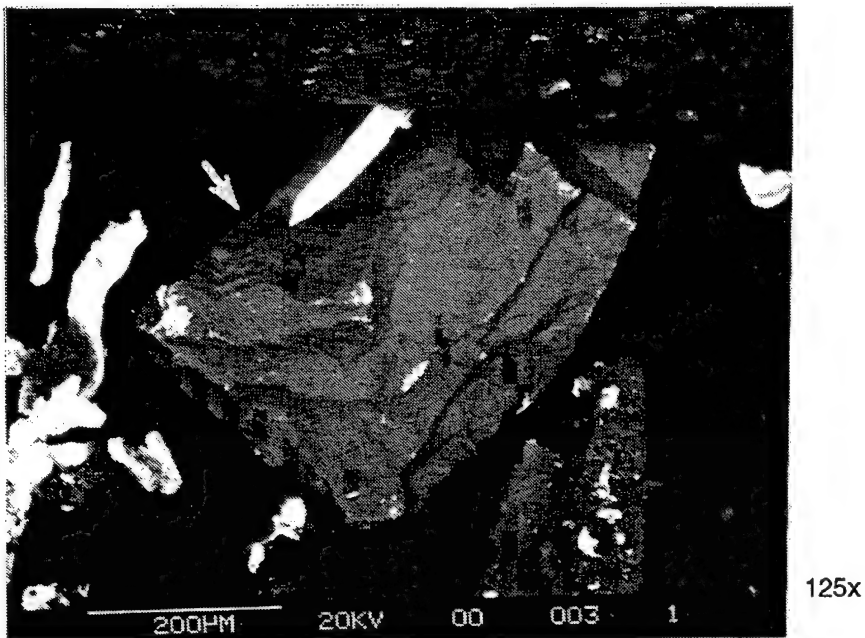


Figure 35. Silicon Nitride Chip from Final Induced-Defect Test
This chip is approximately 360 by 600 μm .

3.5 Task 1 Conclusions

- Silicon nitride balls are capable of withstanding the high shock loads encountered during race spalling.
- The hybrid bearing operates for a reasonable length of time after race spall initiation and is comparable to that of an all-steel bearing.
- The silicon nitride balls exhibit no more distress than AISI M50 tool steel balls.
- Spalls on the silicon nitride balls are made up of numerous smaller spalls, and the chips coming off are large enough to be caught in a 400- μm size screen for detection.
- The hybrid bearing may be liberating significantly more metallic debris than an all-steel bearing, increasing the probability of detecting an impending failure.

3.6 Recommendations for Future Tests

Future induced-defect testing should include placing the defect in the silicon nitride balls and noting the rate of defect growth. Additionally, it may be useful to explore other types of defects, such as contaminated oil or a dented surface from which the spall would grow.

From this series of tests, it appears that a hybrid bearing may spall a larger amount of debris, before undergoing catastrophic failure, than an all-steel bearing. This has significant ramifications on the detectability of incipient bearing failure. Additional tests should be performed to confirm these results.

The hybrid bearing design was not changed or optimized from that of the steel bearing. This may have resulted in larger operating internal clearances and a more severe induced-defect test. In future tests, an optimized hybrid bearing design may further improve the bearing capability.

4.0 Task 2 – High-Speed Testing

4.1 Objective

This task was performed to determine if hybrid bearings (silicon nitride balls with AISI M50 or AISI M50NiL steel races) operated cooler than all-steel bearings (AISI M50 balls with steel races) under normal engine operating conditions, thus allowing reduced cooling requirements or an anticipated improvement in bearing performance or life.

4.2 Test Procedure

Comparisons were made by collecting data (outer-ring temperatures, inner-ring temperatures, power draw, and cage kinematics) from a set of all-steel bearings (designated P04), a set of hybrid bearings with the same internal geometry as the all-steel bearing (designated P05), and a set of hybrid bearings with a higher ball/race conformity to reduce hertzian contact stress (designated P06).

Data were collected using a 120-mm, angular-contact bearing operated from 1.5 to 3.0 MDN (12,500 to 25,000 rpm), with loads of 4.44 kN (1000 lbf) and 22.24 kN (5000 lbf), and oil (Mil-L-7808) flow rates between 63.1 cm³/s (1 gpm) and 126.2 cm³/s (2 gpm) for the first 90 test points, reduced oil for the last 11 test points (91 through 101). Oil was supplied through the split inner ring only for the first 90 test points, and in different combinations of through the split inner ring and outer ring cooling for the last 11 test points (91 through 101). The all-steel bearing P04 and the hybrid bearing P05 both have an inner race curvature of 0.54 and an outer race curvature of 0.52, while the hybrid bearing P06 has an inner race curvature of 0.5225 and an outer race curvature of 0.5175. The bearing used in this test required 15 balls 20.6 mm (0.8125 in) in diameter. The silicon nitride balls used in this Task were Toshiba Si₃N₄. The bearings were manufactured by MRC/SKF Bearings.

Task 2 testing was performed at Industrial Tectonics Bearing Corporation (ITCB) on the machine shown in Figures 36 and 37. Figure 38 is a schematic of the test rig.

In all, this task comprised 101 data points. The testing was based on *design of experiment* (DOE) techniques; both full factorial and fractional factorial designs were used. Again, our goal was to determine if thermal advantages existed with a hybrid bearing compared to an all-steel bearing; therefore, testing was structured and modified in an attempt to identify hybrid bearing benefits.

4.3 Results and Discussion

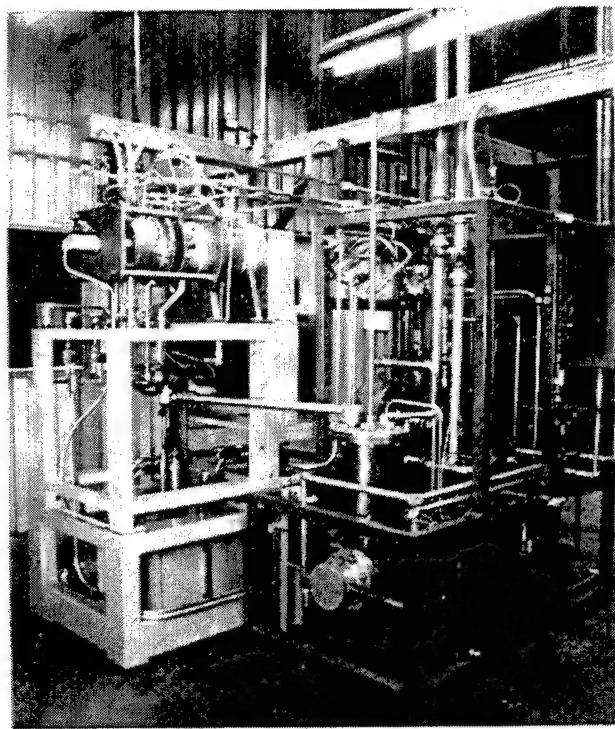
4.3.1 All-Steel Bearing (P04) Data, Points 1 – 36

As mentioned above, all testing was structured using DOE techniques. Table 2 shows the conditions of the first 36 test points.

Figure 39 shows the outer-ring temperature as a function of shaft speed, load, and oil-flow rate with an oil-in temperature of 121°C (250°F). Note that the outer-ring temperature generally increases with increasing shaft speed, increasing load, and decreasing oil flow, all of which are to be expected.

Figure 40 shows the test rig power draw for the P04 bearing as a function of shaft speed, load, and oil-flow rate. Power requirements generally increase with increasing speed, increasing load, and increasing oil-flow rate. The most likely cause of the added power consumption for the higher oil flow rates is the extra oil churning required.

The separator speed ratio as a function of shaft speed, load, and oil flow rate is shown in Figure 41. It is apparent the all-steel bearing has a higher tendency for slip at the lower load. This is as expected.



A color image is presented in Reference 1.

Figure 36. ITBC's 120-mm Bearing Test Machine

A color image is presented in Reference 1.

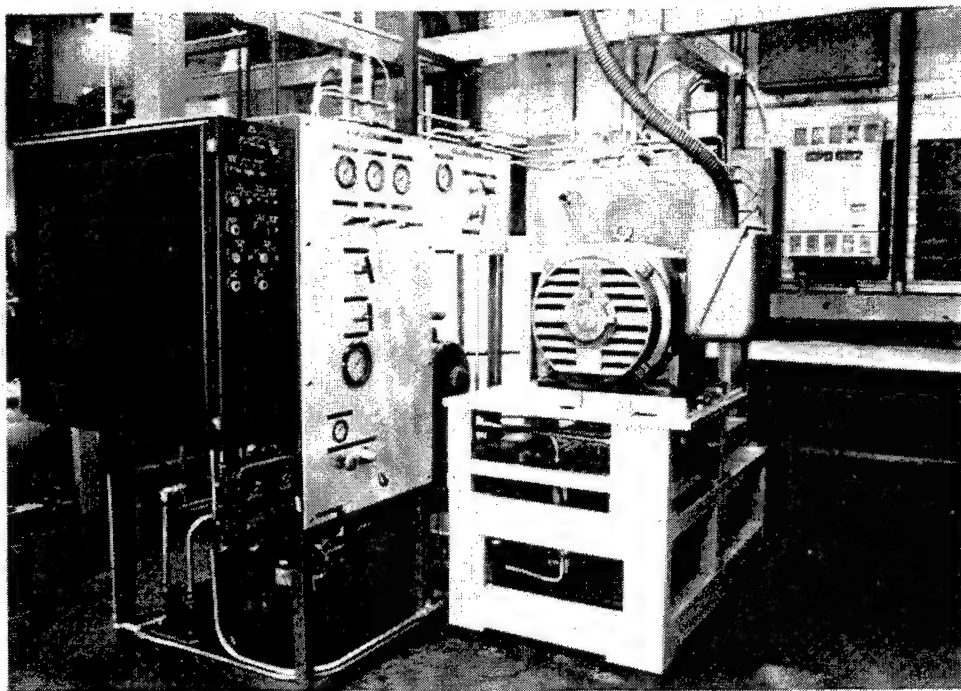


Figure 37. Control Panel of 120-mm Bearing Test Machine at ITBC

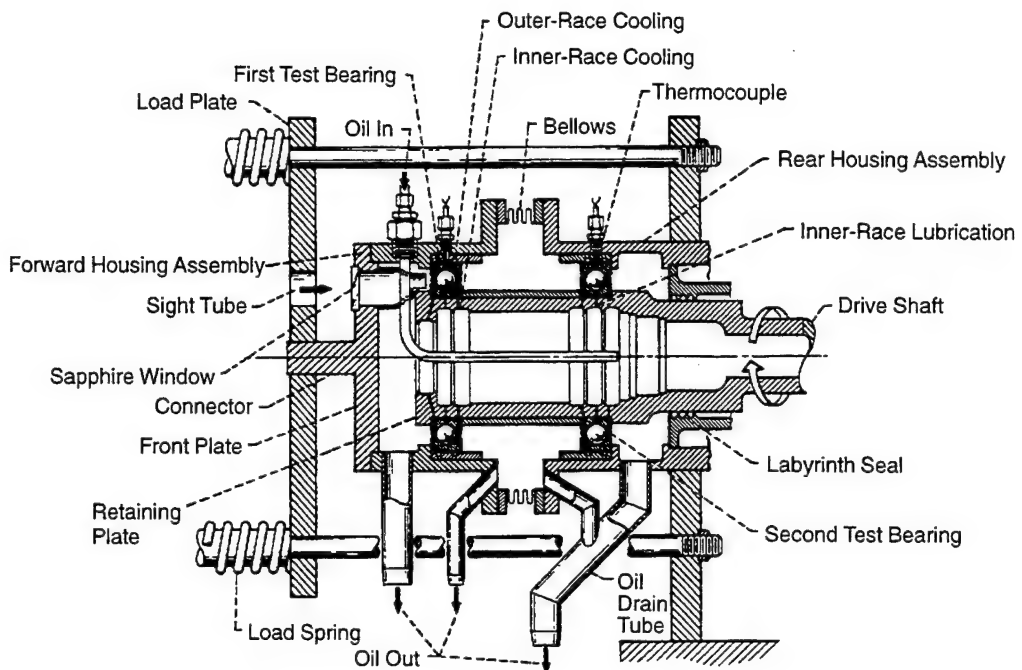


Figure 38. Schematic of 120-mm Bearing Test Rig

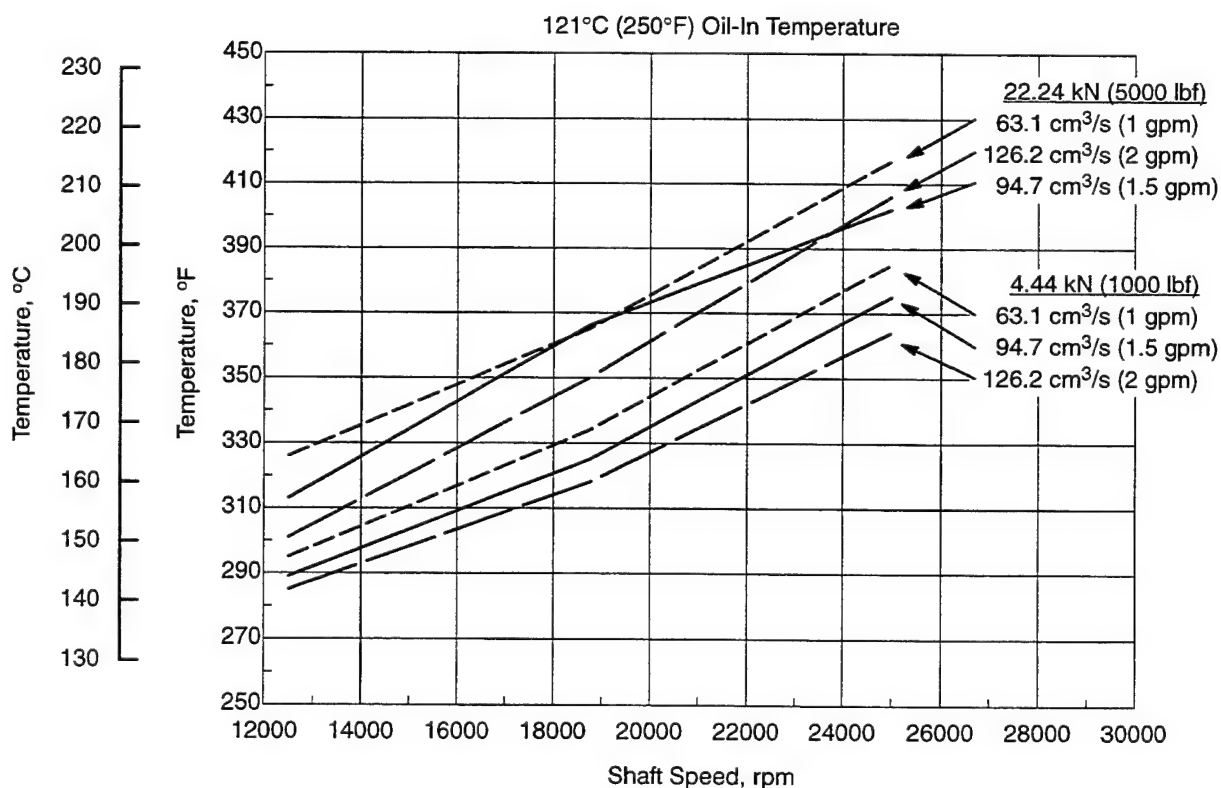


Figure 39. Bearing P04 Outer-Ring Temperature as a Function of Shaft Speed

Table 2. First 36 Points of 120-mm Bore Test, Bearing P04

Test Point	Shaft Speed, rpm	Axial Load, kN (lbf)	Oil Flow, cm ³ /s (gpm)	Oil Inlet Temperature, °C (°F)
1	12,500	4.44 (1000)	126.2 (2.0)	121 (250)
2	12,500	4.44 (1000)	94.7 (1.5)	121 (250)
3	12,500	4.44 (1000)	63.1 (1.0)	121 (250)
4	12,500	22.24 (5000)	126.2 (2.0)	121 (250)
5	12,500	22.24 (5000)	94.7 (1.5)	121 (250)
6	12,500	22.24 (5000)	63.1 (1.0)	121 (250)
7	18,750	4.44 (1000)	126.2 (2.0)	121 (250)
8	18,750	4.44 (1000)	94.7 (1.5)	121 (250)
9	18,750	4.44 (1000)	63.1 (1.0)	121 (250)
10	18,750	22.24 (5000)	126.2 (2.0)	121 (250)
11	18,750	22.24 (5000)	94.7 (1.5)	121 (250)
12	18,750	22.24 (5000)	63.1 (1.0)	121 (250)
13	25,000	4.44 (1000)	126.2 (2.0)	121 (250)
14	25,000	4.44 (1000)	94.7 (1.5)	121 (250)
15	25,000	4.44 (1000)	63.1 (1.0)	121 (250)
16	25,000	22.24 (5000)	126.2 (2.0)	121 (250)
17	25,000	22.24 (5000)	94.7 (1.5)	121 (250)
18	25,000	22.24 (5000)	63.1 (1.0)	121 (250)
19	12,500	4.44 (1000)	126.2 (2.0)	65 (150)
20	12,500	4.44 (1000)	94.7 (1.5)	65 (150)
21	12,500	4.44 (1000)	63.1 (1.0)	65 (150)
22	12,500	22.24 (5000)	126.2 (2.0)	65 (150)
23	12,500	22.24 (5000)	94.7 (1.5)	65 (150)
24	12,500	22.24 (5000)	63.1 (1.0)	65 (150)
25	18,750	4.44 (1000)	126.2 (2.0)	65 (150)
26	18,750	4.44 (1000)	94.7 (1.5)	65 (150)
27	18,750	4.44 (1000)	63.1 (1.0)	65 (150)
28	18,750	22.24 (5000)	126.2 (2.0)	65 (150)
29	18,750	22.24 (5000)	94.7 (1.5)	65 (150)
30	18,750	22.24 (5000)	63.1 (1.0)	65 (150)
31	25,000	4.44 (1000)	126.2 (2.0)	65 (150)
32	25,000	4.44 (1000)	94.7 (1.5)	65 (150)
33	25,000	4.44 (1000)	63.1 (1.0)	65 (150)
34	25,000	22.24 (5000)	126.2 (2.0)	65 (150)
35	25,000	22.24 (5000)	94.7 (1.5)	65 (150)
36	25,000	22.24 (5000)	63.1 (1.0)	65 (150)

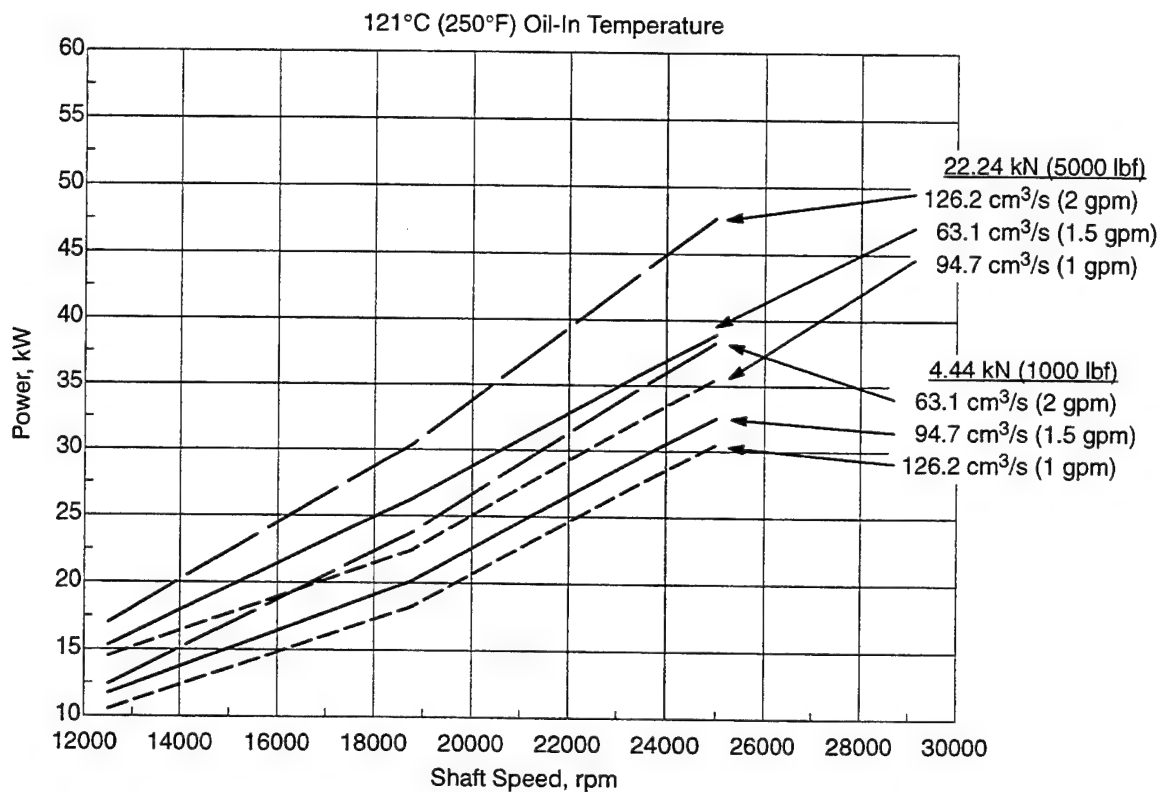


Figure 40. Bearing P04 Rig Power Consumption as a Function of Shaft Speed

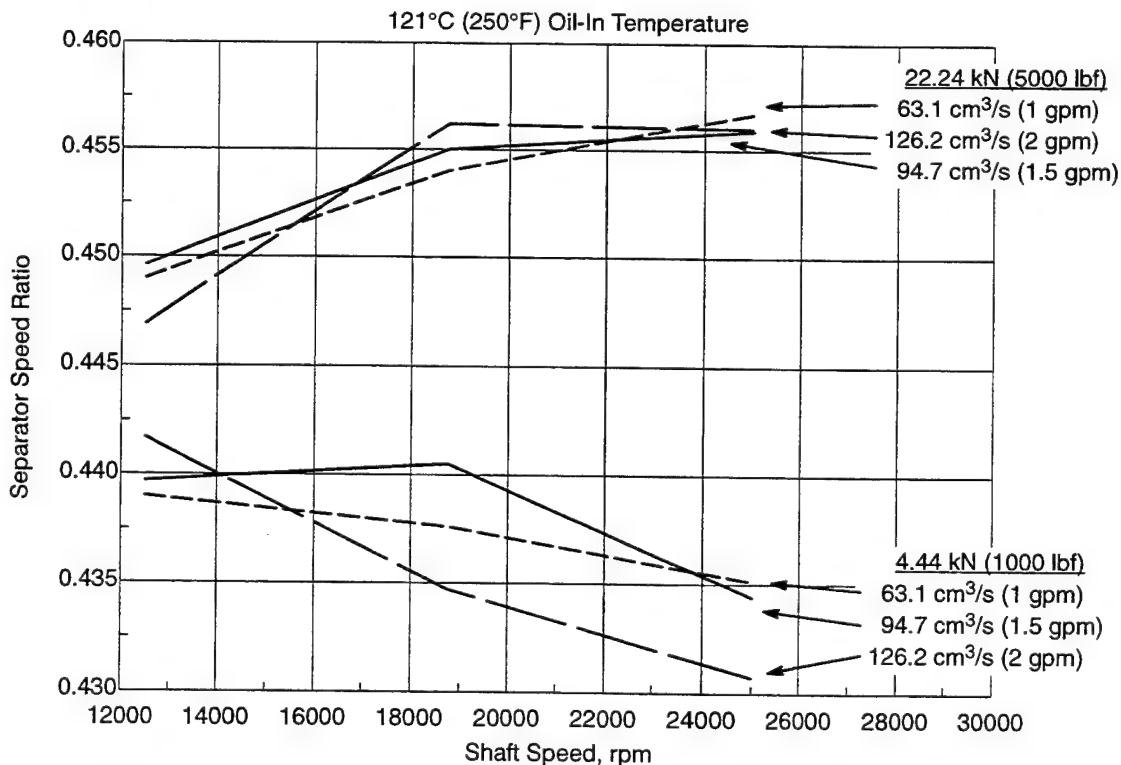


Figure 41. Bearing P04 Separator Speed Ratio as a Function of Shaft Speed

The above plots will be compared to those generated from the testing of the P05 and P06 bearings in an attempt to assess thermal or kinematic benefits.

Figure 42 shows a P04 bearing after completion of the 36 tests points. Except for some rubbing of the cage on the inner-ring land, the bearing is in good condition. This rubbing is considered to have minimal if any effect on the test data, and is most likely caused by the balance of the cage, although the cage balance met specifications.



Figure 42. All-Steel 120-mm Bore Bearing After Completion of 36 Test Points *Other than a slight rubbing of the cage, this bearing is in good condition. Note that the ball path and the lands of the bearing were nodular thin dense chrome (TDC) plated.*

4.3.2 Open-Curvature Hybrid Bearing (P05) Data, Points 37 – 72

As with the all-steel bearing tests, testing of the hybrid bearing was performed using DOE techniques. Table 3 shows the test conditions of test points 37 – 72.

Figure 43 shows the outer-ring temperature as a function of shaft speed, load, and oil flow rate with an oil-in temperature of 121°C (250°F). As with the all-steel bearing, the outer-ring temperature of the hybrid bearing generally increases with increasing shaft speed, increasing load, and decreasing oil flow rates. Comparison of the 36 outer-ring temperature data points (load end + drive end bearings) for the hybrid bearing to the 36 data points (load end + drive end bearing) for the steel bearing indicates that the hybrid bearing runs on average 2.4°C (4.4°F) cooler. The trend of the hybrid bearing running cooler is supported by an analysis of the inner ring temperatures where it is shown that the hybrid runs roughly 1.8°C (3.3°F) cooler than the steel bearing. This difference is likely too small to make a significant impact on cooling system requirements.

Table 3. Test Points 37 through 72 of 120-mm Bore Test, Bearing P05

Test Point	Shaft Speed, rpm	Axial Load, kN (lbf)	Oil Flow, cm ³ /s (gpm)	Oil Inlet Temperature, °C (°F)
37	12,500	4.44 (1000)	126.2 (2.0)	121 (250)
38	12,500	4.44 (1000)	94.7 (1.5)	121 (250)
39	12,500	4.44 (1000)	63.1 (1.0)	121 (250)
40	12,500	22.24 (5000)	126.2 (2.0)	121 (250)
41	12,500	22.24 (5000)	94.7 (1.5)	121 (250)
42	12,500	22.24 (5000)	63.1 (1.0)	121 (250)
43	18,750	4.44 (1000)	126.2 (2.0)	121 (250)
44	18,750	4.44 (1000)	94.7 (1.5)	121 (250)
45	18,750	4.44 (1000)	63.1 (1.0)	121 (250)
46	18,750	22.24 (5000)	126.2 (2.0)	121 (250)
47	18,750	22.24 (5000)	94.7 (1.5)	121 (250)
48	18,750	22.24 (5000)	63.1 (1.0)	121 (250)
49	25,000	4.44 (1000)	126.2 (2.0)	121 (250)
50	25,000	4.44 (1000)	94.7 (1.5)	121 (250)
51	25,000	4.44 (1000)	63.1 (1.0)	121 (250)
52	25,000	22.24 (5000)	126.2 (2.0)	121 (250)
53	25,000	22.24 (5000)	94.7 (1.5)	121 (250)
54	25,000	22.24 (5000)	63.1 (1.0)	121 (250)
55	12,500	4.44 (1000)	126.2 (2.0)	65 (150)
56	12,500	4.44 (1000)	94.7 (1.5)	65 (150)
57	12,500	4.44 (1000)	63.1 (1.0)	65 (150)
58	12,500	22.24 (5000)	126.2 (2.0)	65 (150)
59	12,500	22.24 (5000)	94.7 (1.5)	65 (150)
60	12,500	22.24 (5000)	63.1 (1.0)	65 (150)
61	18,750	4.44 (1000)	126.2 (2.0)	65 (150)
62	18,750	4.44 (1000)	94.7 (1.5)	65 (150)
63	18,750	4.44 (1000)	63.1 (1.0)	65 (150)
64	18,750	22.24 (5000)	126.2 (2.0)	65 (150)
65	18,750	22.24 (5000)	94.7 (1.5)	65 (150)
66	18,750	22.24 (5000)	63.1 (1.0)	65 (150)
67	25,000	4.44 (1000)	126.2 (2.0)	65 (150)
68	25,000	4.44 (1000)	94.7 (1.5)	65 (150)
69	25,000	4.44 (1000)	63.1 (1.0)	65 (150)
70	25,000	22.24 (5000)	126.2 (2.0)	65 (150)
71	25,000	22.24 (5000)	94.7 (1.5)	65 (150)
72	25,000	22.24 (5000)	63.1 (1.0)	65 (150)

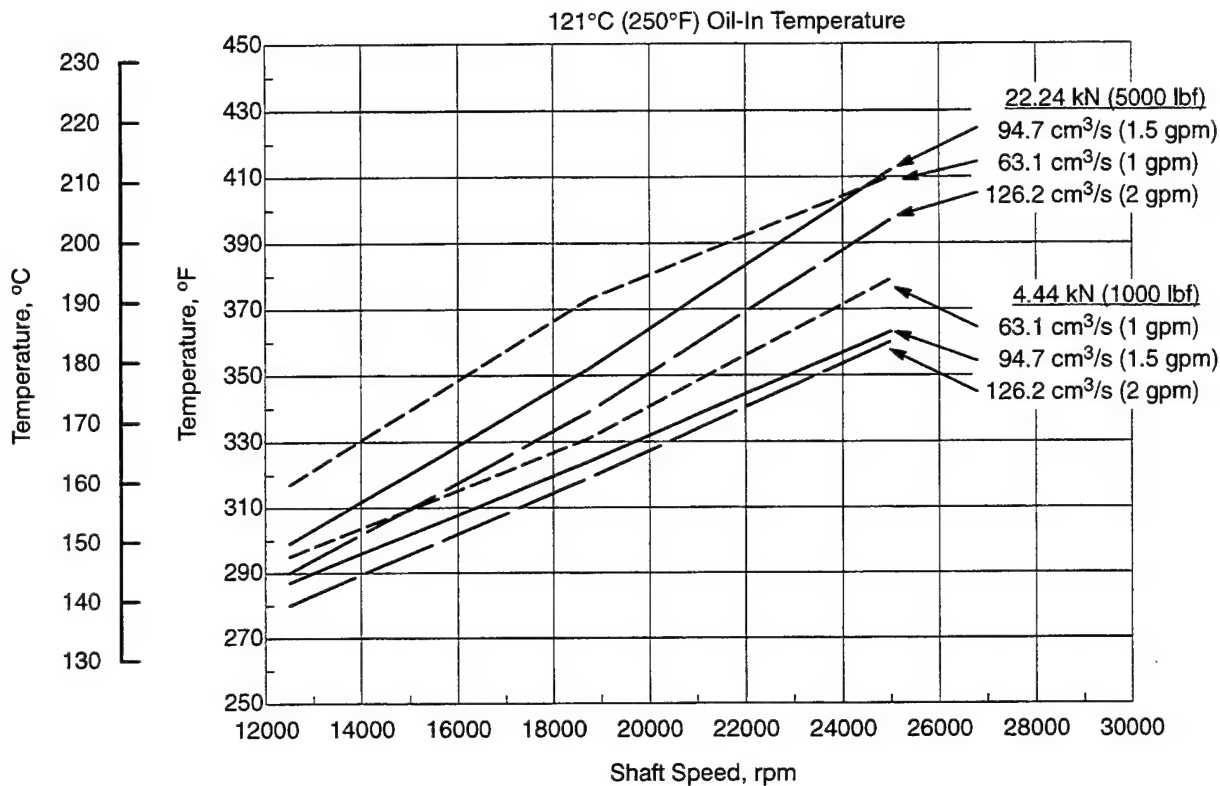


Figure 43. Bearing P05 Outer-Ring Temperature as a Function of Shaft Speed

Figure 44 shows the test rig power draw for the P05 bearing as a function of shaft speed, load, and oil-flow rate. Power requirements generally increase with increasing speed, increasing load, and increasing oil-flow rate, as observed with the P04 bearing. Comparison of the 36 data points indicates that the average power draw between the two bearings is within 1%, with the hybrid bearing requiring the lesser amount. Thus, the power requirements for all practical purposes should be considered equivalent.

Figure 45 shows separator speed ratio as a function of shaft speed, load, and oil-flow rate. At the lower load, it is apparent the hybrid bearing has a lower tendency for slip than the all-steel bearing. This is a potential benefit of a hybrid bearing.

Figure 46 shows hybrid bearing P05 after completion of the 36 test points. Other than some rubbing of the cage against the inner ring land, the bearing is in good condition. This rubbing is thought to be more of an effect of the balance of the cage than any indication of performance of a bearing with silicon nitride balls. Again, as in the P04 data, the rubbing is thought to have had minimal if any effect on the test data.

4.3.3 Tight-Curvature Hybrid Bearing (P06) Data, Points 73 – 90

The next series of 18 tests was designed to determine what, if any thermal penalty, was imposed if the race conformity curvatures were tightened to lower the hertzian contact stress of the hybrid to a value more like that imposed in the all-steel bearing, P04. Table 4 shows the test matrix used for the tight-race-curvature hybrid bearing.

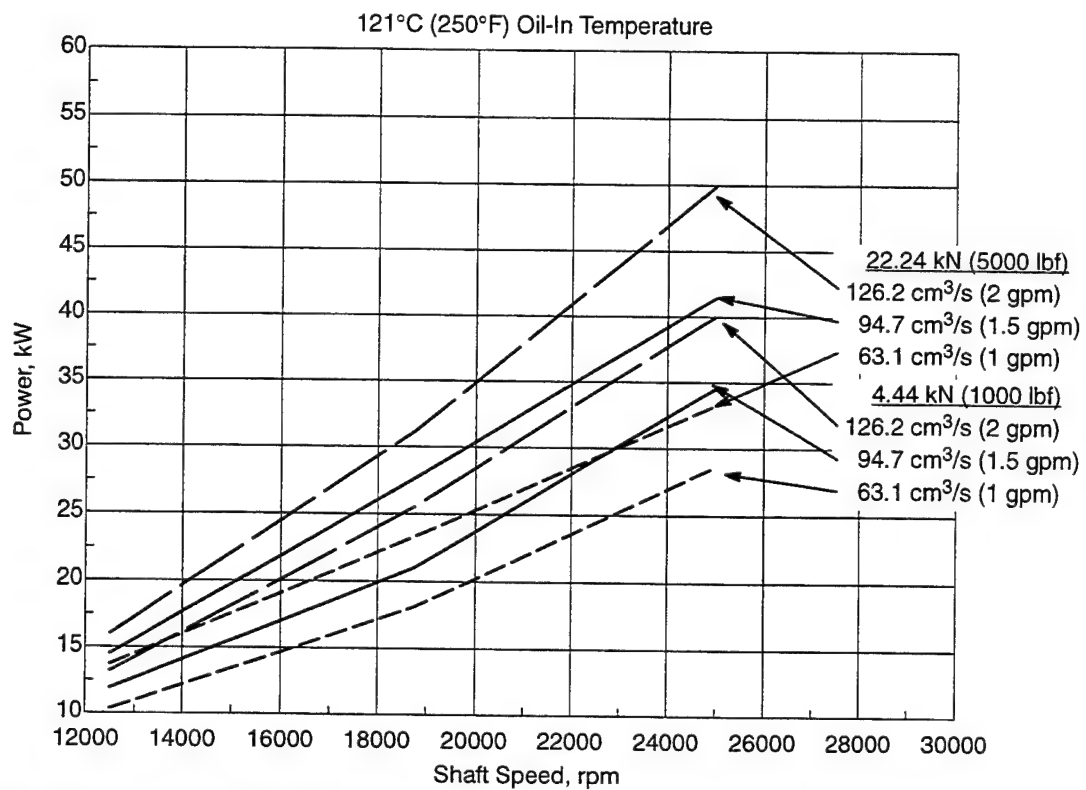


Figure 44. Bearing P05 Rig Power Consumption as a Function of Shaft Speed

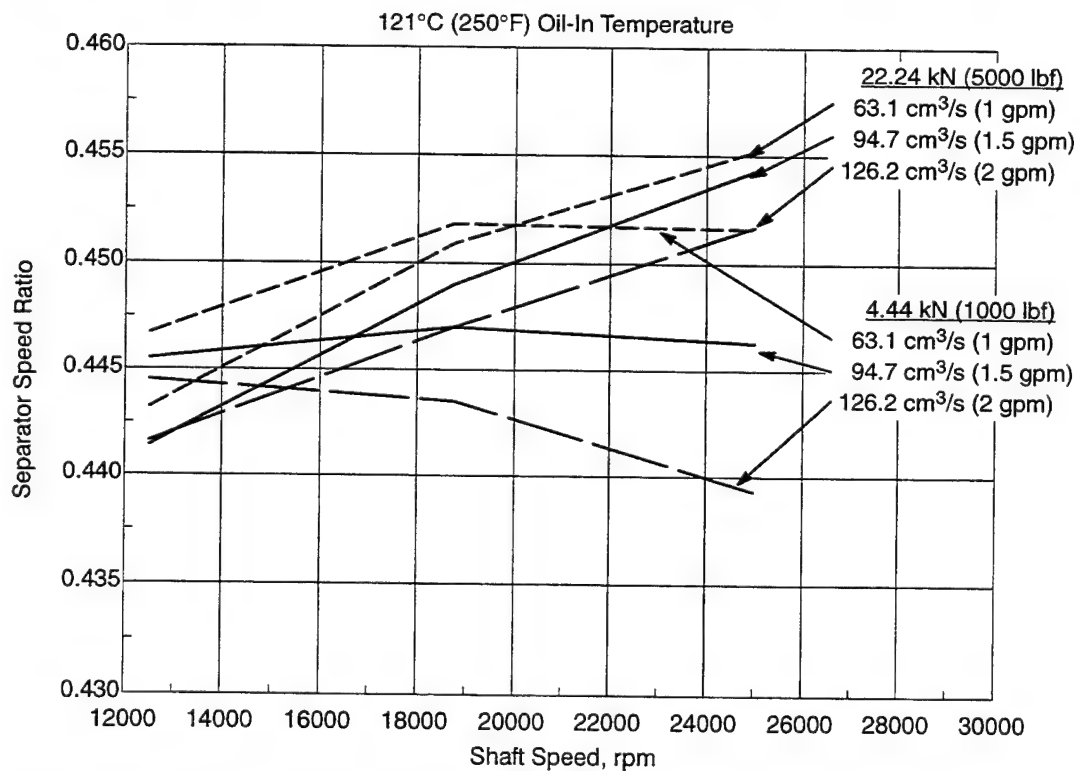


Figure 45. Bearing P05 Separator Speed Ratio as a Function of Shaft Speed

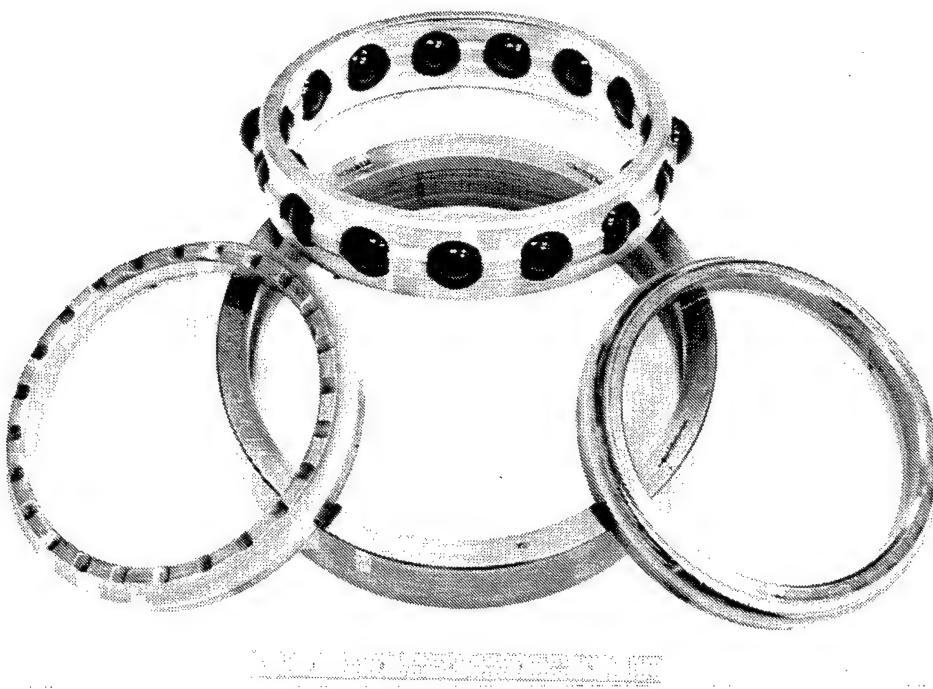


Figure 46. Hybrid Bearing with Silicon Nitride Balls After Completion of Test Points 37 Through 72

Except for slight cage rubbing, this bearing is in good condition. Although the data did not indicate large temperature differences, this bearing did not take on as much straw-yellow coloration as bearing P04, indicating it may have run cooler. The raceway and lands are TDC plated.

Table 4. Test Points 73 through 90 of 120-mm Bore Test, Bearing P06

Test Point	Shaft Speed, rpm	Axial Load, kN (lbf)	Oil Flow, cm ³ /s (gpm)	Oil Inlet Temperature, °C (°F)
73	12,500	4.44 (1000)	126.2 (2.0)	121 (250)
74	12,500	4.44 (1000)	63.1 (1.0)	121 (250)
75	12,500	22.24 (5000)	94.7 (1.5)	121 (250)
76	18,750	4.44 (1000)	94.7 (1.5)	121 (250)
77	18,750	22.24 (5000)	126.2 (2.0)	121 (250)
78	18,750	22.24 (5000)	63.1 (1.0)	121 (250)
79	25,000	4.44 (1000)	126.2 (2.0)	121 (250)
80	25,000	4.44 (1000)	63.1 (1.0)	121 (250)
81	25,000	22.24 (5000)	94.7 (1.5)	121 (250)
82	12,500	4.44 (1000)	94.7 (1.5)	65 (150)
83	12,500	22.24 (5000)	126.2 (2.0)	65 (150)
84	12,500	22.24 (5000)	63.1 (1.0)	65 (150)
85	18,750	4.44 (1000)	126.2 (2.0)	65 (150)
86	18,750	4.44 (1000)	63.1 (1.0)	65 (150)
87	18,750	22.24 (5000)	94.7 (1.5)	65 (150)
88	25,000	4.44 (1000)	94.7 (1.5)	65 (150)
89	25,000	22.24 (5000)	126.2 (2.0)	65 (150)
90	25,000	22.24 (5000)	63.1 (1.0)	65 (150)

Figure 47 compares the outer race temperature of the P06 bearing to that of the P05 bearing as a function of shaft speed, load, and oil-flow rate. The P06 data points are indicated by the triangular symbols and dashed lines. It is evident that the P06 bearing operates at a higher temperature than the P05 bearing. This is most pronounced at the higher shaft speeds. The P06 bearing on average runs 6.4°C (11.6°F) hotter than the P05 bearing. Thus, tightening the race curvature to lower the hertzian contact stress to near that of a steel bearing carries an associated penalty of an increase in operating temperature.

P05 and P06 bearing power consumptions are compared in Figure 48. The P06 data points are indicated by triangular symbols and dashed lines. It is evident that the P06 bearing requires a greater amount of drive power than does the P05 bearing, and the increase is on average about 9%.

Figure 49 compares the cage to shaft speed ratios of the P05 and P06 bearings as a function of shaft speed, load, and oil-flow rate. The P06 data points are indicated by triangular symbols and dashed lines. The P06 bearing has approximately a 0.005 increase in cage/shaft speed ratio relative to the P05 bearing.

Figure 50 shows the two P06 bearings after completion of the 18 test points. With the exception of a few cage/inner race land rubs (as noted in the P04 and P05 bearings), the bearings are in relatively good condition. The fact that the P04 and P06 bearings were running hotter than the P05 is further illustrated by comparing the temperature discoloration of the three. The P04 and P06 bearings show a definite temperature discoloration, but the P05 bearing has only a very slight discoloration from when it was new.

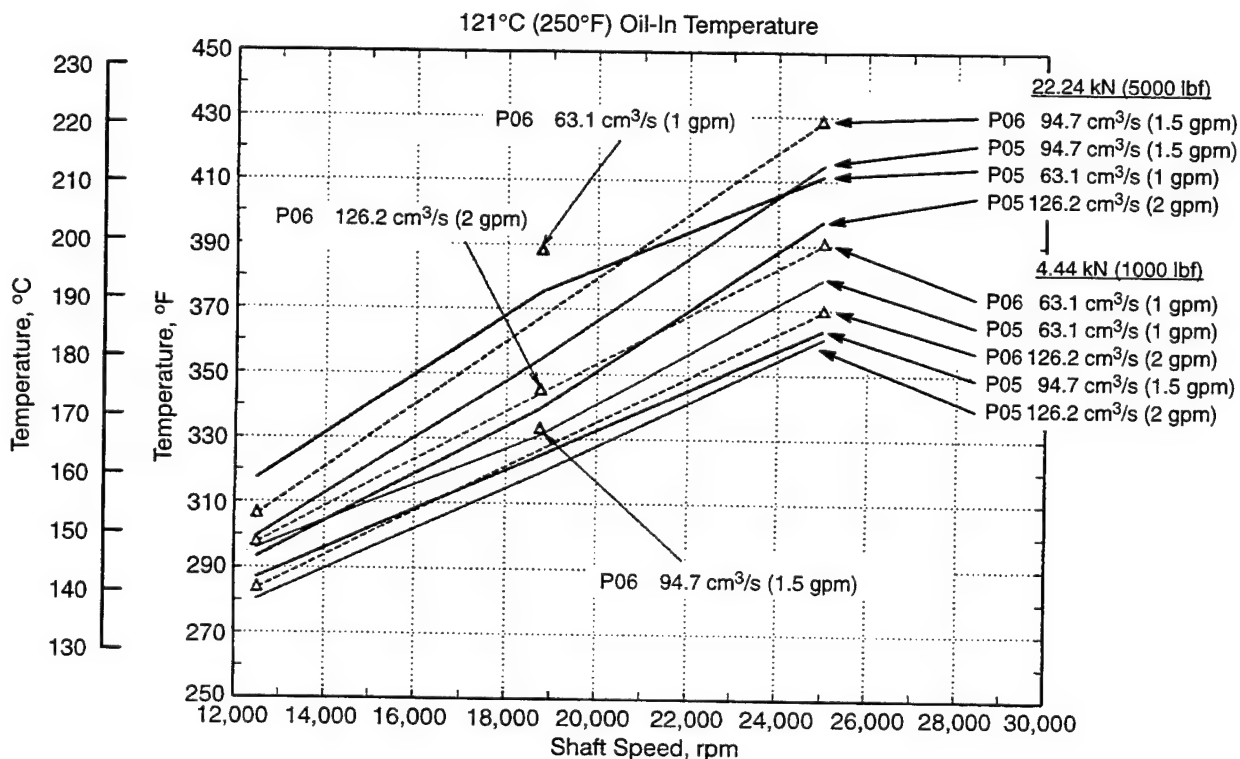


Figure 47. Comparison of Bearing P05 and P06 Outer-Ring Temperatures

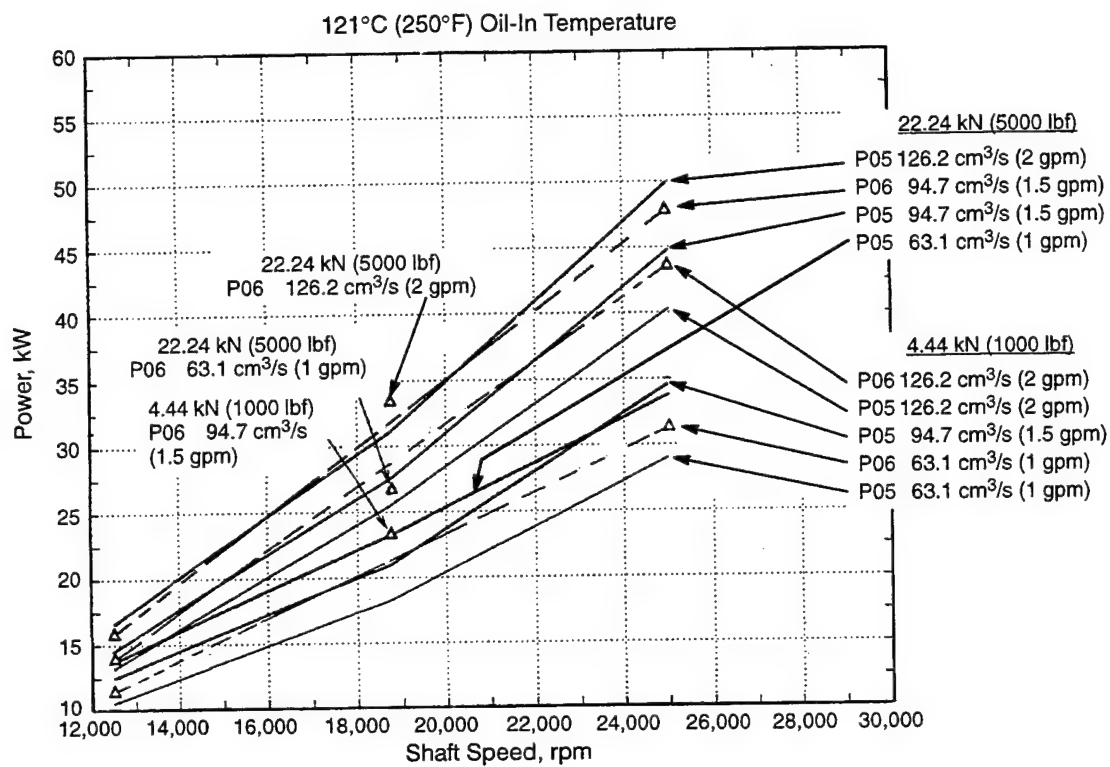


Figure 48. Comparison of Bearing P05 and P06 Rig Power Consumption

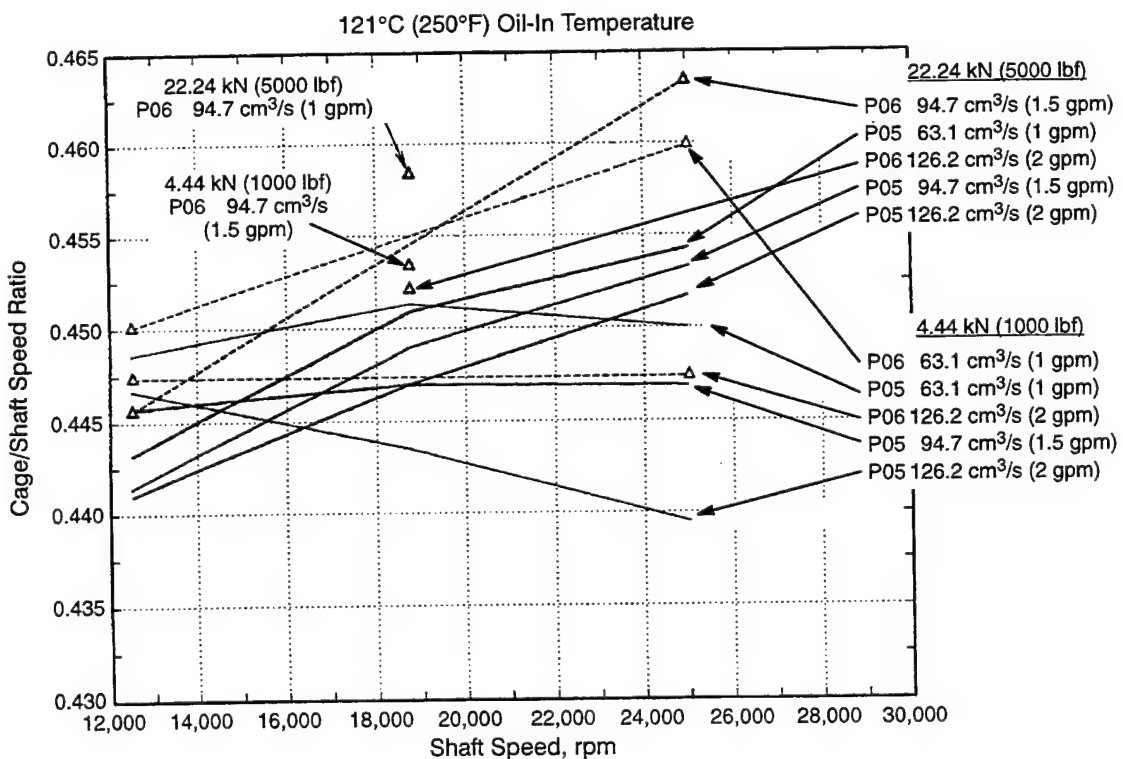


Figure 49. Comparison of Bearing P05 and P06 Separator Speed Ratios



A color image is presented in Reference 1.

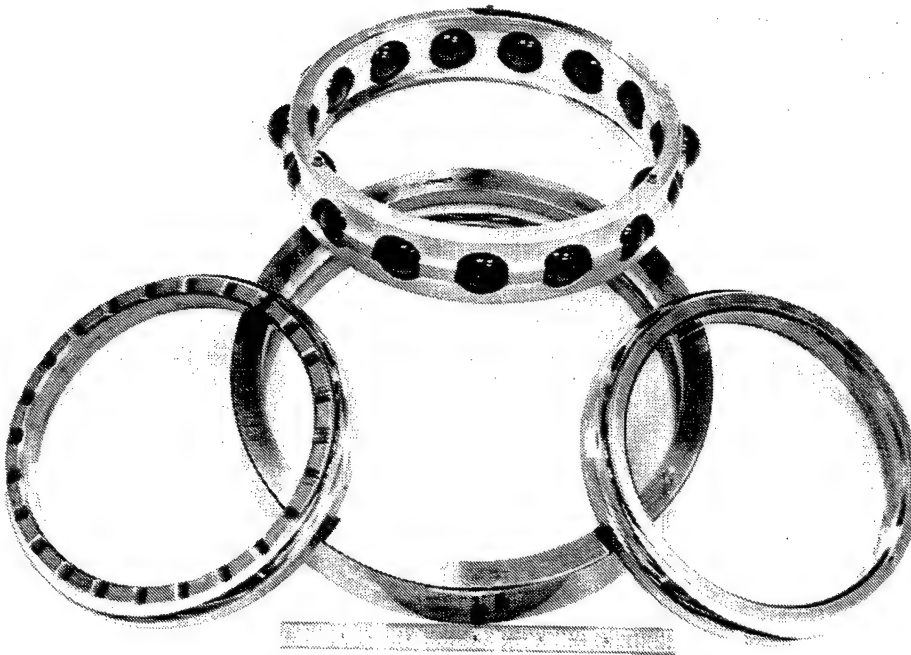


Figure 50. Tight-Curvature Hybrid Bearing After Completion of Test Points 73 Through 90
This bearing is also in good condition. Discoloration (heat tint) is somewhere between that of the open-curvature, all-steel and open-curvature, hybrid bearings.

4.3.4 Reduced Oil-Flow Rate Data (P04 and P05), Points 91 Through 101

To this point in the high-speed testing, the data failed to show significant benefit for a hybrid bearing compared to an all-steel bearing. However, posttest bearing evaluations did indicate that the hybrid bearings, and in particular the P05 bearing, ran cooler than the all-steel bearing. It was decided that the most probable benefit would come in the area of reduced oil-flow rates or oil-out conditions. Therefore, a series of tests was designed in an attempt to illustrate the benefits of a hybrid bearing.

Table 5 shows the conditions for the last 14 tests of this task. Note that the oil-flow rates through the ring are significantly less than in the prior 90 test points. A primary difference in this test is that the bearing types were mixed on the rig and run simultaneously. The P04 bearing was placed on the drive end of the rig, while the P05 bearing was placed on the load end of the rig. It is also important to note that the load end of the rig typically ran about 1.8°C (3.2°F) hotter than the drive end of the rig. This is important when it comes to comparing the P04 and P05 outer-race temperatures. Another difference in this last set of tests was the use of a lower mass (lighter) cage, which was used during NASA testing in the 1970's. This cage lacks the ball-retention feature of the cage used in the first 90 tests.

Table 5. Test Points 91 through 104 of 120-mm Bore Test, Bearing P04 and P05

Test Point	Shaft Speed, rpm	Axial Load, kN (lbf)	Oil Flow, cm ³ /s (gpm)		Oil Inlet Temperature, °C (°F)
			Through the Inner Ring	Outer Ring Cooling	
91	18,750	4.44 (1000)	32 (0.50)	32 (0.50)	121 (250)
92	18,750	4.44 (1000)	16 (0.25)	32 (0.50)	121 (250)
93	18,750	4.44 (1000)	32 (0.50)	0	121 (250)
94	18,750	22.24 (5000)	32 (0.50)	32 (0.50)	121 (250)
95	18,750	22.24 (5000)	16 (0.25)	32 (0.50)	121 (250)
96	18,750	22.24 (5000)	32 (0.50)	0	121 (250)
97	25,000	4.44 (1000)	32 (0.50)	32 (0.50)	121 (250)
98	25,000	4.44 (1000)	16 (0.25)	32 (0.50)	121 (250)
99	25,000	4.44 (1000)	32 (0.50)	0	121 (250)
100	25,000	22.24 (5000)	32 (0.50)	32 (0.50)	121 (250)
101	25,000	22.24 (5000)	16 (0.25)	32 (0.50)	121 (250)
102	25,000	22.24 (5000)	32 (0.50)	0	121 (250)
103	25,000	22.24 (5000)	63 (1.00)	0	121 (250)
104	25,000	22.24 (5000)	126 (2.00)	0	121 (250)

Comparison of the outer ring temperature of test point 91 through 98 indicates an average spread of 4.8°F (8.7°F) between the two bearings, with the hybrid running cooler.

At test point 99, testing was aborted due to an over-temperature condition of the all-steel bearing. At the point the P04 bearing hit the preset temperature limit of 218°C (425°F), the P05 bearing was operating roughly 10°C (18°F) cooler. Figure 51 is a historical plot of test point 99. The conditions of this test were 4.44 kN (1000 lbf) axial load, 25,000 rpm shaft speed, 32 cm³/s (0.5 gpm) inner-ring oil flow, and no outer-ring cooling.

Test point 100 was completed without incident; the temperature difference between the P04 and P05 bearings was roughly 8.3°C (15°F).

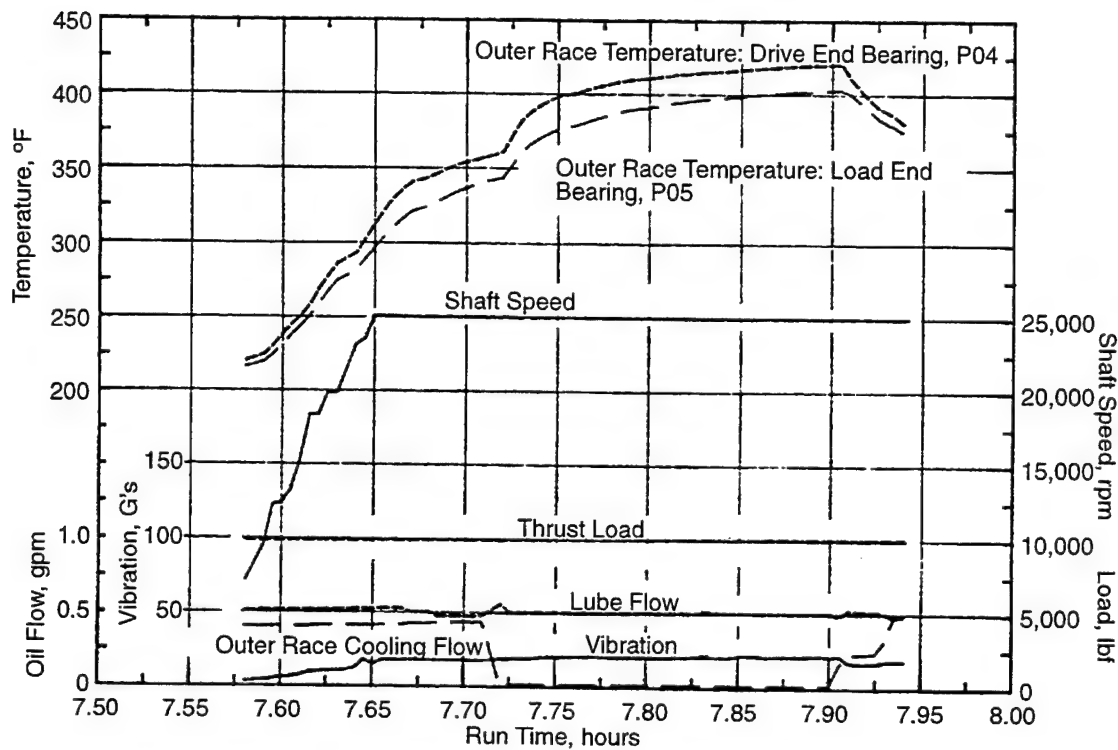


Figure 51. Historical Plot of Test Point 99 Variables

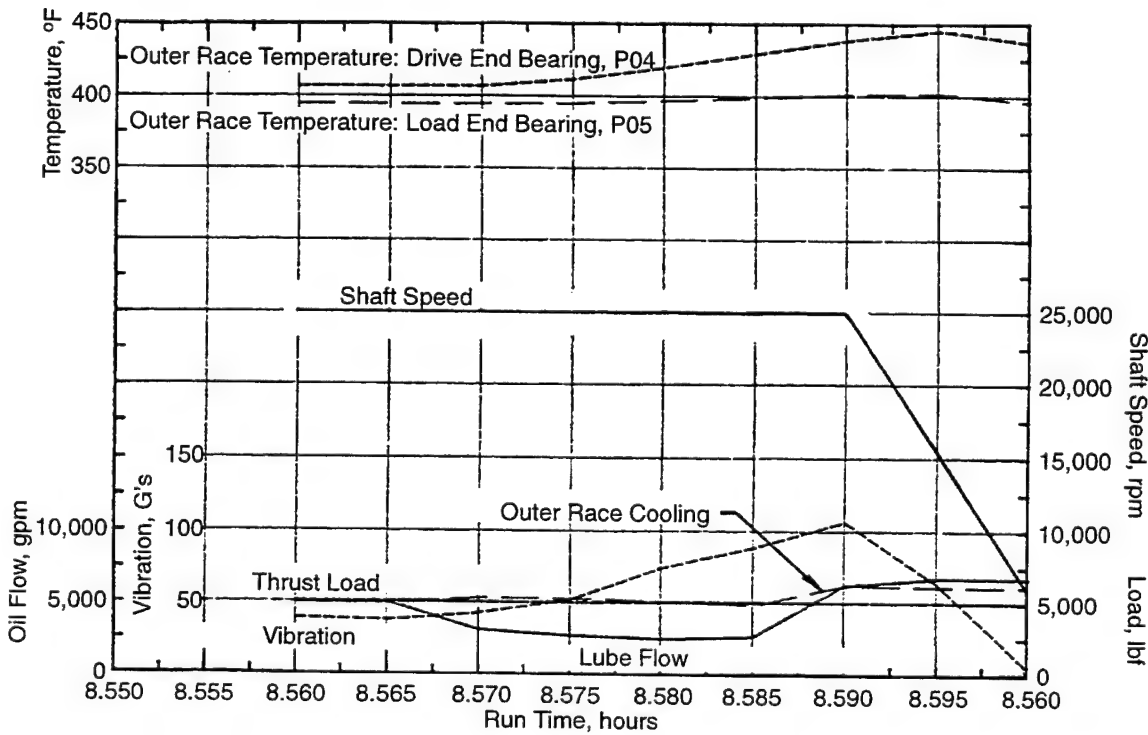


Figure 52. Historical Plot of Test Point 101 Variables

Test point 101 was performed at an axial load of 22.24 kN (5000 lbf), 25,000 rpm shaft speed, 16 cm³/s (0.25 gpm) inner-ring oil flow, and 0.5 cm³/s (0.5 gpm) outer-ring cooling. Figure 52 is a historical plot of test point 101. Because lube flow is lower than in the previous test, the temperature difference of the two bearings starts to become significant. By the time the desired lube flow is reached, the P04 bearing is already running with an outer ring temperature of 223°C (433°F), which is roughly 19.4°C (35°F) hotter than the hybrid P05 bearing. At that point, procedures are being taken to save the bearing, such as increasing lube flows to both the inner and outer rings. By this time the P04 bearing is at 230°C (445°F).

Upon inspection of the two bearings the following observations were made.

The P05 hybrid bearing exhibited a normal-looking wear track and appeared not to have exceeded 204°C (400°F), as shown in Figure 53. The silicon nitride balls measured 20.6 mm (0.8125 in), indicating no wear. The cage contained a minor scuff mark on the land riding surface through a 90° arc. These scuffs may have occurred during the last moments of operation in which the rig was experiencing high levels of vibration due to the failure of the all-steel P04 bearing.

The P04 bearing outer ring exhibited a uniform track, indicating proper alignment, with a wide ball path caused by the shifting ball angle and eventual loss of diametral clearance due to overheating of the bearing. Signs of overheating can be seen in Figure 54. The inner ring also exhibited a uniform track, with a darkened ball path passing from the thrust loaded half of the split inner ring across the split line and onto the typically unloaded half of the inner ring, which indicates that diametral clearance had been lost, as shown in Figure 55. The balls from the P04 bearing appear to be in good condition, except for the black color due to overheating. It is estimated that the surface temperatures of the balls exceeded 371°C (700°F).

A color image is presented in Reference 1.



Figure 53. Hybrid Bearing with Silicon Nitride Balls (P05) After Completion of Test Points 91 Through 101 Except for scuff marks on the cage, the bearing is in good condition. The absence of discoloration indicates low heat generation.

A color image is presented in Reference 1.

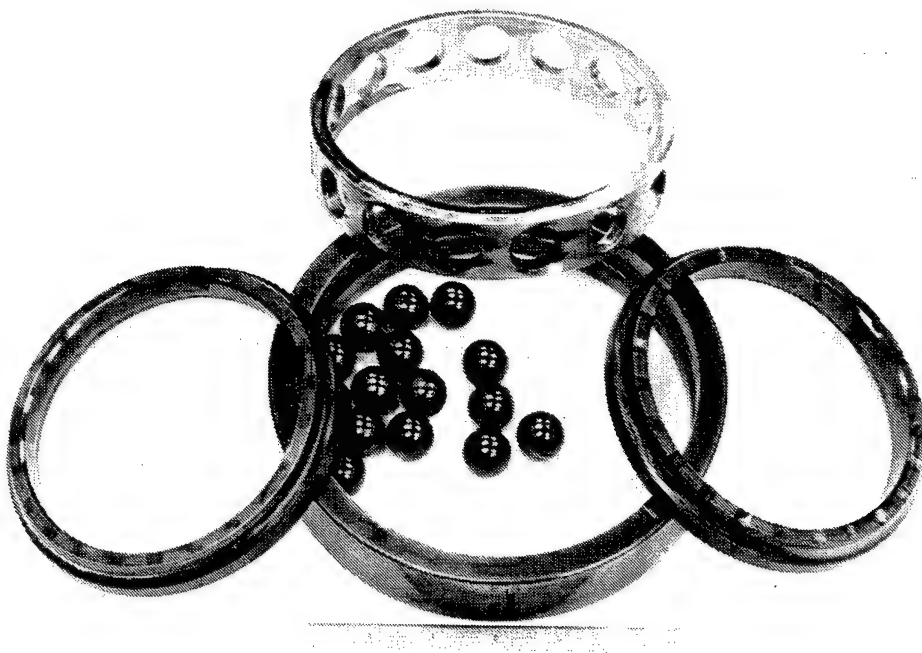


Figure 54. Disassembled Bearing After Test Point 101 The balls of this all-steel bearing have taken on a black discoloration due to excessive heat generation. This bearing evidently ran considerably hotter than the P05 hybrid that was run simultaneously.

A color image is presented in Reference 1.

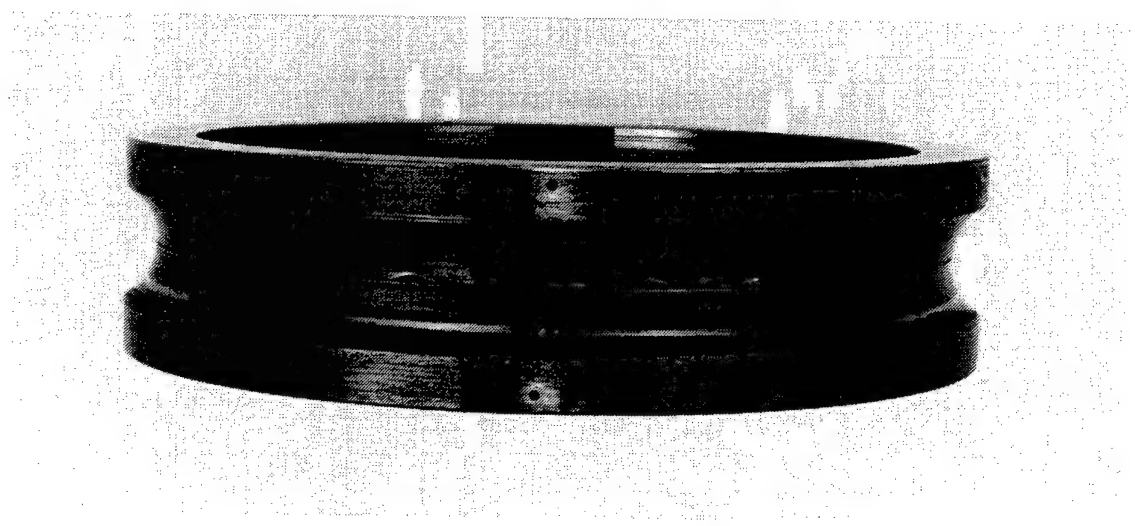


Figure 55. Inner Ring of P04 Bearing The ball path has traversed the split line and is contained on both the inner and the outer halves. (This supports the conclusion that loss of diametral clearance was due to overheating of the bearing.) As the balls pass over the lubrication slots in the inner ring, a high level of vibration would be expected.

The M50 balls also measured 20.6 mm (0.8125 in), indicating no wear had occurred. The cage contained a severe rub through a 180°, arc as seen in Figure 56, but did not contain any opposing rub marks that would indicate cage lockup. The inner- and outer-ring lands and rubbed area of the cage appear to have operated at temperatures in excess of 371°C (700°F). Figure 57 shows the assembled P04 bearing with varying degrees of heat tinting. Dimensional inspection of the cage indicated the silver plate and roughly 0.3 mm (0.012 in) of the 4340 cage material were removed during this rubbing.

The following is offered as the sequence of events that lead to the run-away temperature condition of the all-steel P04 bearing. Running under conditions of high loads, high speeds, and reduced oil flow, the M50 ball to M50NiL/TDC (thin dense chrome) race finally shifted from a condition of partial elastohydrodynamic (EHD) film to one of mostly metal-to-metal contact. This in turn resulted in high traction forces and high rates of heat generation. As the temperature of the bearing increased, the hydrodynamic (HD) film between the inner-race land and the cage-riding land surface broke down to a point where there was also metal-to-metal contact (TDC to silver). The soft silver was easily rubbed away, causing a significant imbalance of the cage which further propagated the rubbing action and heat generation between the inner race and the cage.

It is important to note that both the hybrid P05 and the all-steel P04 bearing were dimensionally equivalent, the cages were balanced against the same specification, and both bearings had successfully completed 7.5 hours of testing at speeds of 18,750 to 25,000 rpm without incident. Only under the combination of a 22.24 kN (5000 lbf) axial load, a speed of 25,000 rpm (3.0 MDN), and reduced oil flow to the inner ring did the temperature between the two bearings start to differ significantly. Under these severe operating conditions it had been anticipated the hybrid bearing would exhibit improved performance, as has been indicated by the last series of tests in Task 2.

An internal study at GEAE confirmed that the all-steel bearing would be expected to run out of internal clearance before the hybrid bearing and that the hybrid bearing may be able to operate at up to 30°C (55°F) hotter for this particular configuration before it would have run out of clearance. This study confirms the results of testing at ITBC.

Appendix A presents the thermal performance, cage speed ratio, and power draw data for test points 1 through 101.

4.4 Task 2 Conclusions

- At normal engine operating conditions, hybrid bearings offer little, if any, improvement in thermal performance over an all-steel bearing.
- Hybrid bearings with tightened race curvatures operate at higher temperatures than either the open-curvature hybrid bearing or the all-steel bearing.
- Hybrid bearings are capable of sustained operation at reduced oil-flow rates.

4.5 Recommendations

It is recommended that additional tests be performed to quantitatively assess the oil-off or oil-out benefits of a hybrid bearing. If a hybrid does in fact run cooler than an all-steel bearing, one might expect a better lube film thickness and therefore longer life with a hybrid bearing. Testing is needed to evaluate this possibility.

A color image is presented in Reference 1.



Figure 56. Cage from Bearing P04 *The severe rub on the inner ring may be due to large vibrations caused by the balls passing over the lube slots.*

A color image is presented in Reference 1.

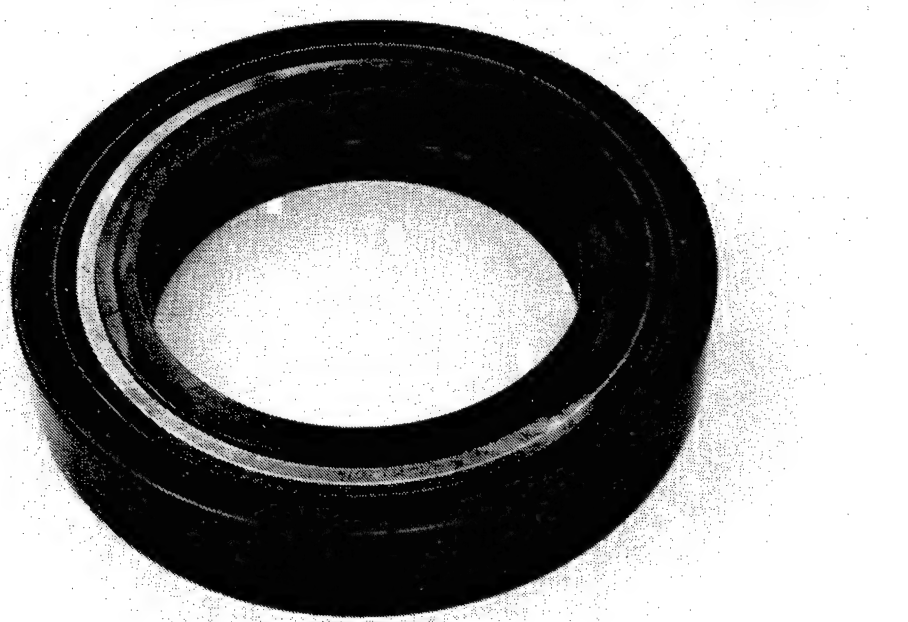


Figure 57. Assembled P04 Bearing After Completion of Test Point 101 *There is considerable heat discoloration.*

5.0 Task 3 – Bearing Condition Monitoring

5.1 Objective

The objective of this task was to research various candidate condition-monitoring methods in terms of timely detection of incipient failure of hybrid ceramic bearings. The approach was to:

- assess performance of two methods on a flow bench in prototype form and later in a bearing test rig,
- evaluate the most promising method against vibration-detection techniques during a bearing rig test, and
- recommend potential further work necessary to transition a prototype system into a product engine application.

It is important to note that various techniques are used to detect magnetic debris from a bearing, but few if any are also capable of detecting silicon nitride debris. Thus, it is necessary to evaluate and develop techniques that are capable of detecting the early stages of Si_3N_4 rolling-element failure.

5.2 Technology Assessment

A Defense Technical Information Center (DTIC) literature search on “Wear Debris Oil Condition Monitoring” was conducted. Several important articles were reviewed, and a comprehensive matrix of 21 techniques was compiled (Appendix B). From this matrix, techniques that show potential were selected for further investigation. The following selection criteria were evaluated:

- cost,
- reliability,
- full-flow monitoring capability,
- on-line operation,
- real-time detection,
- capability to detect debris size $> 200 \mu\text{m}$,
- early warning (indication after 10 chips),
- current availability (low-risk technology), and
- capability of detecting metallic and nonmetallic debris.

The techniques selected for further investigation were:

- ultrasonic-pulse echo with a full-flow, debris-retention screen,
- photoelectric sensing — using various light sources — with a full-flow, debris-retention screen,
- vibration monitoring, and
- radioactive doping.

The ultrasonic-pulse echo and photoelectric sensing (using various light sources) detection techniques assessed the change in signal over a 7.62 mm (0.30 in) diameter screen area as debris was

collected. The design goal of the debris collector was such that full oil flow was maintained while focusing the debris onto a much smaller “reference screen” area that could be assessed by the ultrasonic/light probes. These techniques would detect both ceramic and metallic debris larger than the retention screen mesh rating. Appendix C is a report, “Ultrasonic Scattering by Ceramic Debris in Oil,” prepared for GEAE by Dr. Haydn N.G. Wadley of the University of Virginia as part of our risk-reduction activities.

Dr. Wadley also investigated the feasibility of low-level radioactive doping of finished silicon nitride rolling elements (Appendix D). He concluded that no long-lived, γ -emitting radioisotopes (half life >5 to 10 years) are produced by neutron absorption for any of the elements that compose the material GEAE is using (silicon, nitrogen, magnesium, and oxygen, Cerbec’s NDB-200). It appears the only possibility would be to introduce a γ -emitting impurity into the top 50 to 100 μm of the rolling elements. One such impurity, cobalt 59, when neutron irradiated, forms radioactive cobalt 60 with a half life of 5.2 years. Of course, this approach could only be considered if the impurity has no detrimental effect on bearing integrity. Calculations show, however, that if the dosage level, detector location, and sensitivity are optimized, inherent safety concerns could be significantly reduced, so radioactive doping may warrant further investigation at a later date. No further research was done at this time on the feasibility of this technology since it was beyond the scope of the program.

In addition to the above techniques, a fiber-optic, bearing-deflection sensor was evaluated during induced-defect testing. This probe monitored bearing outer race support ring deflection during the progression of bearing failure. As the bearing degraded, changes in vibrational amplitude were detected by a contact probe that monitored local bearing deflections. A traditional accelerometer was mounted close to this device for comparative purposes. Additionally, an SKF condition-monitoring expert was on site to monitor the progression of the final induced-defect test.

5.3 Risk-Reduction Experiments

Several experiments were conducted in a subscale laboratory setting to reduce the risk and increase the probability of success of the prototypes to be built. Various tests were conducted to study the influence of:

- stainless steel versus fluorocarbon mesh,
- mesh size,
- ultrasonic frequency,
- transducer-to-screen separation distance,
- effect of new and used oil, and
- HeNe laser, red LED (light-emitting diode), infrared light sources.

Based on the findings of initial testing, the final selections for the two prototypes were made. Details of the experiments and results are presented in Appendix E.

5.4 Selection of Prototypes

Two experimental techniques were selected for prototype evaluation:

1. ultrasonic-pulse echo with a full-flow, debris-retention screen (UT), and
2. infrared photoelectric sensing with a full-flow, debris-retention screen (IR).

Two commercially available devices were also evaluated:

3. deflectometer from Philtek Inc. (Arnold, MD) and
4. vibration-monitoring device from SKF Condition Monitoring (San Diego CA).

5.5 Prototype 1 Evaluation: UT Device

5.5.1 Overview of Technique

The proposed chip detector worked on the principle of a traditional in-line, full-flow filter. In-line, full-flow filters were placed in a lubrication system to pass 100% of the oil flow. Thus, any particles or chips in the oil that are larger than the filter opening were trapped by the filter. The size of the filter/screen opening determined the smallest size of chip to be detected. The surface of the screen on which the particles collect was continuously monitored by an ultrasonic detection system. Any chip on the surface of the screen caused a change in the reflection of the ultrasonic signal; this change in signal indicated the change of condition of the oil and the ceramic or metallic ball bearing.

5.5.2 Description and Operation

A chip collector was placed in an engine lubrication system so that 100% of the oil flowed through. This chip collector was designed to allow oil to flow sideways as well as to the bottom through fine screens. The screen at the bottom of the chip collector, 7.62 mm (0.3 in) diameter, collected all the chips. An ultrasonic probe was placed above this screen, as shown in Figure 58, such that the ultrasonic energy reflected from the screen was received by the same (transmitting) ultrasonic probe. Any change in the reflected-signal amplitude indicated the presence of metallic or nonmetallic particles on the screen. Figure 59 shows the complete setup with the chip catcher, chip injector, and ultrasonic transducer.

Figures 60 and 61 are photographs of the chip catcher and flow assembly used in this test. One disadvantage of this technique was that any change in the oil flow characteristics, presence of air, etc. changed the reflected signal. To alleviate this weakness and make the detection scheme more

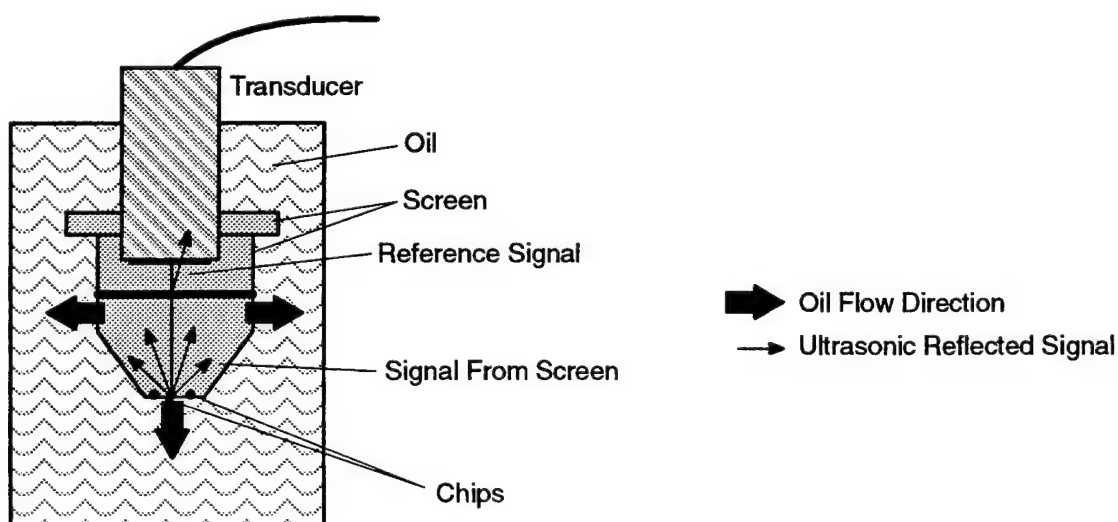


Figure 58. Schematic of UT System Chip catcher and ultrasonic transducer in pulse-echo mode to monitor the change in reflected amplitude from collection screen.

Item No.	Description or Name
2	Inlet Tube
3	Spacer
4	Exit Tube
5	Chip Injector
6	Chip Injector Cap
7	Chip Director
8	Chip Catcher/Collector
10	Clamp
11	SOC HD Shoulder Bolt
12	SOC HD Cap Screw
13	Hex Nut
14	SOC HD Cap Screw
15	SOC HD Cap Screw
16	SOC HD Cap Screw
17	O-Ring
18	O-Ring
19	O-Ring
20	Hex Bolt
21	Ultrasonic Transducer
24	Chip Catcher Screen
25	O-Ring

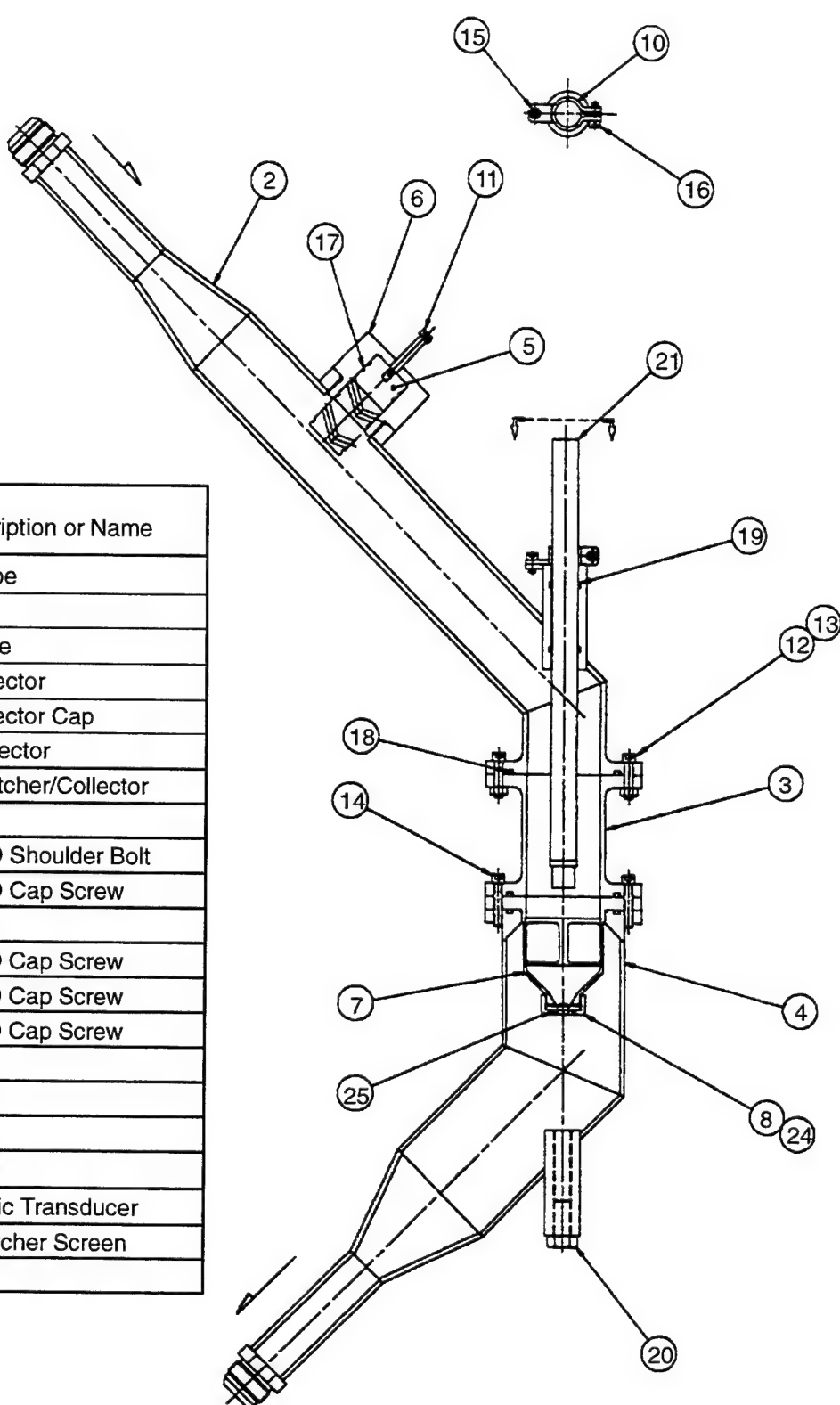


Figure 59. Engineering Drawing of UT System

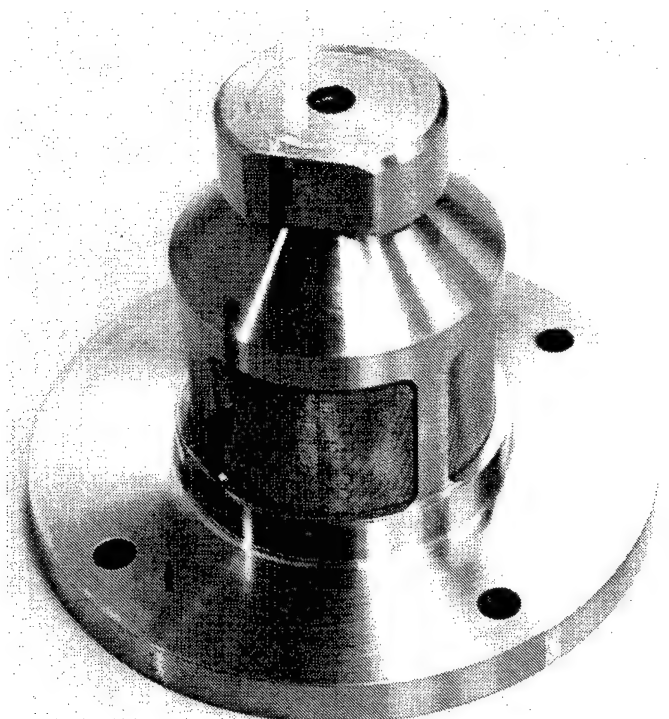


Figure 60. Chip Catcher

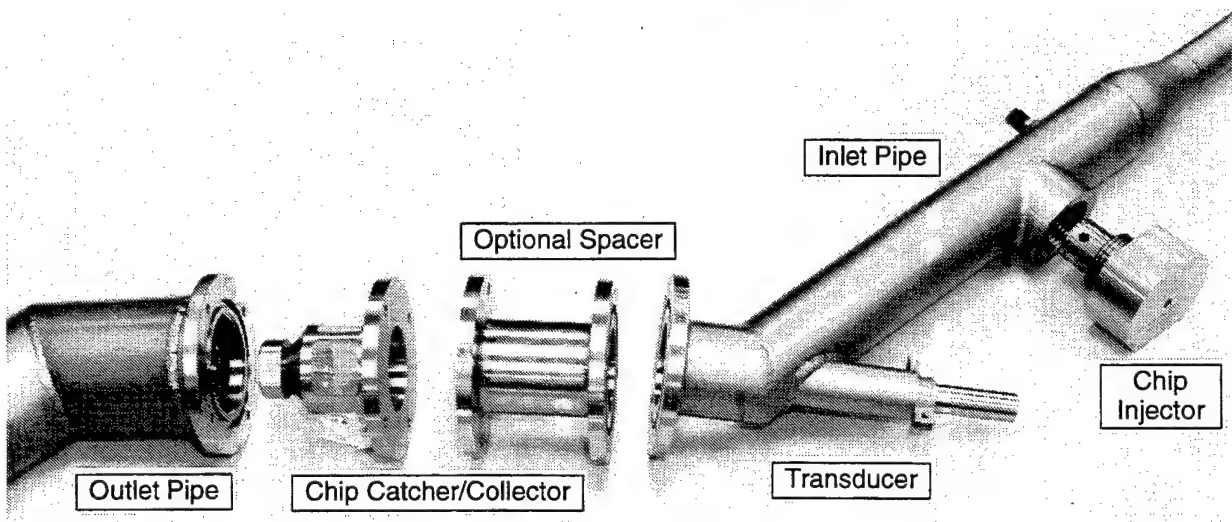


Figure 61. Chip Injector and Chip Catcher Assembly

will change the reflected signal. To alleviate this weakness and make the detection scheme more robust, a reference signal is provided from a stainless steel wire placed ahead of the screen in which chips collect. Rather than merely using the reflected signal from the screen, this reference signal is used to compute a ratio (reflected signal from screen \div reflected signal from stainless steel wire) that is used for the comparison. Sample test results are listed in Table 6.

Table 6 shows the performance of this device in detecting 200- μm ceramic chips, in engine oil, using a 2.25-MHz ultrasonic transducer, at room temperature, under two different flow conditions. The change in the reflection ratio reference/screen signal indicates the presence of chips on the screen.

Table 6. UT Device Sample Test Results

Number of Chips (Ceramic)	Oil Flow, cm ³ /s	Reference From Stainless Steel Wire (Volts)	Reflection from Screen (Volts)	Reflection Ratio Reference/Screen
0	0	1.70	8.1	4.79
10	0	1.62	6.86	4.23
20	0	2.28	6.69	2.93
50	0	1.63	2.88	1.77
0	568	1.72	7.84	4.56
10	568	2.14	8.76	4.09
20	568	2.3	6.60	2.87
50	568	1.66	2.92	1.76

5.5.3 Experiments

5.5.3.1 Initial Tests

To simulate ceramic bearing debris, 1-mm ceramic balls were crushed and 400- μm (nominal) particles were permanently glued to the stainless steel and fluorocarbon meshes to produce repeatable test conditions. Stainless steel screens without chips (bare) and with 10, 20, and 50 chips spread over the screen and concentrated toward the center were used in these tests. Figure 62 is a block diagram of the lubrication system used in this test. Tests were conducted under static or no oil flow to 568 cm³/s (9 gpm), in increments of 189 cm³/s (3 gpm), using both stainless steel and fluorocarbon screens. Due to fluctuations in the oil flow at 379 cm³/s (6 gpm), possibly lubrication system related, the oil flow was changed to 442 cm³/s (7 gpm) to maintain a steadier response. Ultrasonic-pulse echo response (volts) from the reference wire and the screen were collected in two different channels, and the ratio of the two was used to predict the presence of silicon nitride chips on the screen.

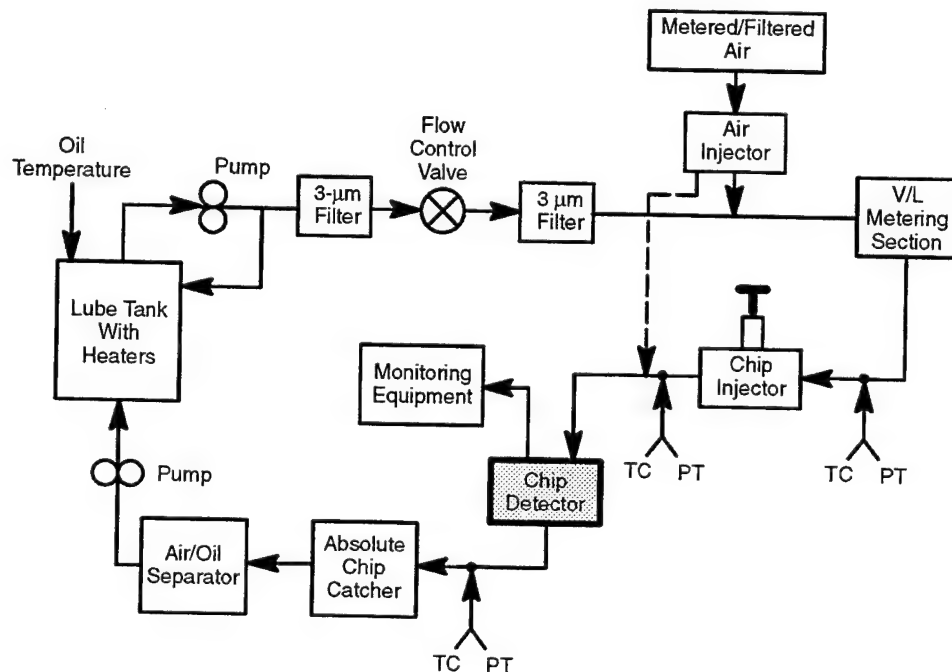


Figure 62. Block Diagram of Lube System Used for Bench Testing

Figure 63 shows the detection capability of the ultrasonic device when only the reference signal was used; the poor correlation was due to trapped air in the oil.

Figure 64 shows the detection capability of the ultrasonic device when the reference signal was used to compensate for variation due to flow, air and temperature. With the reference signal, it was possible to detect 10 to 50 chips, both in the no-oil-flow static condition and up to $568 \text{ cm}^3/\text{s}$ (9 gpm). The influence of air bubbles was thus minimized by the use of a reference signal from a 0.635-mm (0.025-in) stainless steel wire.

Tests were also conducted using the fluorocarbon screen from no flow to $568 \text{ cm}^3/\text{s}$ (9 gpm) in increments of $189 \text{ cm}^3/\text{s}$ (3 gpm). The results of these tests were similar to those with the stainless steel screen, indicating that either stainless steel or fluorocarbon screens could be used to detect 20 chips and greater, under no flow to $568 \text{ cm}^3/\text{s}$ (9 gpm) conditions.

5.5.3.2 Aeration Test

Further testing to study the influence of air and temperature on the detection capability of this prototype were conducted. In this test, small quantities (1 to 2.5%) of air were continuously injected upstream into the oil to study ultrasonic response from the screen and the reference wire. The ratio of the ultrasonic response from the screen to the reference wire degraded significantly as soon as air was injected into the system. This was expected because air is a poor conductor of ultrasonic waves. Hence, the presence of air in the oil should be completely eliminated during assessment of the screen for debris. This was a significant limitation of the technique; however, operating conditions could be identified that resulted in no air being present in the oil while the screen was evaluated for possible ceramic and metallic debris. One such condition could be a shut-down engine ready for ground crew inspection.

The data from the aeration test are summarized in Table 7. The table shows the detection capability of the ultrasonic device when large quantities of air were injected into lubrication system. (V/L = volume % liquid in air + liquid mixture.) The strong influence of entrained air can be seen in the data. The ability to detect chips on the collection screen was severely hindered since the ratio of screen signal to reference signal dropped significantly as airflow increased.

Table 7. Effect of Air Injection on UT Detection Capability
Signal produced by 20 chips on screen No. 5.

Airflow, cm^3/s	V/L, %	Reference Signal, V	Screen Signal, V	S/R Ratio
0.0	100.0	3.77	8.83	2.34
2.5	97.5	0.77	0.50	0.65
2.2	98.5	0.92	0.63	0.68
2.1	99.0	1.41	1.00	0.71

5.5.3.3 Temperature Effects

In this study, the oil temperature was increased to assess influence on the detection capability of the ultrasonic device at temperatures above room temperature to 121°C (250°F). The ratio of the ultrasonic response from the screen to the reference wire remained fairly constant; hence, the influence of oil temperature was minimal. This was considered a significant positive finding, leaving us to contend primarily with entrained air. Table 8 is a summary of the oil-temperature study.

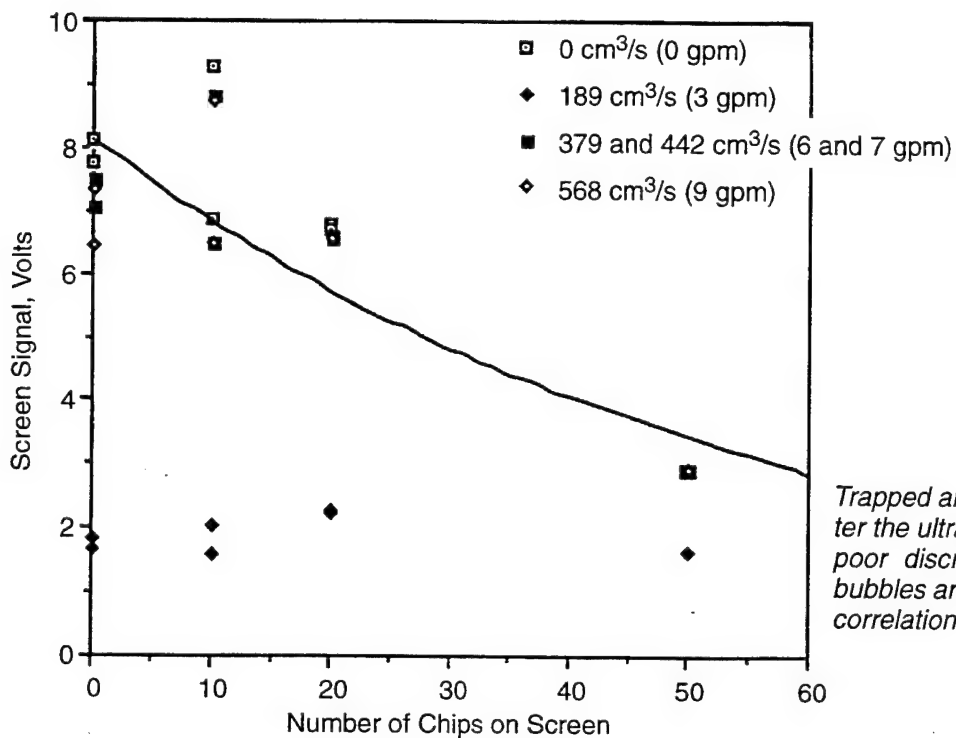


Figure 63. Uncompensated Signal from the Screen at Various Test Conditions

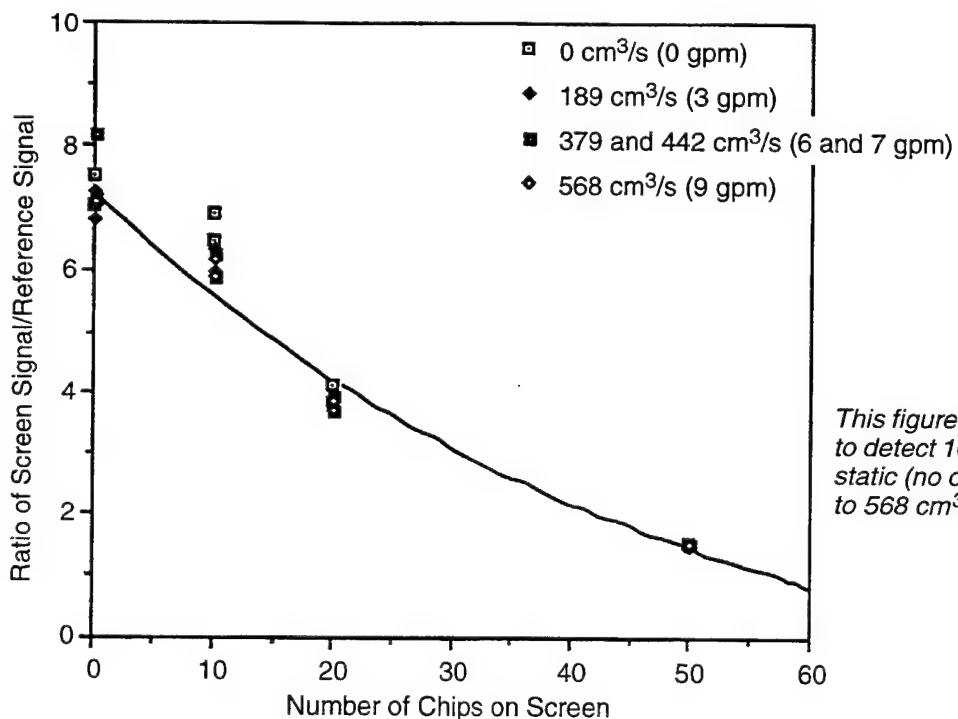


Figure 64. Ratio of Signal from the Screen to the Reference Signal for Various Test Conditions

Table 8. Performance of the UT Device when the Oil Temperature was Varied *Signal produced by 20 chips on screen No. 5, 100% V/L. Results show stable behavior after the signal was corrected by the reference signal; S/R ratio shows little change.*

Oil Temperature, °C	Reference Signal, V	Screen Signal, V	S/R Ratio
49	3.17	6.74	2.13
54	3.05	6.65	2.18
60	2.93	6.54	2.23
66	2.65	6.02	2.27
71	2.26	5.31	2.35
77	2.09	4.93	2.36
82	1.91	4.50	2.36
88	1.81	4.30	2.38
93	1.73	4.17	2.41
100	1.68	4.06	2.42
108	1.61	3.89	2.42
117	1.46	3.60	2.47

Although the effect of temperature on the “ratio” of the UT response of the screen to that of the reference wire was minimal, the decision to use the reference wire was further supported by the evidence that the individual UT response was affected by temperature variations.

5.5.3.4 Chip Injector Evaluation

Having demonstrated significant success with the ultrasonic device while looking at screens with affixed chips, it was time to assess the ability of the chip injector to deliver chips to the screen and the ability of the UT technique to detect loose chips in the system. Thus, the chip injector was loaded with between 30 and 50 chips (300 to 500 μm diameter) tested to investigate both questions. Ultrasonic responses from the reference wire and collection screen were recorded on a strip-chart recorder plotting the UT responses as functions of time. Figure 65 is a sample strip-chart recording.

A large drop in the signal was noticed as soon as the chip injector was activated — because a large quantity of air was injected into the system as well. After several minutes, a steady-state was reached,

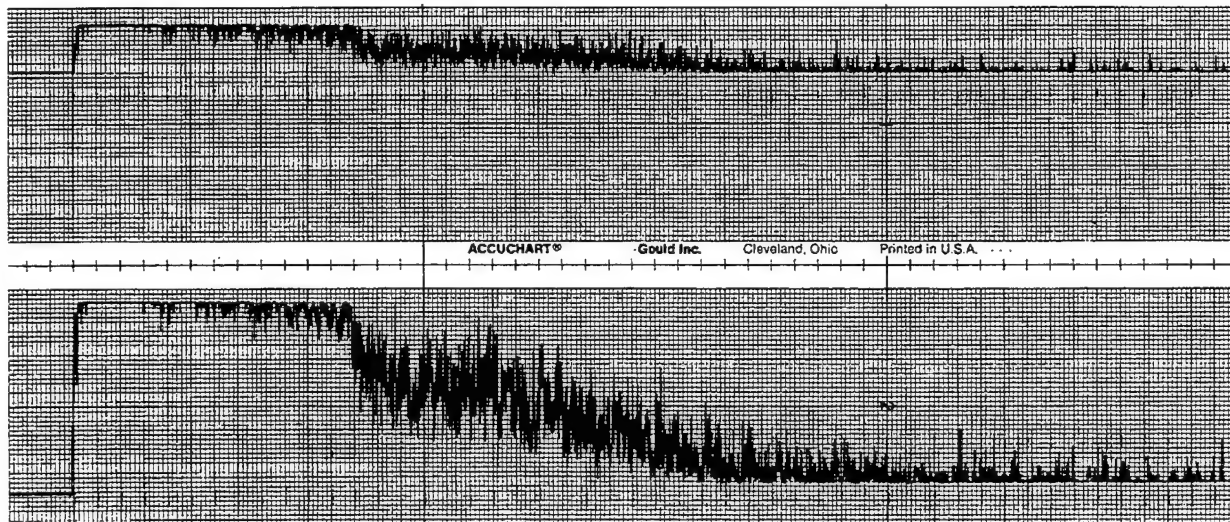


Figure 65. Sample Strip Chart Data Showing Reference and Screen Signals at 568 cm^3/s (9 gpm) After 100 Chips Were Injected

revealing a change in the screen signal while the reference signal remained constant. Monitoring the UT response ratio gave clear indications when the chips were present on the screen. The nominal discrimination signal amplitude ratio was 2:1 (**No chip** : **With chip**) for this particular test. As the chips collected on the screen, they tended to disperse the reflected UT signal; this caused a drop in signal strength from the screen and caused the ratio of the UT signal from the reference wire to the screen to increase. Most, if not all, of the injected chips did make it to the screen. The test was also conducted using various flow rates from 0 to 568 cm³/s (9 gpm); as previously demonstrated, the flow rate did not affect the results.

5.6 Prototype 2 Evaluation: Infrared Photoelectric Sensing (IR)

5.6.1 Overview

The proposed IR chip detector worked on the principle of traditional, in-line, full-flow filters. Any particles or chips in the oil that were larger than the filter opening were trapped by the filter. The size of the filter/screen opening determines the smallest size of chip that was detected. The surface of the screen on which the particles collect was continuously monitored by an infrared light source. Any chip on the surface of the screen caused a change in the transmittance of the infrared signal. This indicated the change of condition of the oil and the ceramic or metallic ball bearing.

The ultrasonic prototype was dismantled, and the infrared sensors and fiber optic cables were installed in the existing oil-flow rig setup. The infrared setup consisted of two transmitters and two receivers, in a through-transmission arrangement (Figure 66). When the infrared energy was transmitted fully, indicating a no-chip condition, the sensor response was 0 volts; for a fully blocked condition, 10 volts on each of two sensors was indicated. The infrared energy was transmitted and received through a 7.62-mm (0.30-inch) diameter fiber bundle split into two equal halves connecting the two receivers and transmitters. The fiber-optic bundles used in this experiment were capable of

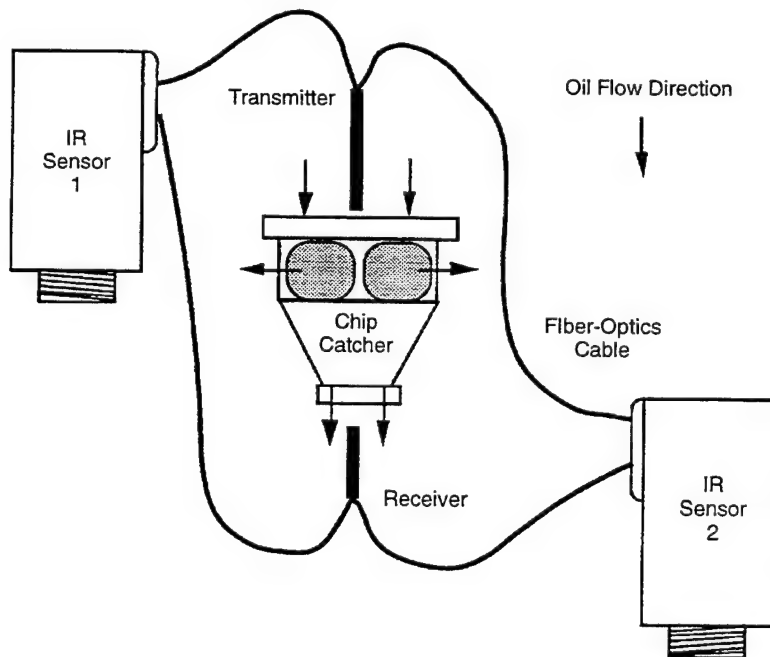


Figure 66. Schematic of IR Setup Showing Arrangement of Fiber-Optic Bundles and Location of the Chip Catcher

operation up to 260°C (500°F). Figure 67 is a drawing of the complete flow setup with the chip catcher and infrared sensors.

Alignment and calibration of the probe proved to be more difficult than originally expected. Preliminary readings from a stainless steel screen with no chips and a screen with 20 chips were collected under several conditions to establish a proper working configuration. The results indicated that the setup was capable of detecting 20 chips and more. Table 9 is a summary of the initial tests with the IR setup. Note the difference in IR probe response from the 0 to 20 chip conditions. Another condition worth noting, but not fully understood at this time, was the apparent increase in infrared energy transmittance for oil flow versus no oil flow, as seen in Table 9.

Table 9. Sample Data from IR Prototype *The results indicate that the setup is capable of detecting 20 chips and more as seen from the Δ response.*

No. of Chips	Flow, cm ³ /s	IR Probe 1 Response	IR Probe 2 Response	Total Response	Delta Response
0	0	4	7	11	--
20	379	9	9	18	7
0	0	1	1	2	--
20	379	5.0	3.5	8.5	6.5

Tests were conducted at no flow, 189 cm³/s (3 gpm), and 442 cm³/s (7 gpm) using the stainless steel screen. Results of this testing indicated that the infrared response voltage was a function of oil-flow rate and the number of chips on the screen, as shown in Figure 68. In summary, this detection method could be used to detect 10 chips and greater under no flow to 442 cm³/s (7 gpm), provided the conditions at the reading are known and compensations are made for variables such as oil-flow rate.

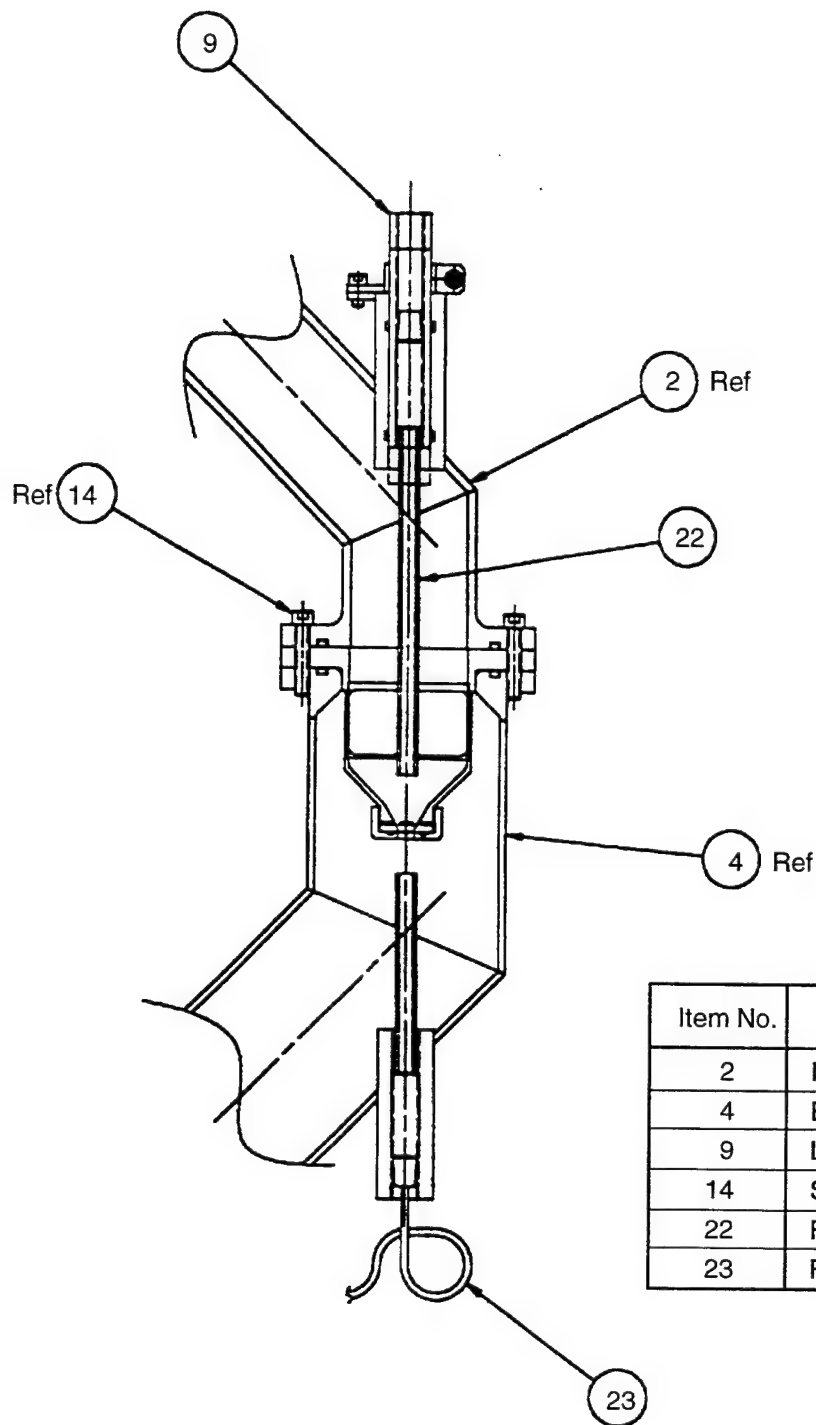
5.6.2 Experiments

5.6.2.1 Aeration Test

As with the UT device, testing to study the influence of air on the detection capability of the IR prototype was conducted. In this test, small quantities (1 to 1.5%) of air were continuously injected upstream into the oil, to study the effect on the infrared response from the collection screen. The total infrared response from the screen with no chips degraded significantly as soon as air was injected into the system. These data are summarized in Table 10.

Table 10. Results of Aeration Test with the IR Prototype
Oil temperature, 38°C; flow rate, 568 cm³/s (9 gpm).

Number of Chips	% Air	Total IR Response, V
0	0.00	8
	0.63	17
	0.90	19
	1.30	20
20	0.00	20



Item No.	Description or Name
2	Inlet Tube
4	Exit Tube
9	Light Source Sleeve
14	SOC HD Cap Screw
22	Fiber Optic Light Source
23	Fiber Optic Light Receiver

Figure 67. Drawing of the Complete Flow Setup with the Chip Collector and IR Sensors

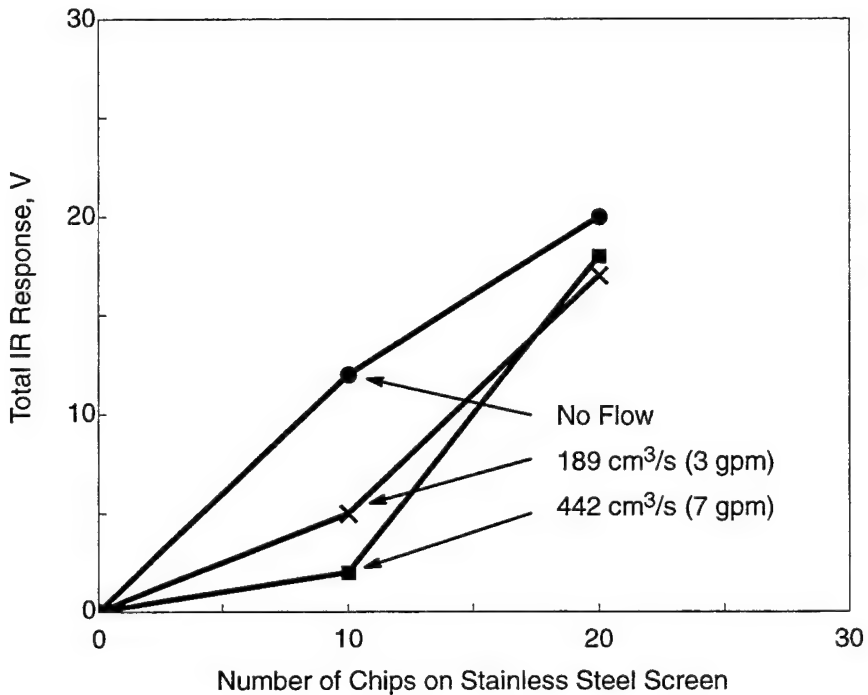


Figure 68. Detection Capabilities of the IR Prototype for Various Flow Rates and Chip Counts

It was expected that the IR device would do better than the UT device under these circumstances, but it did not. One possible explanation is that, although IR attenuation in air is much less than that of UT, the IR detector must be recalibrated to compensate for the change in attenuation due to air. This limitation cannot be compensated without making major modification to the device. Hence, the presence of air in the oil should be completely eliminated during the use of IR, if the technique is to discriminate between 0 chips with 1.3% air and 20 chips with no air. Although this is a significant limitation of the IR technique, operating conditions can be identified that result in no air present in the oil while evaluating the screen for possible ceramic and metallic debris. One such condition could be at the end of a flight with the engine shut-down and the oil settled. The inspection of the collection screen could then be performed by a ground maintenance crew and would therefore not require the addition of cabling or instruments to the cockpit. Table 10 shows the results of the aeration test with the IR prototype. Note that small amounts of air and no chips on the screen result in the same reading as a screen containing 20 chips. This highlights the difficulties in using the IR technique in real time at a condition that involves air in oil.

5.6.2.2 Temperature Effects

Figure 69 shows IR response as a function of temperature, at a constant oil flow of $568 \text{ cm}^3/\text{s}$ (9 gpm) and with 20 silicon nitride chips at the bottom of the stainless steel collection screen. This graph indicates that the IR response (voltage) was constant at oil temperatures greater than 74°C (165°F). It is important to note that this IR system was calibrated such that the zero-volts response indicated no chips on the screen and anything greater than zero indicates a blockage or interference of the infrared light passage, such as would be encountered when chips collected on the screen. Figure 70 shows that not only was the IR response constant at the higher temperature (110°C vs 38°C), it was

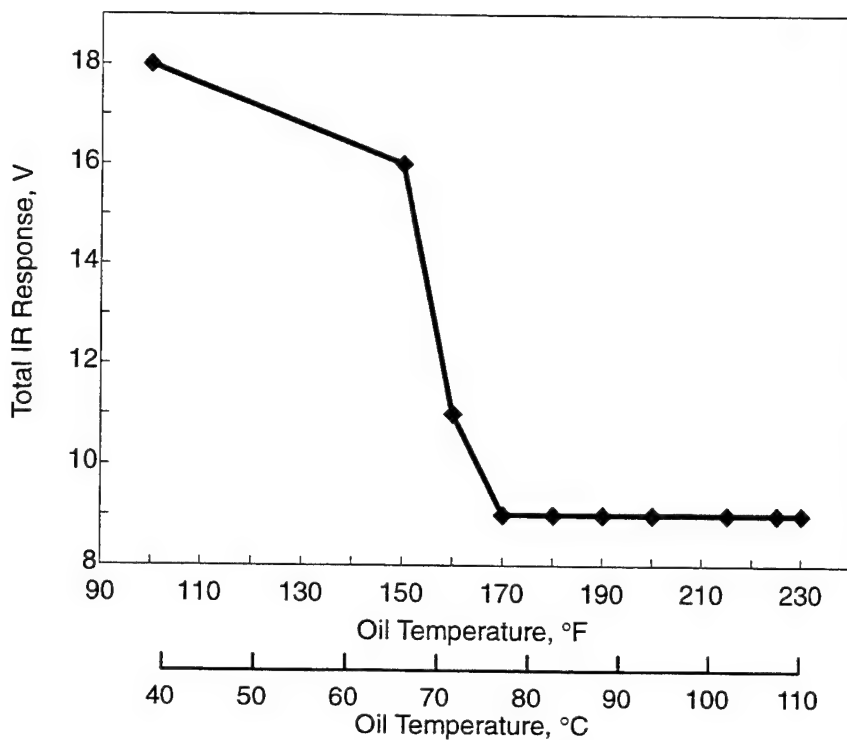


Figure 69. IR Response from 20 Chips on Stainless Steel Screen at $568 \text{ cm}^3/\text{s}$ (9 gpm) as a Function of Oil Temperature

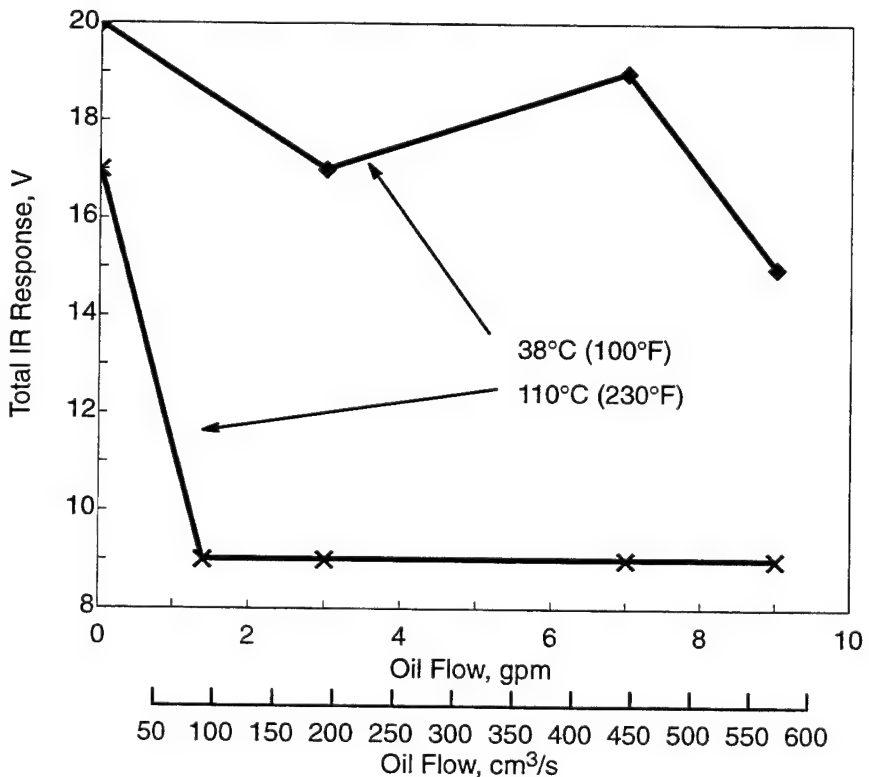


Figure 70. IR Response from 20 Chips on Stainless Steel Screen at $568 \text{ cm}^3/\text{s}$ (9 gpm) as a Function of Oil Flow and Temperature

also constant between 63 and 568 cm³/s (1 and 9 gpm) oil flow rates at the higher temperature. At the lower temperature of 38°C (100°F), the data appear quite erratic for the same range of oil flow rates. These results indicated that the IR technique may be better suited for (or limited to) use at higher temperatures. It is important to note that the ultrasonic technique, using the reference-wire-to-screen signal ratio approach, was relatively insensitive to oil flow rates and temperature variations. This heavily influenced selection of the technique for the last induced-defect test of Task 1.

5.7 Decision Analysis (Technique for Bearing Rig)

A down-selection was conducted to identify the most suitable technique for use in the test rig with the last induced-defect test from Task 1. Tables 11 and 12 show the "must" satisfy criteria and the "wants" for each of the two techniques developed, respectively. In the two tables, a "Y" means the criterion was met, and an "N" means the criterion was not met.

Table 11. "Must Have" Criteria for Prototype Testing

Must Haves	UT	IR
1. Detects 20 chips under static conditions	Y	Y
2. Detects silicon nitride chips larger than 400-μm diameter	Y	Y
3. Capable of on-line operation	Y	Y
4. Detects both metallic and nonmetallic debris	Y	Y
5. Effective in new or used oil	Y	Y
6. Effective in oil flow without entrained air	Y	Y

Table 12. "Wants" for Prototype Testing

Wants	UT	IR
1. Effective in oil flow with entrained air	N	N
2. Can be system-checked for operational capability	Y	N
3. Discriminates trapped air bubbles	N	N
4. Functional under full oil-flow rates — 568 cm ³ /s (9 gpm)	Y	Y
5. Insensitive to temperature changes	*	**
6. Works in real time (under real conditions, with entrained air)	N	N
7. Employs currently available technology	Y	Y
8. Employs low-cost technology	Y	Y
9. Offers good reliability	High	Medium
10. Generates indication after 10 chips	Y	Y
11. Works with a full-flow, debris-collection device	Y	Y
12. Calibration and setup are easy and repeatable	Y	N
13. Insensitive to coking	Y	N

* The ratio of screen signal/reference signal is constant

** IR response is constant after 73.8°C (165°F).

From Table 11, it can be seen that both techniques pass the “must satisfy” criteria. This implies that we are able to carry one of the techniques forward to the full-scale bearing test. From Table 12, it is observed that the IR technique is more sensitive to temperature changes and does not allow an operational-capability check before readings are made; whereas, the UT ratio technique is insensitive to temperature changes and does allow for a system check using the reference wire. Based on a balance of “musts” and “wants” criteria and knowing that a operating scavenge line will likely contains large amounts of air (dry sump requirement), our decision was to use the UT technique under static conditions. This decision agrees well with a concern raised by GEAE military products personnel regarding the additional equipment and wiring needed if a real-time, continuous, condition-monitoring device was proposed. However, the proposed device can be used by ground maintenance crew to perform a static test and determine the presence of either metallic or ceramic bearing chips with minimal modifications and weight addition.

It is apparent from Table 12 that the UT technique satisfies more “want” criteria, and it was therefore the technique used during the last full-scale rig test.

5.8 Fourth Induced-Defect Bearing Test/Prototype Demonstration

5.8.1 Preliminary Results

The UT chip detector, evaluated in the bench setup, was selected as the most suitable condition-monitoring device for demonstration during the fourth hybrid bearing induced-defect test. The device was moved from the bench setup to the bearing test rig and installed downstream from the bearing sump and electronic chip detectors. The UT condition-monitoring device was set-up such that the presence of chips could be detected after the completion of a simulated mission cycle and when the test rig was shutdown. This condition would simulate a ground maintenance crew performing an inspection of the UT condition-monitoring device. The results of the fourth induced-defect test are summarized in Table 13.

The UT condition-monitoring device was set-up and examined after each of the first three cycles, as shown in Table 13. Readings from the reference wire and the screen were taken before and after each test run, and the difference in the ratio was used to determine the probable presence of chips in the collector. A large positive (+) difference was considered an indication of chips on the collection screen, but a small positive (+) or negative (-) difference was not considered an indication of chips (more likely caused by variations in the UT response caused by inspection temperature variations). The UT chip collector was disassembled and examined after the first cycle. The bottom of the flat screen was covered with coke. It is important to note that this did not affect the screen/wire ratio, indicating that coke is not a good reflector and therefore has minimal impact on the UT signal. The coke product surely would have affected the IR chip detection technique, resulting in a false alarm. This further supports the decision to use the UT device during this rig demonstration.

During inspection of the UT device, we found it important to allow the oil and transducer to cool to room temperature before taking readings. (In the initial several rounds of testing, hot oil (+38°C) resulted in some data scatter.)

After the second cycle of testing was completed and the UT condition-monitoring device was disassembled, we found a single metal flake on the bottom of the screen and one metal flake on the ECD. Neither was sufficient to trigger an alarm. No additional chips were detected by either device or found after the third cycle.

Table 13. Summary of Results from Fourth Induced-Defect Test

Cycle	Reference Voltage	Screen Voltage	Ratio	Δ Ratio	Comments
1	1.7	5.7	3.35		With hot oil
1	2.7	8.1	3.00	0.35	Oil cooled overnight; data collected 9 a.m. Bottom of screen covered with coking; no effect on ratio
2	2.7	6.7	2.48		Cleaned and rebuilt; reading with cold oil.
2	2.0	5.0	2.50	-0.02	Reading with hot oil. One metal flake visible; ECD did not trip.
3	1.8	5.0	2.78		Cleaned and rebuilt; reading with hot oil.
3	2.2	9.9	4.50	-1.72	Oil cooled for 1 hr, 30 min before inspection. No chips found.
4	2.5	6.9	2.76		Cleaned and rebuilt; reading with cold oil.
8	2.3	9.8	4.26	-1.50	Oil cooled for 2 hr before inspection. No chips found.
9	2.5	6.6	2.64		Cleaned and rebuilt; reading with cold oil.
30	2.5	1.9	0.76	1.88	Oil cooled for 2 hr before inspection. Found lots of metallic chips, coked oil.
31	2.5	5.0	2.00		Cleaned and rebuilt; reading with cold oil. UT probe failed, possible because of over-temperature. Data collected with conventional low-temperature probe.

At this point, it was decided to go automatic — allowing the ECD to automatically shut the rig down. Five cycles later (or after a total of eight cycles), the ECD automatically shut the rig down. Metal chips on the ECD were confirmed to be the cause of the shutdown. Inspection of the screen using the UT device failed to indicate the probability of any chips on its screen. Upon disassembly and inspection, it was confirmed that no chips had made it to the screen.

Next, the ECD's were removed from the oil flowpath to allow the chips to make it downstream to the UT device. The rig was run through another 22 cycles, and the UT device was inspected. This time the ratio of UT response from the screen to the wire had shifted significantly, indicating chips were likely on the screen. Upon disassembly of the UT device, numerous metallic chips were found. The rig subsequently went through another 111 cycles, after the chips were detected using the UT device, before the bearing failed. Thus the technique had demonstrated its feasibility as an early warning system; there were 55 hours or 111 cycles between early warning and actual failure.

The temperature of the oil at the bearing was 177°C (350°F) and was estimated to be 163°C (325°F) when it entered the ultrasonic chip detector, but the UT probe was designed to withstand 107° to 121°C (225° to 250°F) only. The result of exposing the probe to this kind of high temperature for an extended time (+20 hours) resulted in probe failure. This can be overcome by specifying a higher temperature probe.

5.8.2 Final Results

Although the test bearing ran for 143 cycles before it completely failed, the UT condition-monitoring equipment could not be used to collect additional data during the latter part of the test because it failed during operation. One of the internal solder joints came lose due to the high rig temperatures during the latter part of the testing; temperatures as high as 232°C (450°F) were recorded for the sump oil. The condition-monitoring device was designed to operate between 121° to 148°C (250° to 300°F), which is in the normal operating range for the bearing. The bearing test rig was dismantled, and the chip collector was examined visually (Figures 71 and 72). A large amount of chips had been collected; most appear to be M50 metallic chips, but a few are possibly ceramic chips.

Task 3 showed that metallic and ceramic chips could be detected by the ultrasonic approach, and it could be used as an early warning against catastrophic failure.

5.9 Other Bearing Condition-Monitoring Devices Evaluated

5.9.1 Philtec (Fiber-Optic Bearing Monitor)

The deflectometer used in the trial run of the hybrid bearing for Task 1 was an instrument made by Philtec. This device uses a fiber-optic system to measure relative radial deflection between the outer ring and the bearing housing. This deflection warns of bearing degradation. Our first test of this device was during a break-in run in which a bearing without any defects underwent the automatic 30-minute cycle. During this test, it was discovered that the full range of deflection was used-up just by the variation in load and speed on the bearing. It was thus determined that this particular monitor would likely not survive a test in which a defect was present in the outer race, so no further testing was performed with this device.

5.9.2 SKF Device

An SKF condition-monitoring device was available to monitor the progress of the fourth induced-defect test. The technique works on the premise that, as a bearing fails, the components emit specific harmonic frequencies associated with the degradation of an inner race, outer race, cage, or rolling element. The SKF technique used what they call SEE (spectral emitted energy) enveloping. The technique essentially amplified repetitive harmonic frequencies and suppressed background random noise. At the onset of the final induced-defect test, the SKF device easily detected a frequency correlated to the outer-race EDM-notch defect. In addition to the outer-race defect, the SKF device was able to detect high levels of ball spin and cage defect spectral components in several of the latter displays, which were considered signs of impending bearing failure. Although the probability of detecting rolling-element defects was low, due to the randomness of rolling over a ball defect, spectra were recorded that did reveal a rolling-element defect. This correlated well with the five silicon nitride balls that contained small spalls at the conclusion of this test. The SKF Condition Monitoring report is replicated in Appendix F.

5.10 Task 3 Conclusions

- UT and IR techniques can both detect magnetic and nonmagnetic bearing debris.
- Entrained air limits both techniques.
- The UT technique, being insensitive to temperature and allowing a real-time system check, was selected for rig demonstration.

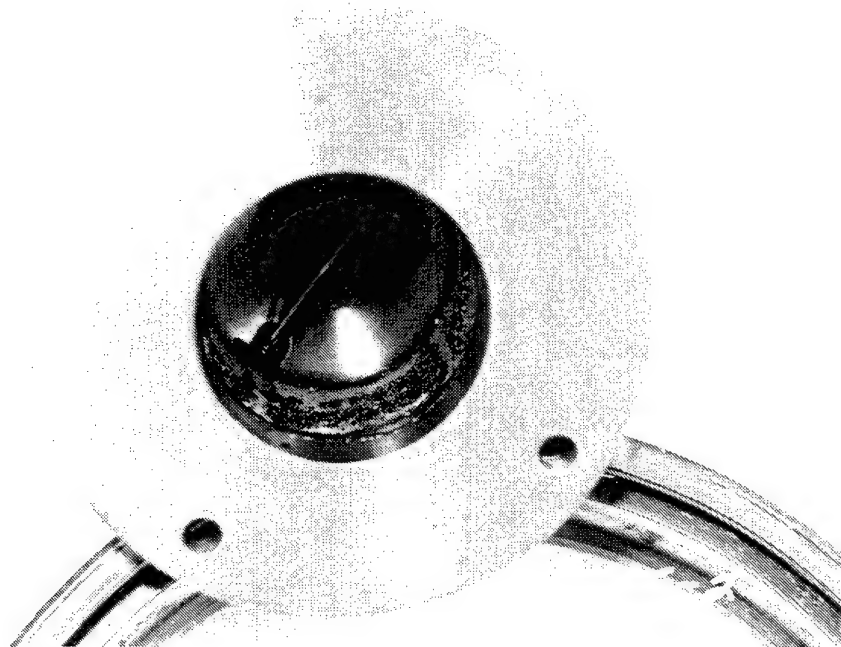


Figure 71. Induced-Defect Chips on Chip Collector

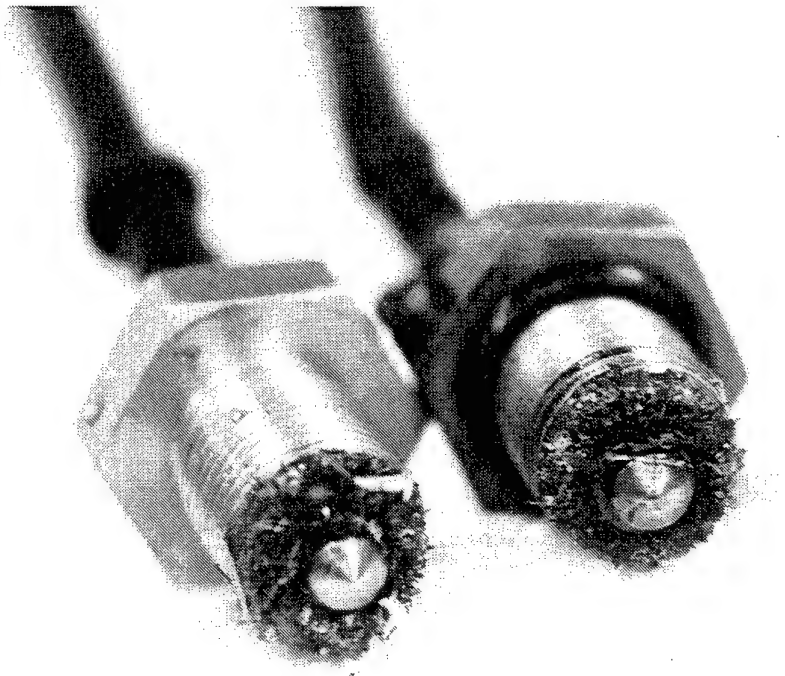


Figure 72. Induced-Defect Chips on Magnetic Plugs

- The UT device detected debris in the full-flow chip collector at least 113 cycles before the bearing failed.
- The SKF condition-monitoring device easily detected and pinpointed the outer-ring defect and also detected cage and rolling-element defects.

5.11 Recommendations for Future Work

Several modifications can be made to improve the performance and to adapt the two prototype devices built and tested in this program. The following are suggestions for improvement and future research:

- Improve the design and construction of the ultrasonic probe so that it performs at higher temperatures, up to 232°C (450°F).
- Multiple ultrasonic probes could be used to cover a larger area, up to 0.75-cm (0.3-in) diameter, and could be shaped to conform to the desired envelope. This would make the filter cross section smaller.

Multiple ultrasonic reception modes (pulse-echo and through-transmission) could be used both independently and simultaneously to provide better discrimination of particles on the screen.

The IR technique lacked a convenient method to verify if the conditions were proper to take data. This can be achieved by adding additional infrared sensors perpendicular to the flow, such that any change in flow characteristics could be used to compensate the received signals.

Further improvements could be made by combining the ultrasonic and infrared devices so that they work simultaneously to provide more reliable data.

The SKF device should be evaluated on a bearing without any known defects, undergoing endurance testing, for ability to detect and pinpoint the onset of impending bearing failure.

6.0 Overall Program Conclusions

6.1 Task 1

- Silicon nitride balls are capable of withstanding the high shock loads encountered during race spalling,
- The hybrid bearing operates for a reasonable length of time after race spall initiation, comparable to that provided by an all-steel bearing,
- Silicon nitride balls exhibit no more distress than AISI M50 tool steel balls,
- The spalls from the silicon nitride balls are made up of numerous smaller spalls, and the size of the chips coming off are reasonably large enough to be caught in a 400- μm size screen for detection.
- The amount of metallic debris liberated by the hybrid bearing may be significantly larger than is released by an all-steel bearing, increasing the probability of detecting an impending failure.

6.2 Task 2

- At normal engine operating conditions, hybrid bearings offer little, if any, improvement in thermal performance over an all-steel bearing.
- Hybrid bearings with tightened race curvatures operate at higher temperatures than either the open-curvature hybrid bearing or the all-steel bearing.
- Hybrid bearings offer the benefit of being capable of sustained operation at reduced oil flow.

6.3 Task 3

- UT and IR Techniques can both detect magnetic and nonmagnetic bearing debris.
- Entrained air limits both techniques.
- The UT technique, being insensitive to temperature and allowing a real-time system check, was selected for rig demonstration.
- The UT device detected debris in the full-flow chip collector at least 113 cycles before the bearing failed.
- The SKF condition-monitoring device easily detected and pinpointed the outer-ring induced defect and also detected cage and rolling-element defects.

7.0 References

1. Rhoads, M., "Engine Hybrid Ceramic Bearings, Final Report Supplement: Selected Color Photos," R94AEB276 Supplement, April 1996.
2. Zaretsky, E.V., "Ceramic Bearings for Use in Gas Turbine Engines," ASME Journal of Engineering for Gas Turbines and Power, Vol. 111, No. 1, pp 146–157, 1989.
3. Parker, R.J. and Zaretsky, E.V., "Fatigue Life of High-Speed Ball Bearings with Silicon Nitride Balls," Journal of Lubrication Technology, Trans. ASME, Series F, Vol. 97, No. 3, July 1975.
4. Wheildon, W.M., Baumgartner, H.R., Sundberg, D.V., and Torti, M.K., "Ceramic Materials in Rolling Contact Bearings," Final Technical Report under Naval Air Systems Command Contract N,00019–72–C0299, 1973.
5. Valori, R., "Rolling Contact Fatigue of Silicon Nitride," Naval Air Propulsion Test Center Report NAPTC-PE-42, August 1974.
6. Reddecliff, J.M. and Valori, R., "The Performance of a High-Speed Ball Thrust Bearing Using Silicon Nitride Balls," Journal of Lubrication Technology, Transactions of the ASME, pp 553 – 563, October 1976.
7. Weinberg, P. and Bersch, C.F., "Ceramics in Rolling Bearings," ASME, 79-GT-68, Gas Turbine Conference and Exhibit & Solar Energy Conference, San Diego, California, March 12–15, 1979.
8. Ebert, F.J., "Performance of Silicon Nitride Components in Aerospace Bearing Applications," ASME, 90-GT-166, Gas Turbine and Aeroengine Congress and Exposition, June 11 –14, 1990, Brussels, Belgium.
9. Nishihara, Y., Nakashima, H., Tsushima, N., and Ito, S., "Factors That Affect Rolling Contact Fatigue Life of Ceramics and Rolling Contact Fatigue Life of Ceramic Balls and Rollers," ASME, 90-GT-377, Gas Turbine and Aeroengine Congress and Exposition, June 11 – 14, 1990, Brussels, Belgium.
10. *Guide to Engine Oil System Monitoring*, SAE, The Engineering Society for Advancing Mobility Land, Sea, Air, and Space, AIR1828, January 22, 1992.

Appendix A

Task 2 High-Speed Test Data

This appendix presents detailed test data in Tables 14 through 21. These data are discussed in section 4 of this report.

In some column headings, “OR” signifies *outer race*, and “ORC” indicates *outer race cooling* (oil flow).

Table 14. Thermal, Cage Speed, and Power Data for All-Steel Bearing (P04)

Test Point	Load, lbf	Speed, rpm	Oil-In Temp, °F	Lube Flow, gpm	Outer Race Cooling, gpm	Outer Race Load-End Temp, °F	Outer Race Drive-End Temp, °F	Inner Race Temp, °F	Cage Speed Ratio	Power Draw, kW
1	1,000	12,500	250	2	0	285	283	281	0.4417	12.4
2	1,000	12,500	250	1.5	0	289	286	277	0.4397	11.7
3	1,000	12,500	250	1	0	295	288	286	0.439	10.5
4	5,000	12,500	250	2	0	301	297	280	0.4469	17
5	5,000	12,500	250	1.5	0	313	307	299	0.4496	15.3
6	5,000	12,500	250	1	0	326	316	291	0.449	14.5
7	1,000	18,750	250	2	0	318	315	306	0.4347	23.7
8	1,000	18,750	250	1.5	0	325	320	325	0.4405	20.1
9	1,000	18,750	250	1	0	334	329	320	0.4376	18.2
10	5,000	18,750	250	2	0	350	345	332	0.4562	30.3
11	5,000	18,750	250	1.5	0	366	356	332	0.455	26.2
12	5,000	18,750	250	1	0	365	358	331	0.454	22.4
13	1,000	25,000	250	2	0	364	362	352	0.4307	38.3
14	1,000	25,000	250	1.5	0	375	370	352	0.4344	32.5
15	1,000	25,000	250	1	0	385	379	360	0.4351	30.5
16	5,000	25,000	250	2	0	406	400	376	0.456	47.7
17	5,000	25,000	250	1.5	0	402	401	358	0.4559	38.9
18	5,000	25,000	250	1	0	417	415	367	0.4567	35.5
19	1,000	12,500	150	2	0	195	192	203	0.4407	14.5
20	1,000	12,500	150	1.5	0	204	201	200	0.4417	13.4
21	1,000	12,500	150	1	0	211	207	200	0.4414	11.5
22	5,000	12,500	150	2	0	220	216	205	0.4482	19.7
23	5,000	12,500	150	1.5	0	232	227	209	0.4453	18.2
24	5,000	12,500	150	1	0	248	235	205	0.4469	16.5
25	1,000	18,750	150	2	0	236	233	220	0.4373	26.5
26	1,000	18,750	150	1.5	0	246	242	219	0.4375	22.8
27	1,000	18,750	150	1	0	258	254	205	0.4378	20.7
28	5,000	18,750	150	2	0	274	270	239	0.4562	35
29	5,000	18,750	150	1.5	0	277	272	230	0.4533	29
30	5,000	18,750	150	1	0	297	290	238	0.4545	25.4
31	1,000	25,000	150	2	0	281	281	264	0.4334	41.4
32	1,000	25,000	150	1.5	0	295	291	277	0.4356	36.4
33	1,000	25,000	150	1	0	311	306	264	0.4364	32.8
34	5,000	25,000	150	2	0	329	315	282	0.4555	51.8
35	5,000	25,000	150	1.5	0	332	329	284	0.4544	44
36	5,000	25,000	150	1	0	348	344	274	0.4558	38.8

Table 15. Thermal, Cage Speed, and Power Data for Hybrid Bearing (P05)

Test Point	Load, lbf	Speed, rpm	Oil-In Temp, °F	Lube Flow, gpm	Outer Race Cooling, gpm	Outer Race Load-End Temp, °F	Outer Race Drive-End Temp, °F	Inner Race Temp, °F	Cage Speed Ratio	Power Draw, kW
37	1,000	12,500	250	2	0	280	279	281	0.4445	13.2
38	1,000	12,500	250	1.5	0	287	286	284	0.4455	11.9
39	1,000	12,500	250	1	0	295	287	285	0.4467	10.3
40	5,000	12,500	250	2	0	290	290	284	0.4416	16
41	5,000	12,500	250	1.5	0	299	298	284	0.4414	14.5
42	5,000	12,500	250	1	0	317	313	292	0.4432	13.7
43	1,000	18,750	250	2	0	319	319	313	0.4435	25.5
44	1,000	18,750	250	1.5	0	324	318	317	0.447	21
45	1,000	18,750	250	1	0	331	329	321	0.4518	18.1
46	5,000	18,750	250	2	0	339	341	318	0.447	31.1
47	5,000	18,750	250	1.5	0	352	351	329	0.4449	27.6
48	5,000	18,750	250	1	0	373	355	339	0.4509	23.3
49	1,000	25,000	250	2	0	360	357	343	0.4393	40
50	1,000	25,000	250	1.5	0	363	364	344	0.4463	34.5
51	1,000	25,000	250	1	0	379	378	362	0.4516	28.6
52	5,000	25,000	250	2	0	397	399	367	0.4517	49.9
53	5,000	25,000	250	1.5	0	412	389	382	0.4543	41.4
54	5,000	25,000	250	1	0	410	405	378	0.4552	33.2
55	1,000	12,500	150	2	0	193	192	200	0.4461	15.1
56	1,000	12,500	150	1.5	0	201	198	200	0.4466	13.3
57	1,000	12,500	150	1	0	210	208	no data	0.4476	11.6
58	5,000	12,500	150	2	0	197	196	no data	0.4388	15.9
59	5,000	12,500	150	1.5	0	204	203	no data	0.4379	13.9
60	5,000	12,500	150	1	0	221	218	202	0.4396	12.8
61	1,000	18,750	150	2	0	234	234	217	0.4483	26.7
62	1,000	18,750	150	1.5	0	237	239	213	0.4449	22.6
63	1,000	18,750	150	1	0	252	255	210	0.4511	19.5
64	5,000	18,750	150	2	0	263	266	223	0.4442	34.4
65	5,000	18,750	150	1.5	0	266	267	223	0.4442	28
66	5,000	18,750	150	1	0	290	290	239	0.4474	25.1
67	1,000	25,000	150	2	0	278	276	259	0.4453	41.7
68	1,000	25,000	150	1.5	0	287	285	264	0.4475	36
69	1,000	25,000	150	1	0	308	305	274	0.4488	31.2
70	5,000	25,000	150	2	0	321	314	275	0.4496	52.8
71	5,000	25,000	150	1.5	0	323	319	274	0.4507	44.1
72	5,000	25,000	150	1	0	344	341	344	0.4532	36.5

Table 16. Thermal, Cage Speed, and Power Data for Tight Hybrid Bearing (P06)

Test Point	Load, lbf	Speed, rpm	Oil-In Temp, °F	Lube Flow, gpm	Outer Race Cooling, gpm	Outer Race Load-End Temp, °F	Outer Race Drive-End Temp, °F	Inner Race Temp, °F	Cage Speed Ratio	Power Draw, kW
73	1,000	12,500	250	2	0	284	281	283	0.4474	13.9
74	1,000	12,500	250	1	0	298	294	284	0.4501	11.4
75	5,000	12,500	250	1.5	0	306	307	284	0.4456	15.8
76	1,000	18,750	250	1.5	0	333	332	323	0.4534	23.3
77	5,000	18,750	250	2	0	345	346	325	0.4521	33.4
78	5,000	18,750	250	1	0	388	388	334	0.4584	26.7
79	1,000	25,000	250	2	0	370	373	356	0.4474	43.6
80	1,000	25,000	250	1	0	390	386	363	0.4599	31.3
81	5,000	25,000	250	1.5	0	428	431	386	0.4634	47.8
82	1,000	12,500	150	1.5	0	206	202	204	0.4467	13.9
83	5,000	12,500	150	2	0	212	214	201	0.4397	18.9
84	5,000	12,500	150	1	0	239	239	204	0.4415	15.7
85	1,000	18,750	150	2	0	236	235	225	0.4476	28.1
86	1,000	18,750	150	1	0	263	260	243	0.4531	21.9
87	5,000	18,750	150	1.5	0	279	282	234	0.4507	30.5
88	1,000	25,000	150	1.5	0	297	294	273	0.4524	38.4
89	5,000	25,000	150	2	0	331	336	280	0.4563	57.6
90	5,000	25,000	150	1	0	355	353	282	0.4603	39.5

Table 17. Thermal, Cage Speed, and Power Data for All-Steel and Hybrid Bearings (P04 and P05)

Test Point	Load, lbf	Speed, rpm	Oil-In Temp, °F	Lube Flow, gpm	Outer Race Cooling, gpm	Outer Race Temp, °F	P04 Outer Race Temp, °F	P05 Outer Race Temp, °F
91	1,000	18,750	250	0.5	0.5	324	327	
92	1,000	18,750	250	0.25	0.5	343	343	
93	1,000	18,750	250	0.5	0	360	366	
94	5,000	18,750	250	0.5	0.5	354	359	
95	5,000	18,750	250	0.25	0.5	380	382	
96	5,000	18,750	250	0.5	0	399	405	
97	1,000	25,000	250	0.5	0.5	362	374	
98	1,000	25,000	250	0.25	0.5	382	392	
99	1,000	25,000	250	0.5	0	403	420	
100	5,000	25,000	250	0.5	0.5	395	407	
101	5,000	25,000	250	0.25	0.5	400	447	

Table 18. Test Data for All-Steel Bearing (P04)

Test Point	Run Time, Hours	Shaft Speed, rpm	Cage Speed Ratio	Thrust Load, lbf	Vibration, G's	Lube Flow, gpm	Power Draw, kW	Temperature, °F				Inner Race
								Oil In	OR	Sleeve	End Casing	
1	1.23	12,542	0.4417	1,015	7.0	1.98	12.4	251.6	283.4	283.8	282.5	284.9
2	17.87	12,519	0.4397	1,018	7.0	1.49	11.7	238.2	286.4	284.6	277.1	287.1
3	3.41	12,497	0.4390	1,008	7.3	0.99	10.5	249.1	288.4	289.4	286.5	295.1
4	18.31	12,502	0.4469	5,020	8.2	2.00	17.0	249.3	296.8	297.5	287.8	300.9
5	6.44	12,510	0.4496	5,009	9.2	1.51	15.3	251.2	306.6	308.6	303.2	313.0
6	18.63	12,518	0.4490	5,014	9.3	0.98	14.5	249.6	316.3	318.6	312.7	305.2
7	18.95	18,723	0.4347	1,017	13.5	2.01	23.7	248.2	315.5	315.6	312.8	299.9
8	10.70	18,767	0.4405	1,010	13.8	1.51	20.1	247.4	320.4	321.1	312.8	305.5
9	19.39	18,779	0.4376	1,018	12.9	0.99	18.2	248.5	329.3	330.7	326.8	315.1
10	2.69	18,754	0.4562	5,007	23.2	1.98	30.3	249.6	344.7	345.5	341.2	323.5
11	20.26	18,729	0.4550	5,014	24.9	1.50	26.2	250.5	355.6	358.6	351.1	335.3
12	4.17	18,763	0.4540	4,993	26.5	1.02	22.4	250.3	357.5	360.9	353.3	341.7
13	7.22	25,036	0.4307	1,003	21.2	2.00	38.3	249.4	362.2	361.4	358.0	337.8
14	20.73	25,026	0.4344	1,019	22.9	1.49	32.5	250.5	370.4	370.7	365.3	347.3
15	3.59	25,013	0.4351	1,016	24.2	0.99	30.5	249.4	378.8	378.8	373.8	355.5
16	21.06	24,983	0.4560	5,024	53.6	1.99	47.7	250.4	400.4	400.4	393.4	365.2
17	8.21	25,029	0.4559	5,012	57.0	1.50	38.9	249.8	401.2	402.1	393.5	370.3
18	21.38	25,027	0.4567	5,005	60.0	1.01	35.5	250.2	415.2	416.4	407.3	386.5
19	1.98	12,492	0.4407	1,007	8.7	1.98	14.5	148.5	191.9	191.5	189.5	182.2
20	5.17	12,505	0.4417	1,003	8.6	1.51	15.4	150.5	200.6	201.0	198.4	189.5
21	2.47	12,517	0.4414	1,015	9.2	1.01	11.5	149.9	207.3	207.1	204.5	196.5
22	11.36	12,476	0.4482	5,010	8.0	1.99	19.7	151.3	215.5	216.2	204.2	210.7
23	5.83	12,497	0.4453	4,994	9.4	1.51	18.2	150.5	226.5	228.3	222.7	211.7
24	23.04	12,481	0.4469	5,016	9.8	1.01	16.5	148.0	235.0	236.8	231.1	223.6
25	23.88	18,751	0.4373	1,004	11.4	2.01	26.5	149.7	232.8	232.8	229.7	214.4
26	17.09	18,746	0.4375	1,012	11.6	1.50	22.8	150.3	242.1	242.2	238.7	222.9
27	24.67	18,794	0.4378	1,011	12.3	0.99	20.7	150.9	254.2	254.3	250.6	235.8
28	13.96	18,733	0.4562	5,002	24.7	1.99	35.0	150.4	270.2	269.6	264.3	244.7
29	0.22	18,710	0.4533	5,019	24.1	1.51	29.0	148.9	272.3	273.5	266.2	249.3
30	17.51	18,743	0.4545	5,008	23.8	1.00	25.4	150.0	290.4	291.2	283.9	270.0
31	15.83	25,027	0.4334	1,016	23.5	1.99	41.4	149.2	280.6	277.9	274.2	252.9
32	14.67	25,021	0.4356	1,016	23.6	1.49	36.4	147.9	290.7	289.2	262.2	295.3
33	16.17	25,001	0.4364	1,015	25.6	0.99	32.8	148.9	306.3	304.2	299.3	310.7
34	1.32	25,016	0.4555	1,017	54.8	2.00	51.8	150.9	315.1	315.5	307.3	328.6
35	15.50	24,986	0.4544	4,998	57.4	1.51	44.0	149.8	329.4	328.3	320.6	314.7
36	15.16	25,022	0.4558	1,016	59.5	1.01	38.8	148.5	343.6	344.0	332.1	341.1

Table 19. Test Data for Hybrid Bearing (P05)

Test Point	Run Time, Hours	Shaft Speed, rpm	Cage Speed Ratio	Thrust Load, lbf	Vibration, G's	Lube Flow, gpm	Power Draw, kW	Temperature, °F						Inner Race			
								Oil In	OR	Drive Sleeve	End Casing	Drain	OR				
37	31.11	12,508	0.4445	1,015	4.7	1.99	13.2	249.2	279.6	278.1	272.7	280.3	281.0	279.2	275.1	281	
38	31.68	12,511	0.4455	1,012	5.0	1.50	11.9	250.5	285.8	283.6	277.4	286.6	288.1	285.4	278.3	284	
39	31.93	12,509	0.4467	1,015	5.1	1.00	10.3	249.5	287.4	288.8	285.3	281.9	294.8	296.1	293.4	279.7	285
40	32.66	12,501	0.4416	5,013	4.1	2.00	16.0	247.7	290.5	288.5	281.8	290.3	291.5	288.6	283.6	284	
41	1.71	12,472	0.4414	5,005	3.9	1.49	14.5	248.5	298.5	294.6	286.8	299.3	300.8	296.6	288.9	284	
42	19.30	12,484	0.4432	5,014	4.4	1.00	13.7	251.6	313.0	314.4	308.8	302.0	317.4	318.8	313.9	300.2	292
43	19.95	18,744	0.4435	1,016	9.5	1.99	25.5	249.9	319.7	319.0	316.8	304.3	319.3	319.6	316.9	308.5	313
44	15.20	18,744	0.4470	1,017	10.1	1.49	21.0	250.5	318.4	319.7	315.7	306.3	324.8	325.8	321.7	309.6	317
45	33.14	18,749	0.4518	1,018	10.6	1.00	18.1	250.2	329.2	330.6	326.3	317.0	331.8	333.6	328.3	309.6	317
46	3.49	18,731	0.4470	5,012	12.2	2.00	31.1	249.8	341.2	336.2	321.8	339.1	341.4	335.4	326.9	318	
47	21.13	18,762	0.4490	5,004	12.6	1.49	27.6	251.7	355.1	356.0	349.8	333.9	354.6	356.2	349.2	336.3	329
48	4.05	18,763	0.4509	5,010	14.0	0.99	23.3	249.1	357.0	359.9	352.2	346.2	375.4	377.9	370.2	343.4	339
49	33.56	24,984	0.4393	1,019	20.9	2.00	40.0	249.3	357.3	356.9	352.6	336.4	360.5	361.0	358.3	342.5	343
50	34.00	25,033	0.4463	1,016	21.3	1.50	34.5	248.7	363.8	362.8	358.7	340.8	362.7	362.9	359.4	346.6	344
51	34.69	24,991	0.4516	1,015	19.7	1.0	28.6	252.3	377.5	378.8	372.8	358.0	379.6	381.8	375.8	352.0	362
52	22.15	24,994	0.4517	5,002	27.7	1.99	49.9	251.1	399.2	398.2	391.5	368.6	397.5	400.0	392.7	374.1	367
53	35.30	25,006	0.4543	5,002	27.7	1.50	41.4	248.3	388.8	391.8	382.7	367.0	411.8	412.8	405.5	378.5	382
54	35.73	25,010	0.4552	5,000	28.1	0.99	33.2	248.4	405.9	408.8	399.2	385.1	410.3	414.0	403.3	381.1	378
55	28.62	12,492	0.4461	1,012	4.2	1.99	15.1	150.3	191.9	192.5	189.7	183.9	193.6	194.4	185.1	180.0	180
56	29.27	12,514	0.4466	1,012	4.7	1.49	13.3	150.5	197.9	199.3	195.7	188.8	201.3	202.7	199.2	189.2	200
57	24.09	12,523	0.4476	1,007	5.2	1.00	11.6	152.6	207.9	208.2	205.2	198.8	209.8	209.9	206.2	194.1	0
58	8.92	12,489	0.4388	4,996	3.6	2.00	15.9	148.5	196.4	196.6	193.5	187.0	196.8	197.6	194.1	187.5	0
59	24.60	12,489	0.4379	5,005	3.6	1.50	13.9	152.1	203.4	203.3	200.2	193.1	204.4	205.6	200.9	193.5	0
60	9.32	12,517	0.4396	5,015	3.7	1.00	12.8	151.0	217.6	218.0	213.8	207.2	221.3	222.8	217.6	203.3	202
61	10.00	18,766	0.4483	1,017	11.7	2.00	26.7	151.0	234.3	233.8	230.4	217.4	233.7	234.9	231.4	219.0	217
62	25.21	18,781	0.4490	1,014	12.6	1.49	22.6	150.7	238.8	238.6	234.4	220.8	236.8	239.0	233.8	220.2	213
63	10.42	18,763	0.4511	1,015	14.0	1.00	19.5	151.6	255.1	255.3	250.5	238.4	252.5	254.3	249.2	228.9	210
64	25.79	18,738	0.4442	4,999	10.7	2.00	34.4	151.4	265.6	264.8	259.7	242.3	263.3	263.9	258.0	244.9	223
65	10.77	18,766	0.4442	4,996	11.6	1.50	28.0	150.9	266.9	267.6	260.1	246.6	265.7	267.5	259.4	247.1	223
66	26.42	18,744	0.4474	5,010	11.8	1.00	25.1	151.0	289.8	292.0	282.9	270.5	290.3	292.6	283.1	264.6	239
67	29.70	25,000	0.4453	1,012	22.4	2.00	41.7	152.5	276.0	275.4	271.1	253.3	278.2	277.7	274.2	256.8	259
68	11.70	24,977	0.4475	1,013	22.9	1.50	36.0	150.6	284.7	282.9	278.1	260.3	286.7	286.5	281.5	263.6	264
69	30.40	25,029	0.4488	1,011	24.2	1.00	31.2	151.0	305.2	304.8	299.5	283.9	308.6	309.5	303.6	278.2	274
70	12.45	25,029	0.4496	5,017	29.0	2.01	52.8	150.3	313.2	305.3	284.2	321.6	320.9	315.2	320.8	275	274
71	28.01	25,023	0.4507	5,013	29.5	1.50	44.1	150.4	319.0	310.6	293.1	322.7	323.6	314.6	314.6	299.0	274
72	13.25	24,974	0.4532	5,016	31.3	0.99	36.5	151.2	341.4	332.2	317.2	346.7	344.7	346.7	335.2	311.9	284

Table 20. Test Data for Tight Hybrid Bearing (P06)

Test Point	Run Time, Hours	Shaft Speed, rpm	Cage Speed Ratio	Thrust Load, lbf	Vibration, G's	Lube Flow, gpm	Power Draw, kW	Temperature, °F						Inner Race					
								Oil In	OR	Drive Sleeve	End Casing	Drain	OR	Drive	End	Sleeve	Casing	Drain	
73	29.59	12,513	0.4474	1,014	5.1	2.00	13.9	250.1	281.3	280.7	275.3	283.6	283.3	277.1	283				
74	30.11	12,495	0.4501	1,015	4.7	1.01	11.4	248.3	293.5	294.0	285.2	297.8	295.5	281.2					
75	5.85	12,502	0.4456	5,017	6.2	1.50	15.8	249.4	307.1	306.6	303.1	293.8	304.5	293.8					
76	25.39	18,748	0.4534	1,008	12.8	1.50	23.3	251.1	331.7	330.7	328.6	314.0	332.8	331.7					
77	19.53	18,750	0.4521	5,016	14.4	2.00	33.4	249.3	346.2	344.7	341.0	325.2	344.8	339.4					
78	26.03	18,774	0.4584	5,002	16.8	0.99	26.7	250.0	387.6	388.9	382.0	363.6	388.3	380.7					
79	26.75	25,008	0.4474	1,006	55.1	2.00	43.6	252.6	373.4	369.3	368.0	348.4	369.6	368.9					
80	21.37	25,016	0.4599	1,015	51.2	1.00	31.3	250.7	386.0	384.6	380.9	365.2	390.4	385.7					
81	21.82	24,971	0.4634	5,008	55.6	1.50	47.8	249.3	430.6	428.9	420.9	391.9	428.4	427.4					
82	24.53	12,487	0.4467	1,007	6.3	1.50	13.9	151.5	202.4	202.8	200.1	191.8	205.5	204.6					
83	7.18	12,502	0.4397	5,006	6.1	2.00	18.9	150.9	214.2	212.3	208.7	199.7	211.5	210.8					
84	8.24	12,498	0.4415	5,019	6.2	1.00	15.7	148.7	238.6	238.5	233.0	223.3	239.1	238.8					
85	27.62	18,751	0.4476	1,012	14.7	2.00	28.1	148.3	235.4	233.6	231.5	226.1	233.4	232.7					
86	28.17	18,724	0.4531	1,010	16.6	1.00	21.9	150.0	259.8	258.4	254.6	241.7	262.7	261.5					
87	10.01	18,775	0.4507	5,005	18.1	1.50	30.5	147.9	281.8	280.5	274.1	254.5	278.9	279.0					
88	28.89	25,034	0.4524	1,013	54.7	1.50	38.4	151.6	293.5	290.6	286.5	267.3	296.8	294.8					
89	23.01	24,989	0.4563	5,013	50.4	1.99	57.6	149.7	335.9	332.4	326.6	297.2	330.6	329.5					
90	23.42	25,003	0.4603	5,010	53.6	1.00	39.5	149.2	352.9	351.5	342.2	325.4	355.1	344.3					

Table 21. Test Data for All-Steel and Hybrid Bearings (P04 and P05)

Test Point	Run Time, Hours	Shaft Speed, rpm	Thrust Load, lbf	Vibration, G's	Lube Flow, gpm	Power Draw, kW	Lube Oil	ORC Oil	Temperature, °F						Inner Race				
									OR	Casing	Drain	ORC	OR	Drive	End	Sleeve	Casing	Drain	ORC
91	2.09	18,767	1,019	9.4	0.99	16.0	247.5	327.3	317.6	321.7	279.6	323.7	323.3	291.4					
92	2.78	18,778	1,018	10.2	0.50	14.6	247.6	325.1	343.5	331.8	335.5	291.3	343.1	293.4					
93	3.45	18,758	1,019	9.1	1.00	0.00	15.8	250.2	366.0	359.3	346.7	348.4	359.8	361.4					
94	4.21	18,721	5,020	14.7	1.00	1.00	18.9	249.1	358.7	345.4	354.4	294.1	354.0	352.8					
95	5.00	18,737	5,008	15.9	0.50	0.99	17.1	246.4	253.4	382.0	366.2	373.4	307.4	380.2					
96	5.72	18,747	5,006	19.2	1.00	0.00	18.6	249.6	404.6	395.7	382.9	383.0	398.5	399.3					
97	6.81	24,968	1,020	16.9	1.00	0.99	24.5	252.1	373.7	360.8	364.7	362.4	361.6	334.2					
98	7.56	25,030	1,019	17.3	0.51	0.99	22.0	249.5	392.2	376.8	380.6	310.7	381.7	330.5					
100	8.54	24,986	5,002	37.9	0.99	0.99	250.3	248.7	406.5	388.4	398.4	313.8	394.6	392.5					

Appendix B

Ceramic-Chip Detector Technology Selection Matrix

This appendix presents a comprehensive matrix (Table 22) of 21 potential techniques for detecting ceramic chips, with a view for detecting incipient failure in hybrid ceramic bearings. The evaluation criteria were:

- cost,
- reliability,
- full-flow monitoring capability,
- on-line operation,
- real-time detection capability,
- capability to detect debris size $> 200 \mu\text{m}$,
- early warning capability (indication after 10 chips),
- current availability, and
- capability to detect metallic and nonmetallic debris.

Table 22. Ceramic-Chip Detector Technology Selection Matrix

Technique	Standard Size Range (µm)	Type of Failure Detected	On-Line Capable ?	Bubble Discrimination ?	Flow Rate	Material Detection Limits	Manufacturer	Comments: (+) Benefits; (-) Drawbacks	Being Considered ?
Ultrasonic (UT)	< 40	Any debris	Yes	Some	Full flow	None	Monitek	<ul style="list-style-type: none"> • Could adapt to >200 µm by defocussing (+) • Requires development (-) • Needs debris-retention device (-) 	Yes
Laser/White Light/IR/Hologen	0.1 – 300	Any debris	Yes	Some	Full flow	None	Particle Measuring Systems	<ul style="list-style-type: none"> • Could be used for >400-µm size debris (+) • Requires development (-) 	Yes
Inductive Debris	> 10	Metallic debris	Yes	Yes	Full flow	Metallic only	IDM/UTC, Smiths, Tyne	<ul style="list-style-type: none"> • Detects metallic debris only; not suitable for ceramic bearings (-) 	No
Spectrometric Soap	≤ 6	Any	No	No	0.3–1.5 cm ³ /s	None		<ul style="list-style-type: none"> • Established procedure in service (+) • Suitable for Si and Ni elements (+) 	No
Light Scatter	2 – 150		Yes	No	0.3–1.5 cm ³ /s	None	Malvern Instruments	• Not suitable for engine application (-)	No
Faraday Effect	0.1 mg	Ferrous debris	Yes		Full flow	Ferrous only	Simmonds Precision	<ul style="list-style-type: none"> • Light transmission affected by presence of magnetic particles only; unsuitable for ceramic bearings (-) 	No
Vibration		Rolling, turning, pumping elements and effects	Yes	Yes	Not in flow	Improper alignment and impact effects	Vibrometer, Endevco	<ul style="list-style-type: none"> • Accelerometers to be located at bearing housing; need one for each bearing (-) • Debris not captured (-) • Would discriminate/locate failure (+) 	Yes
Detectable Coatings		Coating debris	Yes	Yes	Full flow	Coatings only		• Not suitable for silicon nitride balls (-)	No
Radioactive Doping	Depends on doping strength	Doped material	Yes	Yes	Full flow	Depends on material	Oakridge National Laboratory	<ul style="list-style-type: none"> • No suitable isotopes with reasonable half-life, for silicon nitride; only feasible with impurity implantation on bearing surface (-) • Safety issues (-) 	No
Ferrous Debris Monitor	1 – 1000 200 – 1000	Large particles	Yes	Yes	Full flow	Ferrous only	Ferroscan	• Unsuitable for ceramics (-)	No
Capacitance Debris Monitor		Capacitance change in oil	Yes	Maybe	Full flow		Smiths Industries	<ul style="list-style-type: none"> • Since oil and silicon nitride capacitance are similar, would not detect debris in oil (-) 	No

Table 22. Ceramic-Chip Detector Technology Selection Matrix (Concluded)

Technique	Standard Size Range (μm)	Type of Failure Detected	On-Line Capable?	Bubble Discrimination?	Flow Rate	Material Detection Limits	Manufacturer	Comments: (+) Benefits; (-) Drawbacks	Being Considered?
Capacitance Debris Monitor		Capacitance change in oil	Yes	Maybe	Full flow		Smiths Industries	<ul style="list-style-type: none"> Since oil and silicon nitride capacitance are similar, would not detect debris in oil (-) 	No
Fiber-Optic Bearing Monitor		Failures detectable thru race	Yes			None	MTI, Philtac	<ul style="list-style-type: none"> Must be mounted adjacent to outer race (-) Need one for each bearing; debris not captured (-) Would discriminate/locate failure (+) Similar to vibration technique (+) 	Yes
Electric Chip Detector	3 - 1000	Ferrous debris	Yes	Yes	Full flow	Ferrous only	Tedco	<ul style="list-style-type: none"> Relies on magnetic collection of debris; unsuitable for nonferrous (-) 	No
Pulsed Electric Chip Detector	> 15	Ferrous debris	Yes	Yes	Full flow	Ferrous only	Tedco	<ul style="list-style-type: none"> Relies on magnetic collection of debris (-) Small debris suppressed by current pulse (+) 	No
Full-Flow Screen	> Screen size	Any debris	Yes		Full flow	None		<ul style="list-style-type: none"> Need indication of debris trapped by screen (-) Ultrasonics or laser detection are good candidates (+) 	Yes
Indicating Screen Chip Detector	> Screen size	Metallic debris	Yes		Full flow	Metallic only		<ul style="list-style-type: none"> Uses electric chip detector to sense trapped debris; unsuitable for ceramics (-) 	No
X-Ray Fluorescence Monitor	Depends on radioactive source	Metallic debris	Yes	Yes	Full flow	Metallic only		<ul style="list-style-type: none"> Hard to excite Si or Ni; unsuitable for ceramics (-) Safety issues (-) 	No
Magneto Resistive Sensor		Ferrous debris	Yes	Yes	Full flow	Ferrous only		<ul style="list-style-type: none"> Relies on magnetic properties; unsuitable for ceramics (-) 	No
Pressure Differential	> Screen size	Any debris	Yes	Yes	Full flow			<ul style="list-style-type: none"> Sensitivity an issue for detection of few chips: 10 chips vs 1000 holes (-) 	No
Tube Tuning Fork	> Screen size	Any debris	Yes	Yes	Full flow			<ul style="list-style-type: none"> Sensitivity an issue in engine vibration environment (-) 	No
Acoustical Target	> Screen size	Any debris	Yes	Maybe	Full flow			<ul style="list-style-type: none"> Affected by background engine noise (-) Affected by fluid turbulence (-) 	No

Appendix C

Ultrasonic Scattering by Ceramic Debris in Oil

This appendix is a report prepared for GE Aircraft Engines by Haydn N.G. Wadley of the Intelligent Processing of Materials Laboratory, School of Engineering and Applied Science, University of Virginia (Charlottesville, Virginia 22903) in March 1992.

Introduction

General Electric's Aircraft Engines Division is exploring a novel method for determining the presence of ceramic debris in aircraft engine lubricants. It involves the capture (and alignment) of debris particles entrained in oil upon a coarse screen. The screen is positioned normal to a pulse-echo ultrasonic transducer and the reflected ultrasonic signal from the particles detected. Two of the factors that can affect the response of the sensor are the intrinsic absorption of the oil and the scattering characteristics of the particles. The work reported here calculates, as a function of frequency, the scattering intensity for oblate spheroidal particles of various sizes and shapes (aspect ratios) immersed in oil. From this it is possible to identify the best frequency to use for the inspection. Measurements of the attenuation of representative lubrication oils over the same range of frequencies are also reported. They enable the effect of ultrasonic attenuation to be assessed.

Ultrasonic Scattering Calculations

The problem to be considered is that of an ellipsoidal ceramic debris particle with density ρ' and elastic stiffness c' in a lubricant with density ρ^0 and stiffness c^0 . The incident ultrasonic wave displacement amplitude as a function of propagation distance can be written:

$$u_i^0(\vec{r}) = A_0 \frac{e^{ikr}}{r} \quad (1)$$

where A_0 is the initial amplitude of the wave (measured at the generating transducer), k is the wave number ($k = 2\pi/\lambda$ where λ is the wavelength), and \vec{r} is the propagation distance in the oil.

When this ultrasonic disturbance reaches a particle, it suffers partial scattering. The total wave field in the oil must be a linear superposition of these two fields:

$$u_i(\vec{r}) = u_i^0(\vec{r}) + u_i^{sc}(\vec{r}) \quad (2)$$

where the scattered field can be calculated from:

$$u_i^{sc}(\vec{r}) = \delta\rho\omega^2 \int_v g_{ij}(\vec{r} - \vec{r}') u_j(\vec{r}') dr' + \delta c_{jklm} \int_v g_{ij,k}(\vec{r} - \vec{r}') u_{l,m}(\vec{r}') dr' \quad (3)$$

and $\delta\rho$ is $\rho' - \rho^0$, δc_{jklm} is $c' - c^0$, ω is the ultrasonic frequency and g_{ij} is the Green's function for the oil (it relates the displacement at \vec{r} in direction u_i to the excitation force at \vec{r}' in direction j).

At low frequencies, the far field expression for the Green's function of the lubricant can be simplified:

$$g_{ij}(\vec{r} - \vec{r}) \approx \frac{1}{4\pi\rho\omega^2} \hat{r}_i \hat{r}_j k^2 \frac{e^{ikr}}{r} \quad (4)$$

and the scattered field far from the scatterer can be written as:

$$u^{sc}(\vec{r}) = A(\theta) \frac{e^{ikr}}{r} \quad (5)$$

where $A(\theta)$ is the scattering amplitude. A Born (weak scattering) approximation can be made by replacing the total field, u_i , in Equation 3 by the incident field, u_i^0 , whereupon the amplitude $A(\theta)$ is obtained as:

$$A(\theta) = \frac{ab^2k^2}{3} \left(\frac{\rho' - \rho^0}{\rho^0} \cos\theta - \frac{\lambda' - \lambda^0 + 2\mu' \cos^2\theta}{\lambda^0} \cos\theta \right) \quad (6)$$

where the particle has an oblate shape, and a and b are the (oblate spheroids) semi-axis lengths, ($a < b$), λ^0 is the modulus of the fluid, and λ' and μ' are Lame's elastic constants for the debris.

The ultrasonic intensity of the incident wave can be written:

$$I_{in} = \rho^0 \omega k A(\theta) / 2 \quad (7)$$

The intensity for the scattered wave is given by:

$$I_{sc} = \rho^0 \omega k A_\theta^2 / 2 \quad (8)$$

The relative scattering intensity (I_{sc}/I_{in}) can therefore be easily evaluated and the relative strength of scattering in a given direction obtained for any excitation frequency, ω , and oblate particle shape (defined by a/b).

Assuming the acoustic waves propagate from left to right and propagation is normal to the largest face of the debris particle, the scattering ratios shown in Figures 73–75 are obtained. For these calculations, it was assumed that for oil: $\rho^0 = 0.9 \text{ g/cm}^3$, and $\lambda^0 = 125 \text{ MPa}$ whilst for a silicon nitride debris particle: $\rho' = 3.2 \text{ g/cm}^3$, $\lambda' = 310.266 \text{ GPa}$ and it was assumed that Poisson's ratio $\nu = 0.3$.

Figure 73 shows that at the relatively low frequency of 1 MHz, the maximum scattering always occurs in the back-scattered or forward-scattered direction ($\theta = 180^\circ$ or 0°) for any oblate shape. Note that the scattering in the perpendicular direction ($\theta = 90^\circ$) is zero. The shape of the particle has a very significant effect upon the scattering intensity. Particles with an aspect ratio of 10 scatter approximately 4% of the incident intensity in the back-scattering direction at 1 MHz. This is reduced 4 orders of magnitude when the aspect ratio is reduced to 1.

A significant increase in the back-scattered intensity can be achieved by using a 5-MHz excitation frequency. For example, the scattering efficiency of a 10:1 aspect ratio particle is increased to almost 100% in the back-scattering direction. The scattering of spherical particles is also increased by increasing the frequency (see Figures 74 and 75).

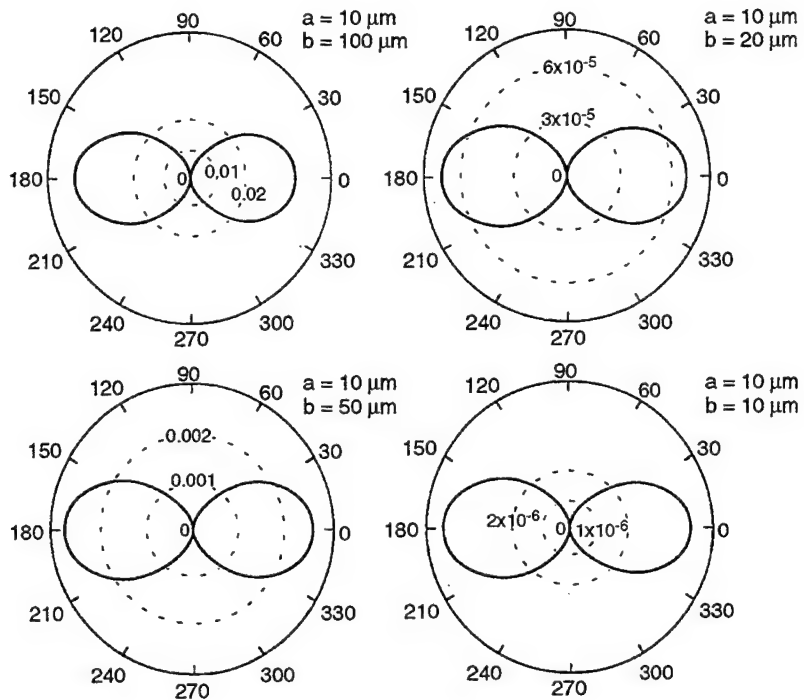


Figure 73. Calculated Scattering Amplitude of a 1-MHz Ultrasonic Frequency for Four Aspect Ratio Debris Particles *The ultrasonic disturbance propagates horizontally from left to right.*

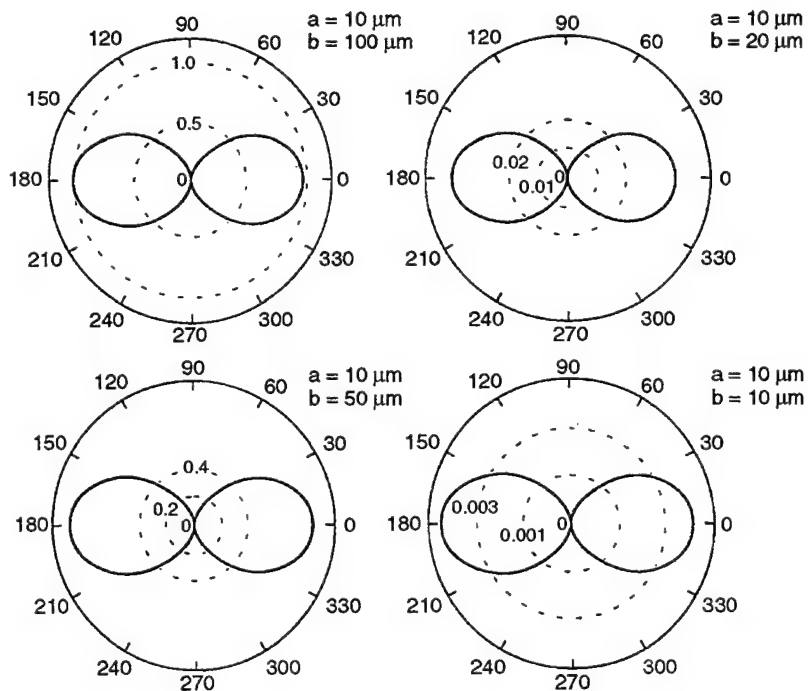


Figure 74. Calculated Scattering Amplitude at a 5-MHz Frequency for Four Aspect Ratio Debris Particles

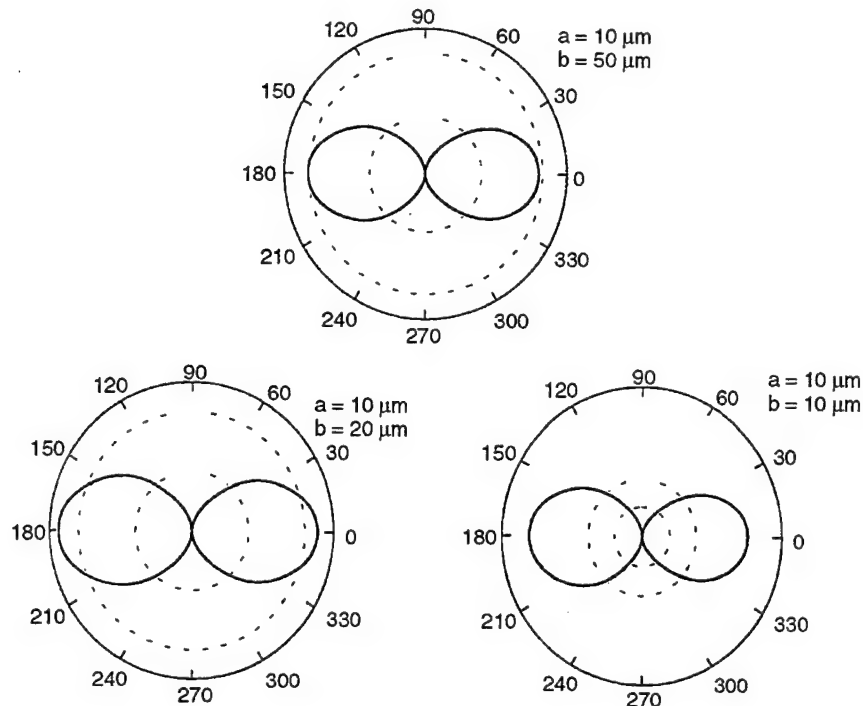


Figure 75. Calculated Scattering Amplitudes Ratio at a 10-MHz Frequency for Three Aspect Ratio Particles

To summarize, it appears essential to use excitation frequencies of 5 – 10 MHz for an efficient debris monitor and to ensure that entrapment upon screens results in particles aligned normal to the inspection direction.

Experimental Measurements

The results of the scattering calculations indicate that higher frequency measurements offer the potential of a stronger echo at the receiving transducer and thus an enhanced-reliability debris monitor. This can only be realized if the lubricating oil is able to efficiently propagate ultrasound at these frequencies. Measurements were performed to evaluate the intrinsic signal transmission characteristics of three typical aircraft oil engine samples provided by GE Aircraft Engines.

Figure 76 is a schematic diagram of the experimental test setup used to make the measurements. A 0.25-in diameter transducer formed part of the bottom surface of a test cell. Oil was placed in the cell and ultrasonic pulses caused to propagate between the transducer and the oil/air interface.

A series of echoes were obtained (Figures 77 – 79) from which the attenuation (defined as $20 \log A_i/A_{i+1}$ where A_i is the amplitude of the i -th peak) could be determined. A MATEC MBS-8000 measurement system was used for this. It utilizes a phase-sensitive detector to automatically measure echo amplitude and calculates an attenuation from the amplitude ratio of successive echoes. Figure 80 shows the dependence of the measured attenuation upon frequency.

The measurements indicate that there are small differences in the attenuation of the three oils and that there are small variations with frequency. The levels of attenuation are sufficient to perform measurements with a several-inch propagation path, but care needs to be taken if this is significantly increased.

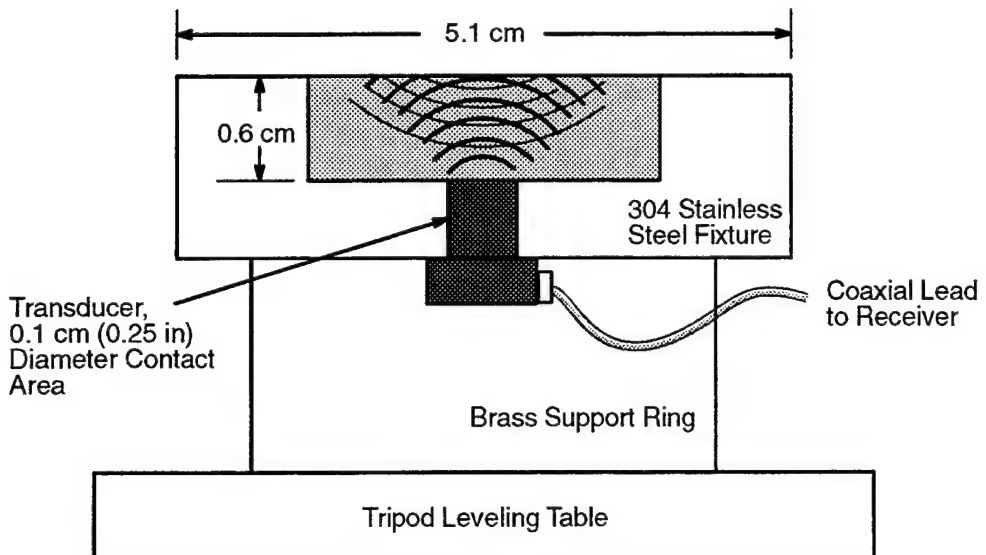


Figure 76. Experimental Test Setup used to Measure Lubricant Attenuation

Note, the measurements reported here may overestimate the severity of the attenuation because of (a) slight surface curvature of the oil surface, (b) lack of perfect planarity between the transducer and the oil surface, and (c) diffraction losses.

Summary

Calculations of the scattering from oblate-shaped ceramic debris have been performed to identify the factors controlling the detection reliability of an ultrasonic wear debris monitor. The calculations indicate that both the shape of the particle and the ultrasonic frequency affect the strength of the signal back-scattered from the particle. Spherical particles 10 μm in diameter scatter weakly at all frequencies between 1 and 10 MHz and will be difficult to detect. Increasing the major axis length of the debris particle significantly improves the detectability, as does an increase in the ultrasonic frequency. Measurements at 5 MHz are likely to result in good detection of oblate-shaped debris with a 100- μm major axis and 10- μm minor axis.

Measurements have been made of the ultrasonic attenuation of typical aircraft engine lubricants. The attenuation shows small differences with oil type/age and ultrasonic frequency. These differences are of insignificant relevance to the design of a wear-debris monitor. The absolute values of the attenuation may be overly conservative (too high) because of the effects of slight misalignments and diffraction losses in the test cell used.

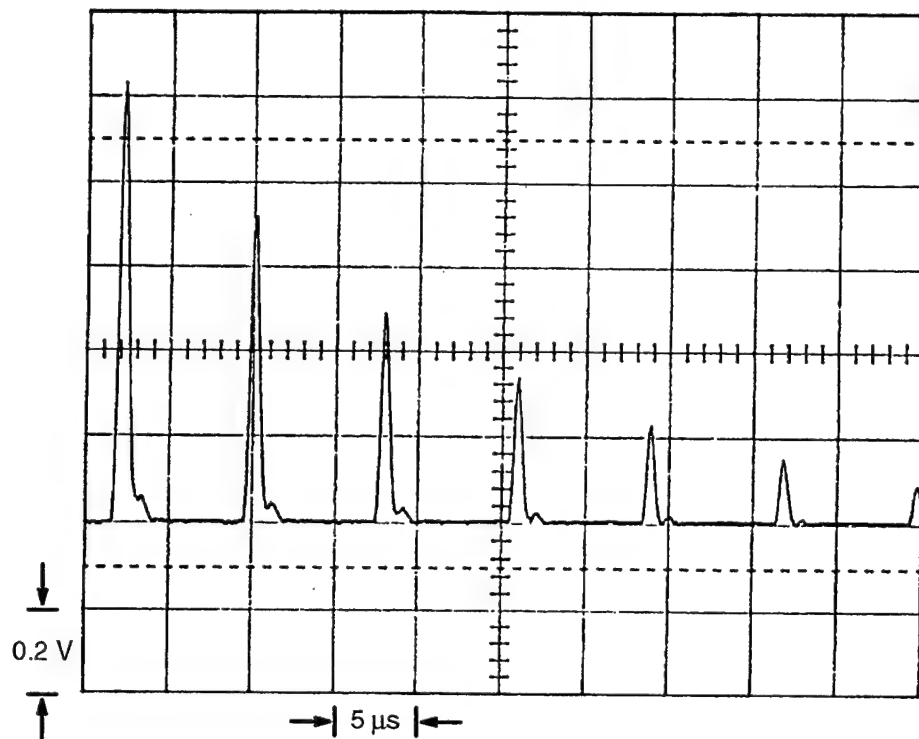


Figure 77. New 7808K Lubricant: Ultrasonic Amplitude (0.2 V/Division) versus Time (5 μ s/division) for Measurement of Attenuation at 5 MHz

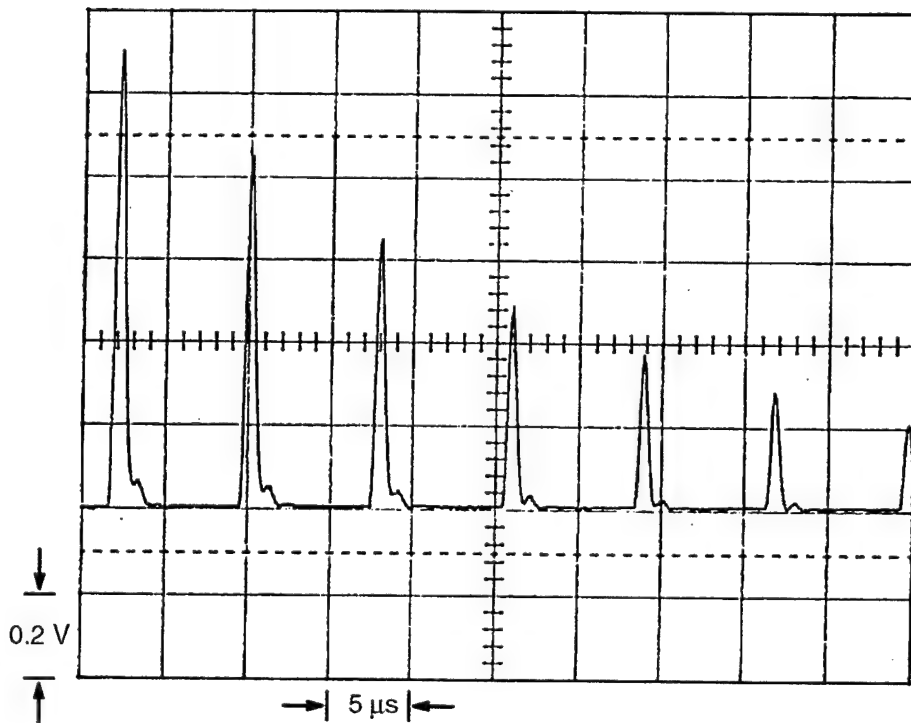


Figure 78. New 7808J Lubricant: Ultrasonic Amplitude Verses Time at 5 MHz

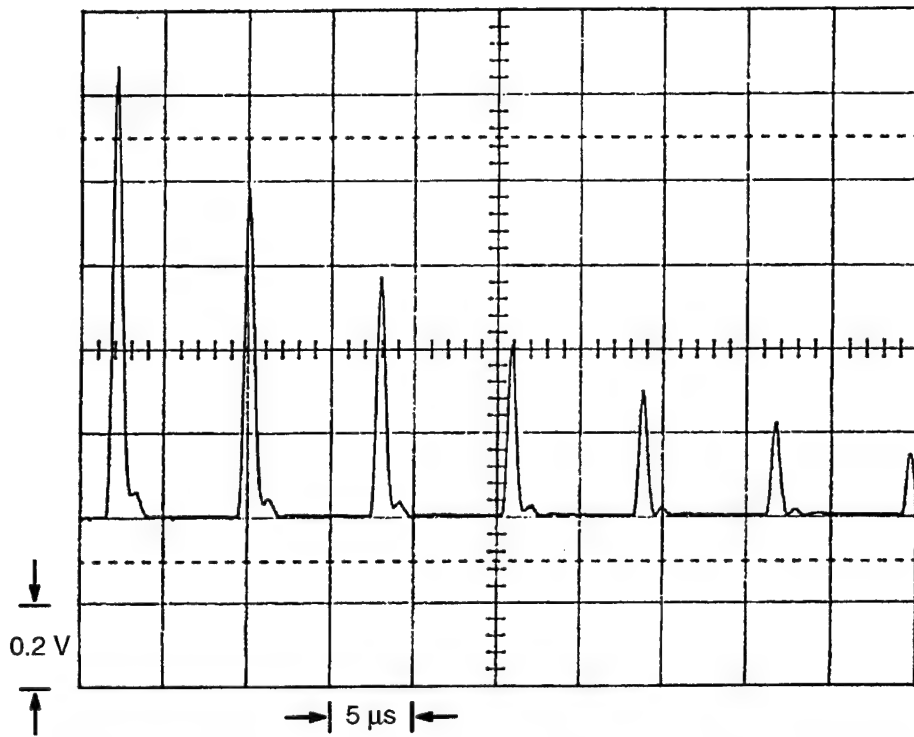


Figure 79. Used 7808J Lubricant: Ultrasonic Amplitude Versus Time

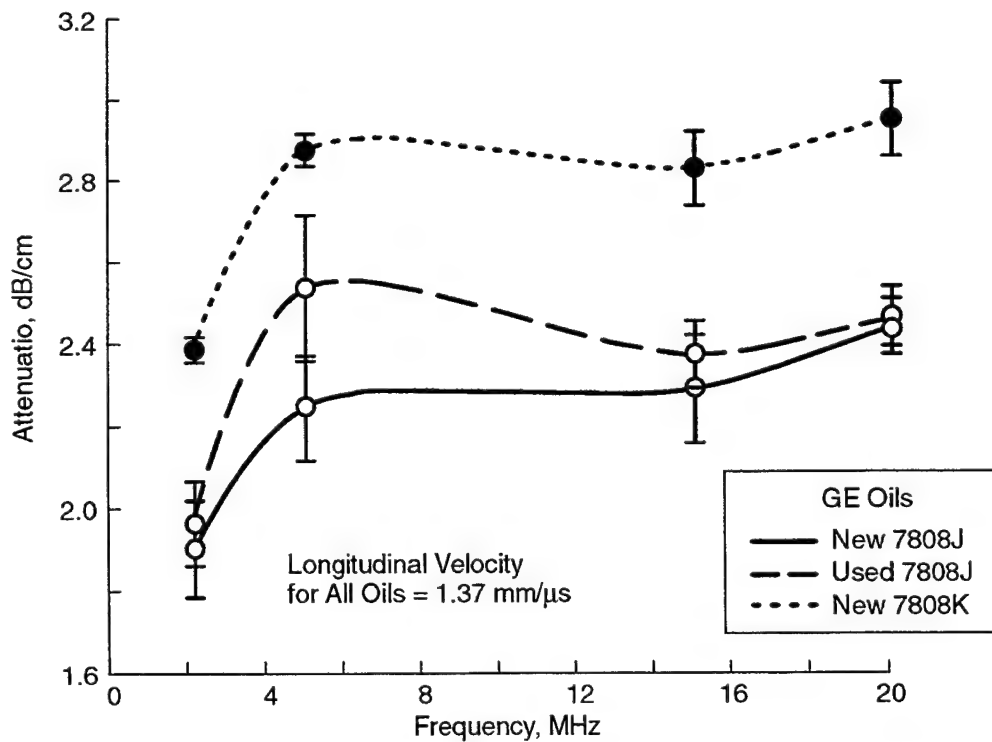


Figure 80. Measured (Average of 10 Tests) Ultrasonic Attenuation at Different Frequencies for Three Aircraft Engine Lubricants

Appendix D

Radioisotopic Detection of Si_3N_4 Bearing Chips

This appendix is a report prepared for GE Aircraft Engines by Haydn N.G. Wadley of the Intelligent Processing of Materials Laboratory, School of Engineering and Applied Science, University of Virginia (Charlottesville, Virginia 22903) in November 1992.

Objective

Low-level radioactive doping of finished rolling elements represents one potential approach to the detection of mainshaft hybrid bearing degradation. Suppose one were able to induce a low level of radioactivity in a bearing, and subsequently collect (in a filter) the resulting radioactive chips associated with degradation. Then, provided the chips were sufficiently radioactive, a detector placed either in or (preferably) outside the mainshaft bearing lubrication line might be able to detect the emission from the chips in real time. This would provide a timely indication of the need for a bearing inspection and satisfy our needs for a bearing degradation monitor. The objective of this report is to (a) determine the level of radiation needed for reliable chip detection, (b) assess methods able to operate in or adjacent to a flowing oil stream, and (c) evaluate their practical applicability to a mainshaft bearing.

For the approach to be successful, it must satisfy the following criteria:

1. A potential method must exist for radioactively labelling Si_3N_4 bearings.
2. The radioisotope must have a half life commensurate with the bearing life (5 to 10 years minimum).
3. The radioactivity from a single typical chip must be detectable at the detector location.
4. No unacceptable radiation hazard must be posed to engine assembly and maintenance personnel.

Isotopic Labelling

The most common method for inducing radioactivity in materials is to neutron irradiate them. This results in the formation of isotopes, some of which may be radioactive and decay by the emission of α and β particles, positrons, and γ rays. For the resulting radiation to be detectable, either within or outside a lubrication oil line, only γ -ray emitting isotopes are acceptable. The other radiations are too easily attenuated by the lubrication oil. It is also necessary for the radioactivity of the radioisotope to decay slowly compared with the service (and prior shelf) life of the bearings. Thus, one needs a half life for the radioisotope of 5 to 10 years or more.

A survey of nuclear data (K. Way et al., *Nuclear Data*, NBS Circular 499) has revealed that no long-lived γ -emitting radioisotopes can be produced by neutron absorption for any of the naturally occurring isotopes of nitrogen or silicon or for the isotopes of Mg and O which are present as MgO , an impurity of Si_3N_4 (1% concentration). Recent work at Implant Sciences Corporation (A.J. Armini and S.N. Bunker, "Wear Measurement of Ceramic Bearings in Gas Turbines," WRDC-TR-90-2078) has identified the possibility of proton activation of nitrogen through the reaction

$N^{14} + p \rightarrow Be^7 + 2He$. Whilst Be^7 is a γ -emitting radioisotope, it unfortunately has a half life of only 53 days, insufficient for our engine monitoring purposes (though it might be useful for laboratory studies of accelerated degradation). It thus appears that the only possibility for applying the radioisotopic labelling approach is to implant/dope the bearing surface (say the top 50 to 100 μm) with an impurity that emits γ radiation with the necessary half life. One almost ideal candidate for this is Co^{59} , a naturally occurring but nonradioactive isotope of cobalt. Upon neutron irradiation, the atom captures a neutron resulting in the formation of Co^{60} which is radioactive. Each Co^{60} decay results in simultaneous emission of two γ rays with energies of 1.17 and 1.33 MeV. The half life of Co^{60} is 5.2 years, a little on the short side for our application, but still acceptable.

Feasibility

To determine the concentration of Co^{60} required in the outer surface of the bearing, we need to specify a level of radioactivity that can be reliably detected at the detector position. As a first safe, but still easily measured, estimate assume a value of ~ 4 mr/h (4 milliroentgens per hour is about that from the front face of a luminous wrist watch). Let us assume that a γ -ray detector is positioned with respect to a chip collector as shown in the Figure 81 and initially that the chip-detector distance is 10 cm.

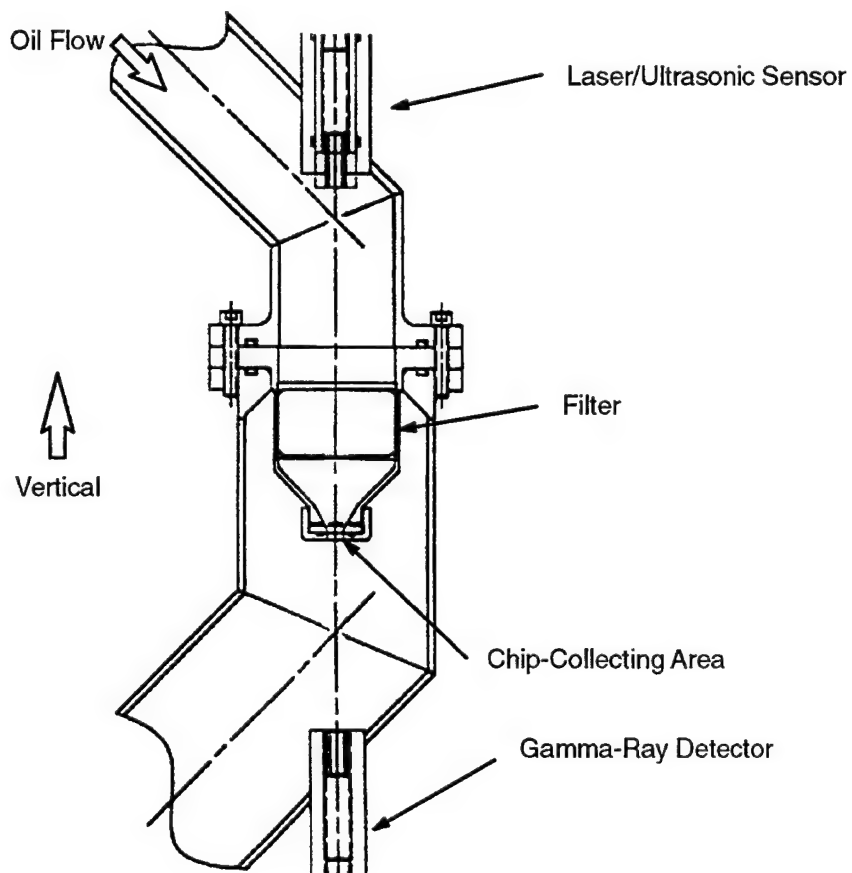


Figure 81. Schematic of Sensor Concept

We further assume a 5-mm thick sheet of steel separates (and protects) the detector from the oil flow. The dose rate at the detector a distance R (in cm) from a γ -emitting radioactive source C curies in strength is given (see S. Glasstone and A. Sesonske, *Nuclear Reactor Engineering*, Van Nostrand, 1955, p 524) by:

$$\text{Dose Rate (mr/h)} = (5.2 \times 10^6 C E_\gamma) \div R^2$$

where E_γ is the γ -ray energy in MeV. Thus, the minimum activity of the source (that is, the number of curies for a typical chip to be detectable) must be:

$$C = (4 \text{ mr/h})R^2 \div (5.2 \times 10^6 E_\gamma)$$

But this has ignored the attenuation of the γ rays by the intervening oil and steel. If we assume (to start) a 10-cm thickness of oil, this results in a 50% reduction of dose rate at the counter, whilst a 5-mm thickness of steel reduces this a further 30% (see G.E. Francis, W. Mulligan, and A. Wormall, *Isotopic Tracers*, Athlone Press, 1954, p 85). Thus, because of absorption, only 35% of the radiation reaches the detector. Therefore, the minimum chip activity needs to be at least:

$$\begin{aligned} C &= (4 \text{ mr/h})R^2 \div (5.2 \times 10^6 E_\gamma 0.35) \\ &= (4 \text{ mr/h})(100 \text{ cm}^2) \div (5.2 \times 10^6)(2.5)(0.35) \\ &= 0.9 \times 10^4 \text{ curies} \end{aligned}$$

where E_γ is taken as the sum of the energies of the two γ rays:

$$E_\gamma = 1.13 + 1.17 \text{ MeV} = 2.5 \text{ MeV}$$

This is a modest level of activity.

The number of grams, G , of Co^{60} required to achieve this level of activity can also be calculated (from Glasstone and Sesanske, p 525):

$$G = C A t_{1/2} \div 1.3 \times 10^{13}$$

where A is the atomic weight and $t_{1/2}$ is the isotope half life in seconds. We find:

$$G = (0.9 \times 10^4 \text{ curies})(60 \text{ amu})(1.7 \times 10^8 \text{ s}) \div (1.13 \times 10^{13}) = 8.1 \times 10^{-8} \text{ g}$$

If only a single chip is to be detected, then this mass of Co^{60} must be contained in a single chip of Si_3N_4 . Assuming such a chip to have dimensions of $500 \times 500 \times 25 \mu\text{m}$, its weight, G' , is:

$$G' = (500 \times 500 \times 25) \times 10^{-4} \text{ cm}^3 \times 3.2 \text{ g cm}^{-3} = 2 \times 10^{-5} \text{ g}$$

Thus, the concentration of Co^{60} (i.e., G/G') required for single-chip detection is 0.4 wt%. If one were interested in less-sensitive damage detection, say attempting only to detect the accumulation of 10 chips, then obviously the needed concentration could be decreased proportionally (i.e., to 0.04 wt%). There would be a further big advantage associated with reducing the distance between the chips and the detector. Reducing this distance from 10 to say 1 cm would reduce the needed Co^{60} a further factor of 100 (down to only 4 ppm). This level of doping could be easily accomplished by ion implantation and is likely to have a modest effect on the bearing durability, though this would need to be confirmed experimentally.

It is possible to evaluate the health/safety issue associated with the use of radioactively labelled bearings. Suppose Co is implanted uniformly to a depth of 50 μm below the surface of a 2-cm

diameter bearing. The volume of radioactively labelled material would be $6.25 \times 10^{-2} \text{ cm}^3$. If we assume first a worst case of single-chip detectability with a source-detector distance of 10 cm, we find that the bearing must contain $8 \times 10^{-2} \text{ g}$ of Co^{60} . Thus, the activity $C=1$ curie. The dose rate experienced at a location 10 cm from such a bearing would be 130 r/h; a serious dose rate requiring precautions so stringent that one would probably be uninterested in the method. However, if we assume the need for only a 10-chip detectability criterion, and a source-detector spacing of 1 cm, the dose rate for a bearing falls to 130 mr/h. This level can be dealt with using well-established safety procedures during storage and assembly of the bearings and during the maintenance of the engine. There would be a small hazard to personnel positioned near a completed engine and, depending upon the size and number of engine bearings installed, further warnings/screening might be necessary. These safety factors could all be further improved by reducing the needed dose rate at the detector. A value of 4 mr/h has been assumed necessary to this point. Reducing it to say 0.4 mr/h (but beware that the cosmic background at sea level is 0.1 mr/h) would reduce the safety hazard by a factor of 10, but at the expense of a decreased detection reliability.

Conclusions

The radioactive labelling of Si_3N_4 hybrid bearings has been proposed as a method for *in situ* monitoring of bearing damage. A review of labelling approaches has identified only one a possibility, the implantation of a foreign element (such as cobalt) in the surface of the bearing and its subsequent activation by neutron irradiation. Calculations indicate a required cobalt concentration of as little as 4 ppm in the implanted layer if one seeks to detect only the accumulation of significant damage (say 10 chips) in a filter located 1 cm from an efficient γ -ray detector. These levels of implantation are likely to minimally affect the bearing durability.

Estimates of the health/safety danger have also been made. In a worst case situation where one attempted to detect only a single chip with a detector positioned 10 cm from the source, substantial risk would be posed to workers, especially during assembly when 8 to 10 bearing elements are present. There could even be significant radiation exposure on the outside of an assembled engine. However, for a 10-chip detectability criterion, a 1-cm detector/source spacing, and with a tradeoff in the monitor reliability, this safety hazard could be significantly reduced, and satisfactory procedures might be developed to allow safe implementation.

Appendix E

Risk-Reduction Experiments

Effect of Mesh Material on UT

Objective: The objective was to study the amount of change (from the background reflection due to mesh) one would expect from the mesh material and the chips.

Setup: Figure 82 shows the configuration used for the experiment. The setup involves a transducer looking at the reflection from a screen/mesh with some glass particles (approximately 10). Glass particles were used because ceramic particles were not available and the ultrasonic properties of glass are quite similar to those of silicon nitride. Reflection from the mesh alone was measured, and later the reflection from the mesh and glass particles was measured. Comparison of the measurements shows the loss of reflection due to the presence of irregular scatters in the ultrasonic beam.

Two types of mesh material (steel and nylon) were investigated. The mesh size for the steel was 75 and 250 μm ; and the nylon was 70 μm . The results are tabulated for two transducer frequencies (5 and 10 MHz). Also, the effect of a perfect reflector (a stainless steel plate) was assessed. The transducers were 9.5 mm (0.375 in) in diameter and had approximately 2 to 2.5 cm (80 to 100 mil) beam diameter; focal length was either 5 cm (2 in) or 7.5 cm (3 in).

Table 23 shows effects of mesh size, mesh material, transducer separation distance, and transducer frequency on the loss of reflection due to the presence of irregular scatterers in the ultrasonic beam.

Results:

1. The focal length doesn't seem to cause a large change in amplitude (good).
2. The finer the mesh, the bigger the difference.
3. The higher the frequency, the bigger the difference.
4. The finer steel mesh and the nylon mesh both provided good change in signal strength.
5. Nylon material is frequency insensitive and produced a large change in both 5 and 10 MHz; hence, it is a good candidate for mesh material and should be considered for future tests.

UT Attenuation of New and Used Oil

Frequency-dependent ultrasonic attenuation was measured (Figure 83) for new 7808K, new 7808J, and used 7808J oil. The results show that at 2.25 MHz the attenuation for both new and used oil is the same; hence, this frequency was selected for the ultrasonic condition-monitoring device.

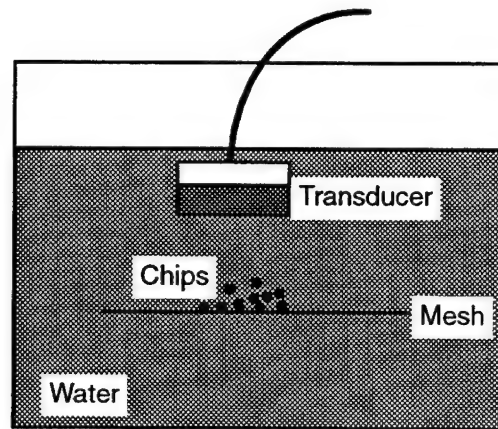


Figure 82. UT Experiment

Table 23. Loss of Reflection Due to Irregular Scatterers in Ultrasonic Beam

Material*	Frequency (MHz)	Focus (cm)	Number of Chips	Change (%)	Signal with Mesh and Chips	Signal with Mesh Only
S75	5	5	10	17	62	75
S75	5	7.5	10	20	60	75
S250	5	5	10	40	42	70
S250	5	7.5	10	59	38	68
S500	5	5	10	42	50	86
S500	5	7.5	10	43	50	88
N70	5	5	10	63	28	76
N70	5	7.5	10	62	32	84
S304	5	5	10	08	75	82
S304	5	7.5	10	12	72	82
S75	10	5	10	57	18	42
S75	10	7.5	10	65	12	35
S250	10	5	10	62	06	16
S250	10	7.5	10	60	06	15
S500	10	5	10	46	42	78
S500	10	7.5	10	49	38	74
N70	10	5	10	62	30	78
N70	10	7.5	10	58	34	80
S304	10	5	10	34	54	82
S304	10	7.5	10	41	44	74

* The nomenclature is as follows:

S75 Stainless steel mesh with 75- μm holes
 S250 Stainless steel mesh with 250- μm holes
 S500 Stainless steel mesh with 500- μm hole)
 N70 Nylon mesh with 70- μm holes
 S304 Stainless steel plate with no holes (perfect reflector)

Sensitivity of IR

Objective: To study the sensitivity of the CCD (ceramic-chip detector) when the laser light passes through a transparent film with varying numbers of dark spots.

Setup: Figure 84 is a schematic of the measurement setup used to evaluate the sensitivity of the laser source in detecting the random dots used to simulate ceramic chips. The laser beam passes through a beam splitter and then through a transparent film with dark dots. The resulting light transmitted through the sheet is received by a photodetector. The scope provides a quantitative measure of the light energy transmitted through the film.

This experiment was conducted to test the capability of the photodetector in sensing small changes when the beam is partially blocked by dark spots. The dark spots represent small ceramic chips. Table 24 shows the response received by the CCD light detector.

Results: The results show that this detector can detect small changes in light transmission.

Table 24. CCD Response

Number of Spots	Millivolts
11	10
10	12
9	10
8	8
7	8
6	4
0 (Bare Film)	0

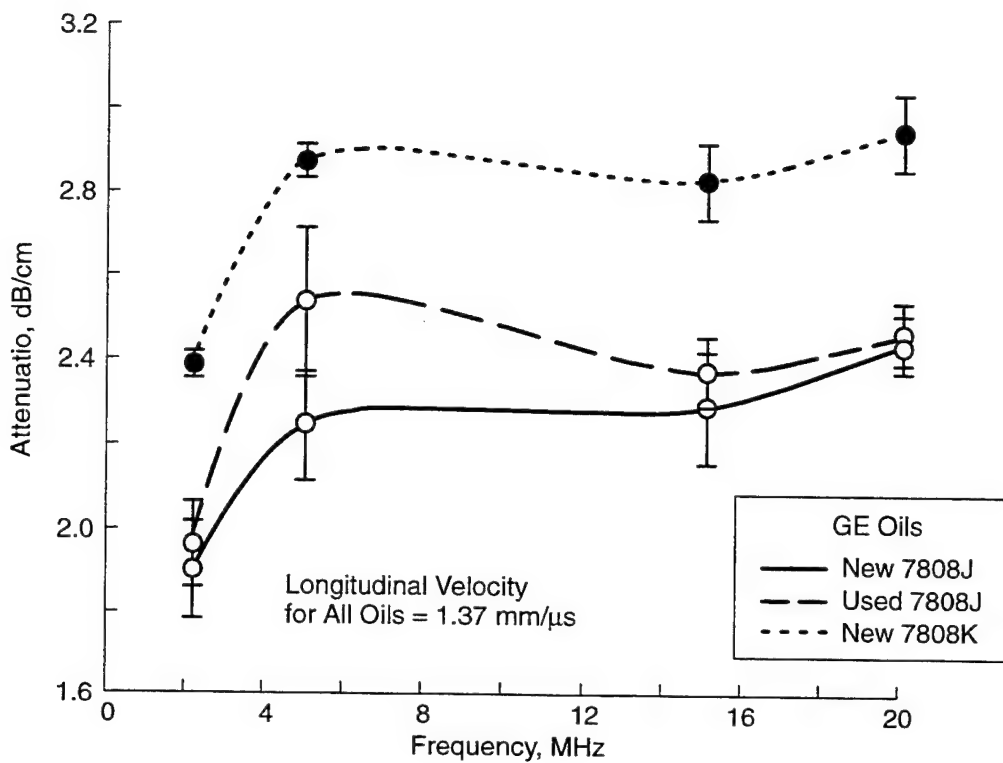


Figure 83. Attenuation vs Frequency for New and Used Oil

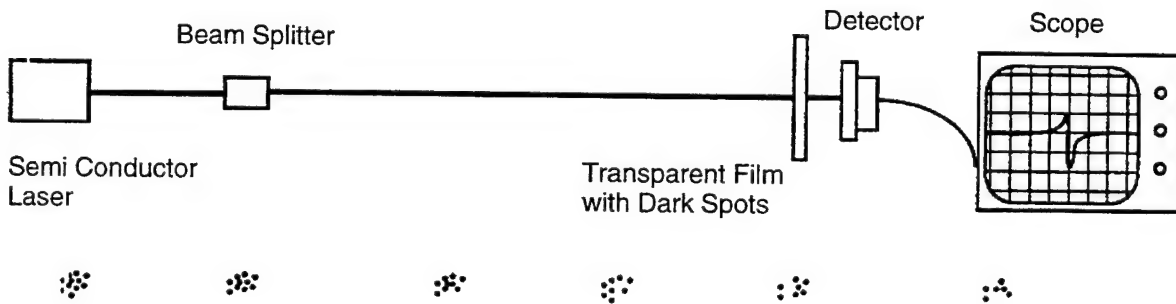


Figure 84. Schematic of Sensitivity Measurement

IR Attenuation of New and Used Oil

Frequency-dependent infrared transmission was measured (Figure 85) for new and used 7808J oil. The results show that between 900 and 1000 nanometers, transmissivity for new and used oil is the same; hence, 880 nm was selected for the infrared condition-monitoring device — as infrared sensors are commercially available at that frequency.

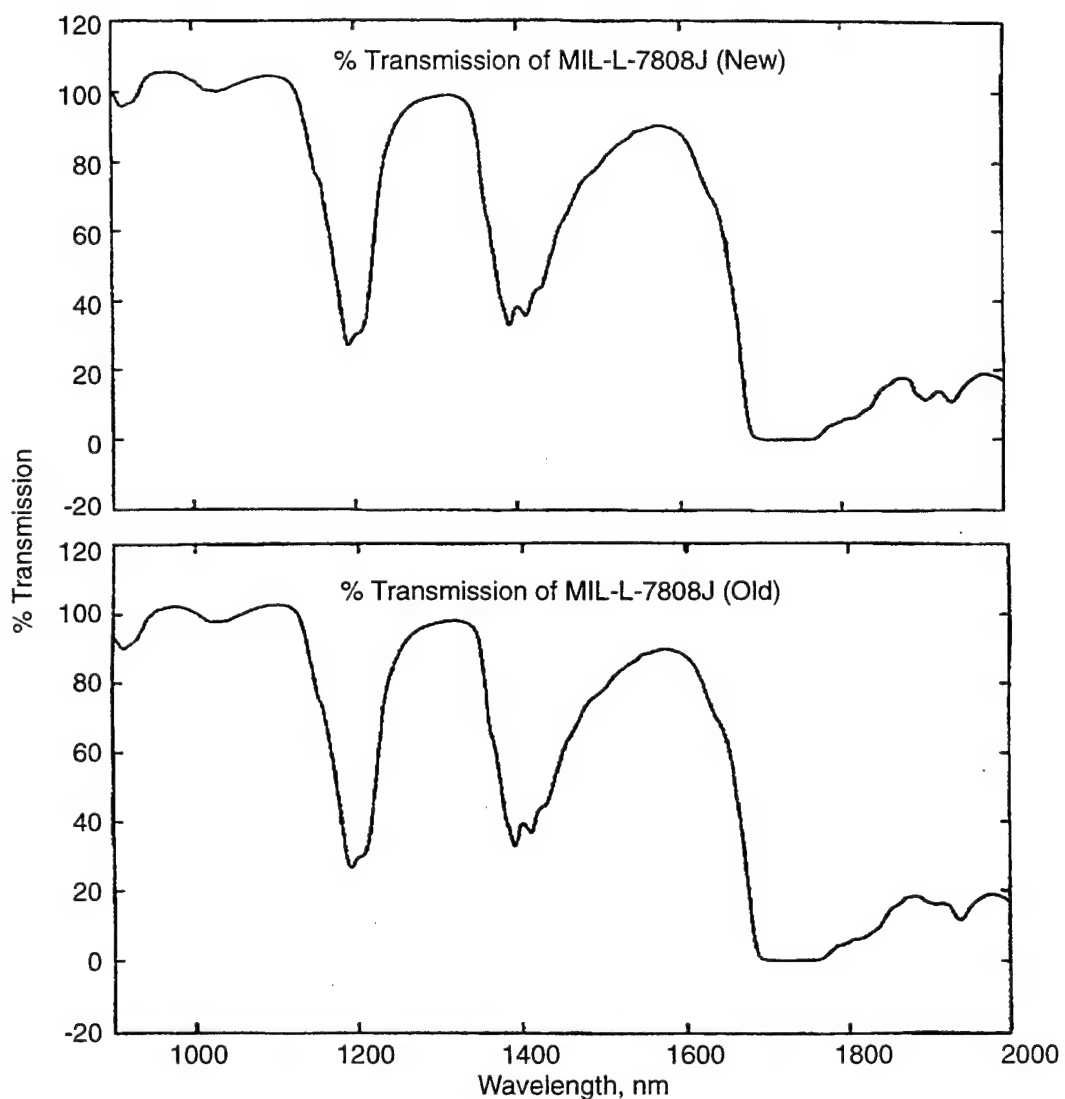


Figure 85. Infrared Transmission vs Wavelength for New and Used Oil

Appendix F

SKF Condition-Monitoring Application

This appendix is based on Report RFM L275669, "Condition Monitoring of Bearing Test," dated October 15, 1994, prepared by André J. Smulders. It has been reformatted, edited slightly, and reprinted by permission of SKF Condition Monitoring Inc., San Diego, CA.

History

A bearing degradation test was performed with an EDM notch in the outer race of a hybrid bearing with ceramic rolling elements running under normal (varying) loading conditions. Progress of defect development was to be observed along with that of any newly developed defects detected, specifically ball spalls.

Introduction

The vibration measurements performed on the GE engine test rig tracked the bearing degradation from the seeded race defect to final failure. Vibration was measured, in three directions, using three twin sensors. Three measurement formats were used:

1. Acceleration: The accelerometer measured vibrations in the horizontal, vertical, and axial planes. The signals were digitally sampled and transformed to acceleration spectrums by the resident wide dynamic high resolution FFT processor.

2. Acceleration Enveloping: The same accelerometer signals were modified by selected band pass filters prior to a demodulation processor, to isolate the defect overrolling generated impulses. The enveloping demodulation process enhances the repetitive phenomena and so improves its signal to noise ratio versus sinusoidal signals. These impulsive repetitive amplitudes are enveloped, sampled, and FFT converted to spectrum and time domain displays.

3. SEE Technology: Acoustic emission transducers, which are built into the accelerometer housing to form a twin sensor, are responsive to surface stress waves that result from the periodic surface contacts generated by the rolling elements impacting the race defects. These acoustic emission signals are mainly generated by wear conditions: scuffing, sliding, and impact with nonelastic material deformation in bearings. The signals, which are above sonic frequencies of 100 to 500 kHz, are filtered and demodulated to base band, sampled in the time domain, and FFT converted to the spectrum analysis frequency span.

Measurement Theory

Acceleration: The accelerometer is a transducer that measures the acceleration structural response to the vibration forces generated within the machine. These complex signals are a composite of large, low-frequency vibrations that are often due to imbalance misalignment as well as the small impulse forces that result from bearing rolling element defects. Acceleration response to bearing defects is generally seen as small amplitude spectral components that are frequently imbedded in noise.

When the bearing defects are in the early stages of a failure mode, the acceleration spectrum will not prominently display the peaks symptomatic of bearing defects. In the later bearing failure stages,

the bearing defect spectral lines are more identifiable but often require display markers that are assigned to the display by optional bearing library modules. When these bearing problem indicators appear in the acceleration spectrum, it is assumed there is enough remaining service life to schedule the bearing change-out at convenient intervals.

The advantage of enveloping techniques is that the maintenance engineer is made aware of a bearing failure process early enough to apply possible proactive corrective measures that would prolong bearing service life.

Acceleration Enveloping: Enveloping methods modify the acceleration response signal to isolate the bearing defect impulsive components from the normal higher amplitude, low-frequency vibration components. A bearing defect response signal is a narrow-width, small-amplitude repetitive pulse that is mixed with the normal vibration signals such as imbalance, misalignment, structural resonances etc. The enveloping measurement sequence first applies band pass filtering to attenuate the unwanted low-frequency signals and the high-frequency noise, attributed to other defect sources, enhancing the bearing signal-to-noise ratio. The enveloping functions to translate the higher harmonically related defect components to base band. Once these spectral components have been formatted by the enveloper sequence to appear as a harmonic series in the FFT analysis range, the bearing signature is easily identified by the defect spectral markers.

If there is not a defect, the impulse signals are not combined with the complex vibration components and the envelope spectrum will not display bearing harmonic amplitudes. The major advantage of enveloping is to provide an early warning of the initial stages of a progressive failure mode. Often proactive procedures are possible, such as correction of imbalance or lubricant breakdown or misalignment or raceway relocation to a new load position, to extend the bearing service life.

Another form of enveloping uses an acoustic emission transducer which has the advantage of sensing surface contact wear signals, often independent of low-frequency vibration.

SEE Technology: The acoustic emission transducer transmits a voltage signal in the 100 to 500 kHz range that is related to the structural stress waves generated by bearing surface contact between rolling elements and the raceways. These periodic occurrences can be attributed to lubricant breakdown, spalls, surface defects, particle contaminants, etc.

Acoustic emission has the spatial advantage of localizing the measurement by inherently discriminating against distant attenuated component signals. These localized high-frequency signals are again band-pass filtered prior to the enveloping process. The enveloper performs the same function as in acceleration enveloping to translate the defect response to the measurable analysis range. Once these spectral components have been formatted vectorially, the recognition pattern indicators can be more easily applied to diagnose bearing problems.

Lubrication failures are often a measurable quantity in the early stages of bearing wear. Lubrication concerns are related to viscosity change, contaminants, particle density, etc. Intermittent surface contacts caused by lubricant problems are sensed by the SEE transducer and demodulated to a measurable signal for both time and frequency domain analysis. Again, if there are indicators of such problems, the user can elect to change the bearing lubricant to effect corrective action. If the new lubricant does not reduce the SEE signal, spectral analysis of the harmonic series will allow early defect diagnosis.

Results

Each of the measurement modes did show positive evidence of the outer-race defect from the very start of the life test. Normally, enveloping techniques and specifically acoustic emission enveloping (SKF's SEE Technology) reveal the very early onset of the bearing defect stages which are the precursors to the more degenerative process of mechanical failure.

General Conclusions

The investigation measured the evolution of a seeded outer-race bearing defect from the initial period to the time when there was a high probability of an immediate failure.

The measurement encompassed the three vibration/acoustic format types. It was previously stated that the bearing defect was so dominant that even in the acceleration spectrum display the outer-race defect line components were clearly visible.

As the bearing defect progresses towards a catastrophic failure, other mechanical changes can take place within the bearing to cause impulsive 1^* harmonic amplitudes to appear in the envelope spectrum. The term 1^* indicates a single multiple ($1\times$) a fundamental measurement; in this case, it's rotational speed of the bearing. When the bearing clearances become excessive in the late stages of bearing life, the 1^* spectral harmonic components are probable indicators of an imminent failure. Although the growth of the 1^* component trend seen in both acceleration enveloping and SEE is a reasonable criteria for determining bearing end of life, it is not exclusive.

Other mechanical failure conditions unrelated to bearing defects can also produce impulsive 1^* vibration components in the envelope spectrums. Measurements at other bearing locations on the same shaft would provide more data to narrow the defect diagnostic estimate.

The bearing life test applied a constant axial hydraulic loading that tends to reduce the effects of clearance as it is developed in a normal bearing application. The probability that 1^* impulsive forces due to end-of-life clearance is a positive indicator of approaching failure should be investigated further.

There were other spectral defect indicators of late-stage bearing deterioration, which appeared periodically and with sufficient consistency to warrant urgent bearing replacement. High-level ball spin and cage defect spectral components were viewed in several spectrum displays occurring in the final intervals of the life test. It is known that when these defect signatures appear, the bearing is severely damaged and close to the end of life. It is impossible to accurately estimate the remaining life before catastrophic failure, but these dominant failure characteristics suggest immediate action is required to avoid more costly process down-time maintenance.

Measurement Results Overview

Maximum values for different measurements cycles are listed in Table 25.

Table 25. Maximum Acceleration, Acceleration Enveloping, and SEE Measurements for Eight Different Cycles

Measurement Units

- Acceleration: G's (Approximately $32 \text{ ft/s}^2 \approx 10 \text{ m/s}^2$)
- Acceleration Enveloping: G's
- SEE: Transducer Signal

Measurement	Direction	Cycle							
		1	2	3	4	5	6	7	8
Acceleration 10 kHz	Vertical	0.6	7.8	6.2	11.6	13.6	13.0	10.4	3.3
	Horizontal	0.7	3.7	5.0	6.5	4.0	6.3	6.0	4.5
	Axial	15.2	33.6	11.7	31.3	14.1	11.1	7.6	20.2
Acc Enveloping 10 kHz	Vertical	3.0	4.8	5.2	30.8	4.4	5.4	13.1	5.3
	Horizontal	3.2	2.1	3.8	5.1	1.4	2.3	5.2	3.1
	Axial	15.1	40.6	10.6	31.2	13.6	11.3	20.2	26.2
SEE 10 kHz	Vertical	28	52	80	12m	58m	51m	53m	39m
	Horizontal	23	46	75	11m	54m	49m	51m	35m
	Axial	250	250	12	10m	44m	43m	28m	15m
Acceleration 3 kHz	Vertical	2.4	8.7	5.2	22.2	10.7	12.2	7.5	2.4
	Horizontal	0.7	5.0	4.6	7.8	4.1	4.8	4.7	3.7
	Axial	1.1	13.1	13.3	10.0	6.7	8.5	4.0	4.7
Acc Enveloping 3 kHz	Vertical	3.0	2.4	2.8	25.3	4.5	5.5	7.2	3.5
	Horizontal	3.1	1.1	2.6	4.0	1.0	1.9	3.8	1.8
	Axial	13.4	26.9	6.9	25.1	15.3	10.5	16.3	15.8
SEE 3 kHz	Vertical	31	50	88	11m	56m	50m	53m	37m
	Horizontal	20	48	64	12m	57m	49m	51m	38m
	Axial	250	222	40	9m	51m	40m	23m	22m
Acceleration 300 Hz	Vertical	0.7	0.3	0.7	0.2	0.2	0.3	0.8	0.4
	Horizontal	0.4	0.2	0.4	0.2	0.2	0.2	0.4	0.4
	Axial	0.7	0.3	0.7	0.4	0.3	0.4	0.8	1.2
Acc Enveloping 300 Hz	Vertical	0.9	0.4	0.5	7.5	1.2	1.4	2.7	1.3
	Horizontal	2.2	0.2	0.2	1.3	0.6	0.8	1.0	0.6
	Axial	2.4	5.7	4.5	9.3	9.6	4.7	3.7	4.3
SEE 300 Hz	Vertical	21	34	40	8m	46m	38m	46m	46m
	Horizontal	6	23	26	8m	34m	30m	35m	42m
	Axial	125	6	34	6m	30m	22m	14m	14m

Bearing Defect Frequencies at 8,700 RPM

Bearing designation	GE Ceramic
Pitch diameter [dm] (mm)	168
Rolling element diameter [DW] (mm)	22.22
Number of rolling elements [z]	20
Contact angle (degrees)	28.00
Inner ring speed (RPM)	8700
Bearing type code	3
Outer, housing, diameter [D] (mm)	0
Inner, bore, diameter [d] (mm)	133
Number of rows	1
Bearing type	Angular contact ball
Inner ring defect frequency (Hz)	1619.84
Outer ring defect frequency (Hz)	1280.16
Rolling element defect frequency (Hz)	1078.06
Inner ring rotational speed (Hz)	145.00
Cage rotational speed (Hz)	64.01
Rolling element rotational speed (Hz)	539.03

Bearing Defect Frequencies at 14,100 RPM

Bearing designation	GE Ceramic
Pitch diameter [dm] (mm)	168
Rolling element diameter [DW] (mm)	22.22
Number of rolling elements [z]	20
Contact angle (degrees)	28.00
Inner ring speed (RPM)	14,100
Bearing type code	3
Outer, housing, diameter [D] (mm)	0
Inner, bore, diameter [d] (mm)	133
Number of rows	1
Bearing type	Angular contact ball
Inner ring defect frequency (Hz)	2625.25
Outer ring defect frequency (Hz)	2074.75
Rolling element defect frequency (Hz)	1747.19
Inner ring rotational speed (Hz)	235.00
Cage rotational speed (Hz)	103.74
Rolling element rotational speed (Hz)	873.60

Output from ATLAS — Copyright © SKF, 1989

Bearing Defect Frequencies at 14,250 RPM

Bearing designation	GE Ceramic
Pitch diameter [dm] (mm)	168
Rolling element diameter [DW] (mm)	22.22
Number of rolling elements [z]	20
Contact angle (degrees)	28.00
Inner ring speed (RPM)	14250
Bearing type code	3
Outer, housing, diameter [D] (mm)	0
Inner, bore, diameter [d] (mm)	133
Number of rows	1
Bearing type	Angular contact ball
Inner ring defect frequency (Hz)	2653.18
Outer ring defect frequency (Hz)	2096.82
Rolling element defect frequency (Hz)	1765.78
Inner ring rotational speed (Hz)	237.50
Cage rotational speed (Hz)	104.84
Rolling element rotational speed (Hz)	882.89

Bearing Defect Frequencies at 14,800 RPM

Bearing designation	GE Ceramic
Pitch diameter [dm] (mm)	168
Rolling element diameter [DW] (mm)	22.22
Number of rolling elements [z]	20
Contact angle (degrees)	28.00
Inner ring speed (RPM)	14800
Bearing type code	3
Outer, housing, diameter [D] (mm)	0
Inner, bore, diameter [d] (mm)	133
Number of rows	1
Bearing type	Angular contact ball
Inner ring defect frequency (Hz)	2755.58
Outer ring defect frequency (Hz)	2177.75
Rolling element defect frequency (Hz)	1833.93
Inner ring rotational speed (Hz)	246.67
Cage rotational speed (Hz)	108.89
Rolling element rotational speed (Hz)	916.97

Output from ATLAS — Copyright © SKF, 1989

Gearmesh Frequencies at 8,700 RPM

Gear designation	na
Pinion (driver) gear [Teeth]	31
Driven gear [Teeth]	184
Calculated gear ratio	5.9355 : 1
Rotational input speed (Hz)	145
Rotational input speed (RPM)	8700
Rotational output speed (Hz)	24.43
Tooth meshing frequency (Hz)	4495
2nd harmonic GMF (Hz)	8990
3rd harmonic GMF (Hz)	13485
4th harmonic GMF (Hz)	17980
Sideband modulation frequencies (Hz)	± n * 145
Tooth repetition frequency (Hz)	0.788

Gearmesh Frequencies at 14,100 RPM

Gear designation	na
Pinion (driver) gear [Teeth]	31
Driven gear [Teeth]	184
Calculated gear ratio	5.9355 : 1
Rotational input speed (Hz)	235
Rotational input speed (RPM)	14100
Rotational output speed (Hz)	39.6
Tooth meshing frequency (Hz)	7285
2nd harmonic GMF (Hz)	14570
3rd harmonic GMF (Hz)	21855
4th harmonic GMF (Hz)	29140
Sideband modulation frequencies (Hz)	± n * 235
Tooth repetition frequency (Hz)	1.277

Gearmesh Frequencies at 14,250 RPM

Gear designation	na
Pinion (driver) gear [Teeth]	31
Driven gear [Teeth]	184
Calculated gear ratio	5.9355 : 1
Rotational input speed (Hz)	237.5
Rotational input speed (RPM)	14250
Rotational output speed (Hz)	40.0
Tooth meshing frequency (Hz)	7362
2nd harmonic GMF (Hz)	14725
3rd harmonic GMF (Hz)	22088
4th harmonic GMF (Hz)	29450
Sideband modulation frequencies (Hz)	± n * 237.5
Tooth repetition frequency (Hz)	1.291

Output from ATLAS — Copyright © SKF, 1989

Gearmesh Frequencies at 14,800 RPM

Gear designation	na
Pinion (driver) gear [Teeth]	31
Driven gear [Teeth]	184
Calculated gear ratio	5.9355 : 1
Rotational input speed (Hz)	246.67
Rotational input speed (RPM)	14800
Rotational output speed (Hz)	41.56
Tooth meshing frequency (Hz)	7647
2nd harmonic GMF (Hz)	15293
3rd harmonic GMF (Hz)	22940
4th harmonic GMF (Hz)	30587
Sideband modulation frequencies (Hz)	$\pm n * 246.67$
Tooth repetition frequency (Hz)	1.341

Output from ATLAS — Copyright © SKF, 1989

GE Ceramic Test Bearing Dimensions (Test RFM L 275669)

Pitch	6.596 inch
Ball	7/8 inch
Angle	28 degrees
Number of Balls	20
Bore	133 mm
Seeded Defect size	Width 0.020 inch Depth 0.010 inch

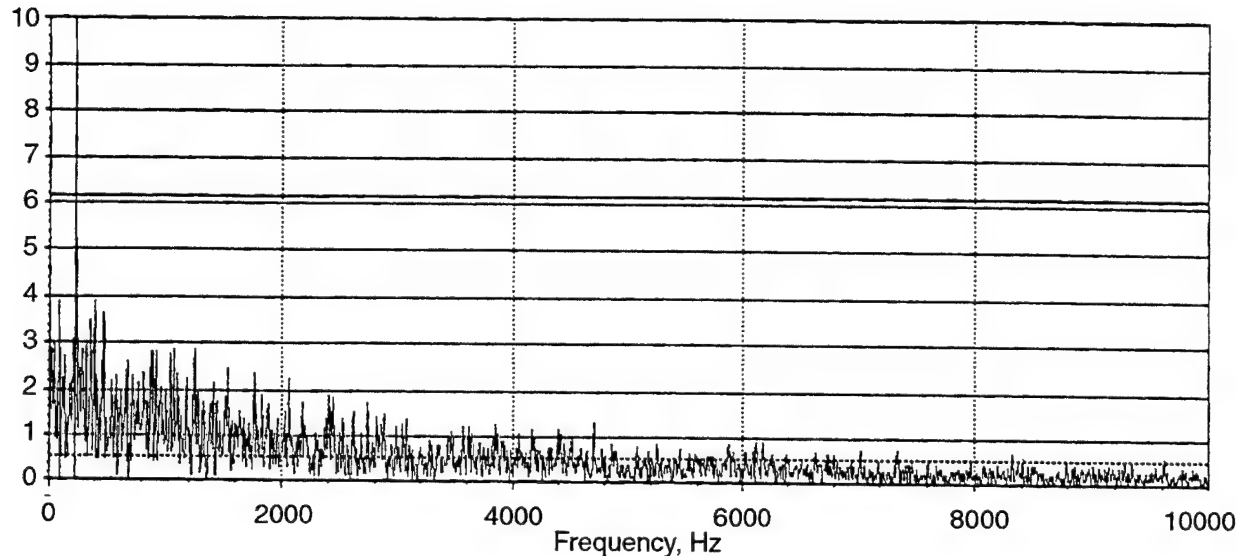
Test Cycle Conditions

Time (min)	Speed (RPM)	Axial Load (lb)
6.5	8,700	900
1.5	14,800	9,000
5.5	14,250	7,000
16.5	14,100	2,500

Examples of Spectrums

During the progress of failures, different phenomena show themselves. Figure 86 indicates overrolling of debris by showing a rather random pattern. Figure 87 shows the opposite, a well-defined peak at the outer-race defect frequency. Figure 88, a time domain plot, shows clearly a modulation pattern related to the rotational speed (234 Hz). Figure 89 shows a moment where the outer-race pattern is dominant, whereas Figure 90 displays a huge amount of rotational speed modulation. Figures 91 and 92 show the same spectrum with different overlaying cursors. Figure 91 displays the rotational speed sideband pattern and Figure 92 the cage defect pattern (the outer-race defect frequency is an integer harmonic of the cage defect frequency). At the later stage of defect development, the rolling element shows up randomly (Figure 93). The randomness of the effect can be explained by the small chance of overrolling a rolling element defect.

Set: Axial Twin GE Type: FTT Date: 17 March 1994 12:03:13
Point ID: Spectral Emitted Energy Axial 10K Desc:
Window: Hanning Lines: 1600 Aver: 1 Freq: 0-10000Hz
Detect: Peak to Peak Speed: 232.99 Threshold: 0.5000 Units: SEEs



Identification of Spectral Peaks Above Threshold

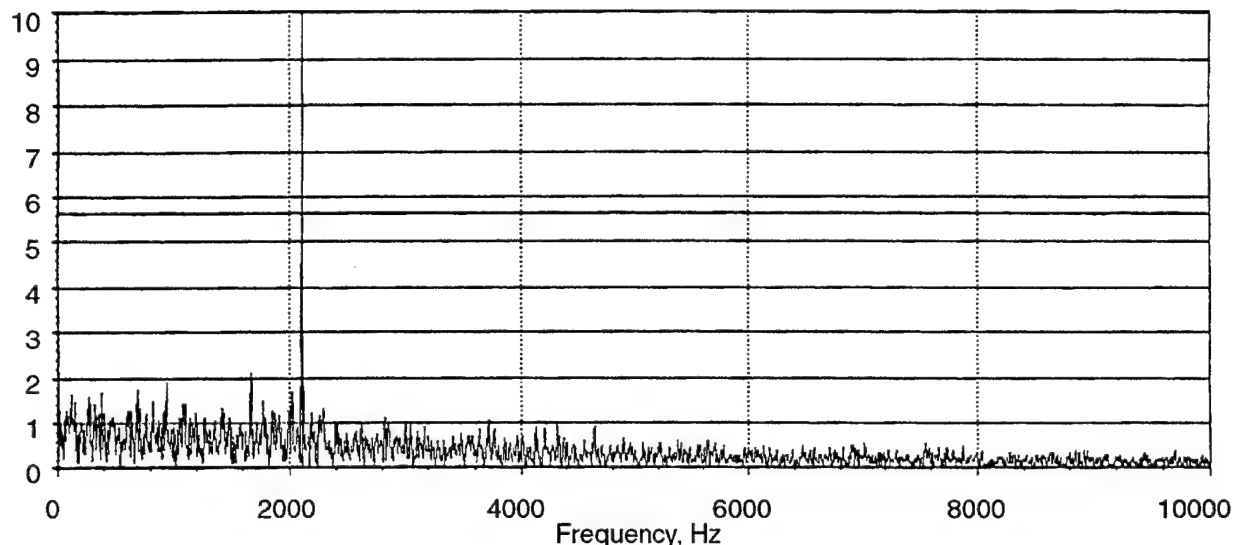
No.	Amp.	Freq.	Order	No.	Amp.	Freq.	Order
1.	3.9124	6.3	0.027	9.	3.4801	362.5	1.556
2.	2.8745	25.0	0.107	10.	3.9066	393.8	1.690
3.	2.9470	43.8	0.188	11.	3.6274	468.8	2.012
4.	3.8793	87.5	0.376	12.	2.8853	887.5	3.809
5.	3.0600	206.3	0.885	13.	2.8182	918.8	3.943
6.	6.0835	231.3	0.993	14.	2.7656	1043.8	4.480
7.	2.8826	287.5	1.234	15.	2.8651	1075.0	4.614
8.	2.9524	325.0	1.395	16.	2.8785	1250.0	5.365

Spectral Energy Summary

Overall	Sync	Subsync	Nonsync
27.24	9.39165	10.0179	23.5257

Figure 86. Single-Spectrum Plot: Frequency = 231.25, Amp = 6.0834 OV, Order = 0,933

Set: Axial Twin GE Type: FTT Date: 17 March 1994 12:21:53
Point ID: Spectral Emitted Energy Axial 10K Desc:
Window: Hanning Lines: 1600 Aver: 1 Freq: 0-10000Hz
Detect: Peak to Peak Speed: 240.00 Threshold: 0.5000 Units: SEEs



Identification of Spectral Peaks Above Threshold

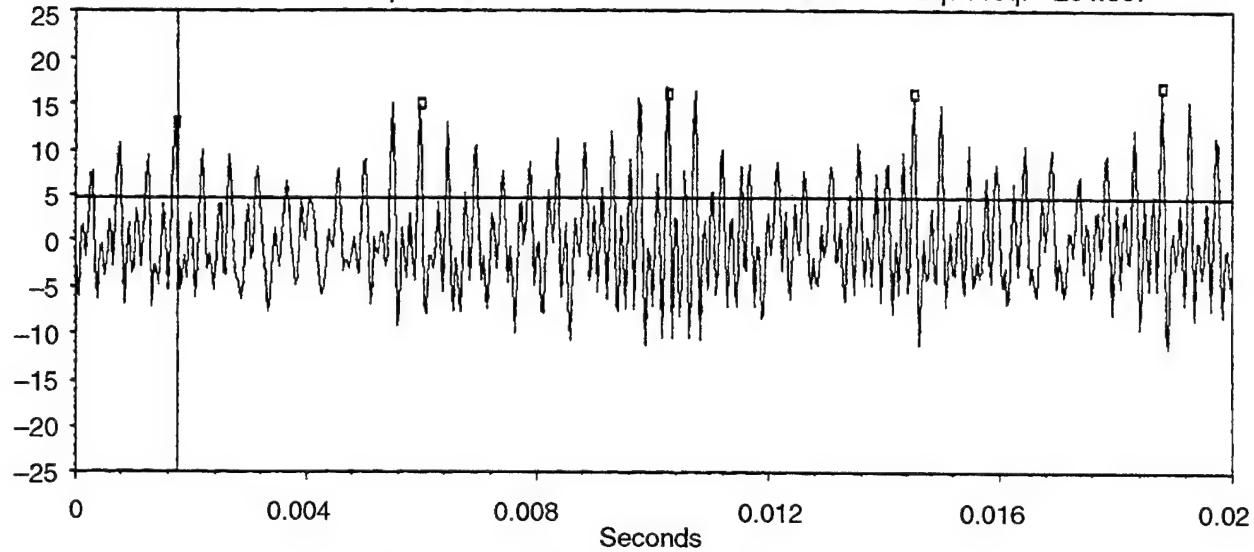
No.	Amp.	Freq.	Order	No.	Amp.	Freq.	Order
1.	1.4398	6.3	0.026	9.	1.8761	937.5	3.906
2.	1.6353	112.5	0.469	10.	1.3990	1081.3	4.505
3.	1.4637	150.0	0.625	11.	1.4162	1100.0	4.583
4.	1.5537	268.8	1.120	12.	2.0852	1662.5	6.927
5.	1.4263	318.8	1.328	13.	1.4479	1762.5	7.344
6.	1.6515	375.0	1.563	14.	1.6977	2018.8	8.411
7.	1.7443	687.5	2.865	15.	5.5838	2106.3	8.776
8.	1.4624	818.8	3.411	16.	1.3339	2293.8	9.557

Spectral Energy Summary

Overall	Sync	Subsync	Nonsync
16.923	4.21046	4.55813	15.7444

Figure 87. Single-Spectrum Plot: Frequency = 2106.25, Amp = 5.5837 OV, Order = 8.776

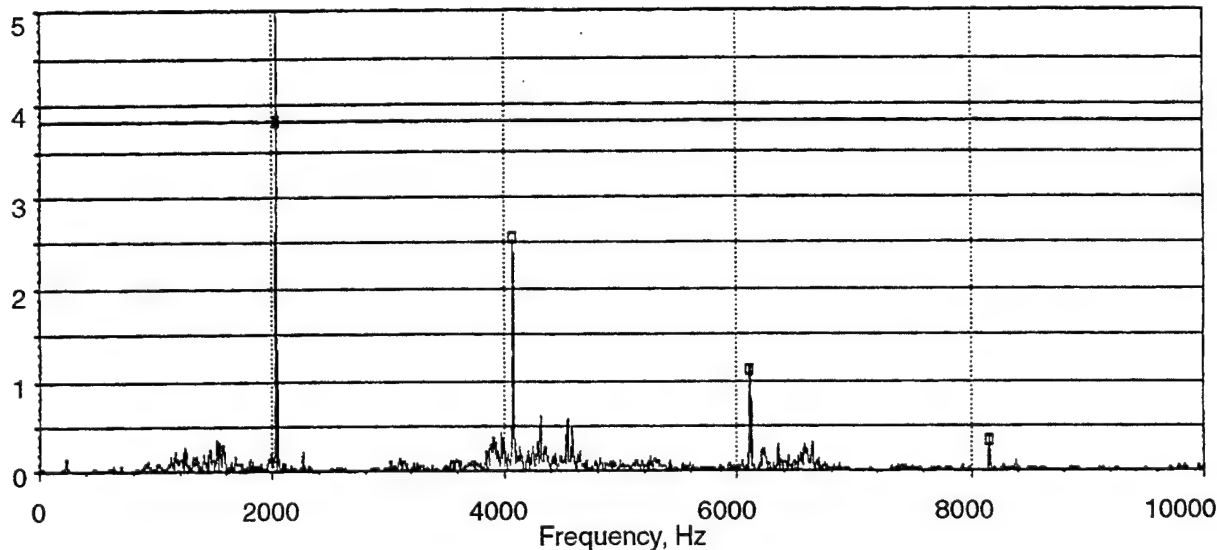
Set: Axial Twin GE Type: Time Record Date: 17 March 1994 12:41:22
 Point ID: Accelerometer Axial 10K Desc:
 Window: Uniform Lines: 4069 Aver: 1 Secs: 0.000–0.160
 Detect: RMS Speed: 0.00 Threshold: 0.0000 Units: Gs
 Secs: 0.00601 Amp: 4.4157 Interval: 0.00425 Eqv Freq: 234.807



Identification of Replicated Interval Markers

No.	Amp.	Seconds	No.	Amp.	Seconds
1.	12.8237	0.00176	26.	-3.6001	0.10823
2.	14.9414	0.00602	27.	-3.7726	0.11249
3.	15.9140	0.01027	28.	1.5922	0.11675
4.	15.7257	0.01453	29.	-0.0078	0.12100
5.	16.5414	0.01879	30.	-0.6196	0.12526
6.	8.7139	0.02305	31.	-1.5294	0.12952
7.	7.0040	0.02731	32.	-2.3451	0.13378
8.	6.6589	0.03157	33.	-6.1099	0.13804
9.	6.1726	0.03583	34.	-5.9687	0.14230
10.	1.8432	0.04009	35.	-6.9727	0.14656
11.	-4.0707	0.04435	36.	-1.5294	0.15082
12.	-1.9059	0.04860	37.	-0.8549	0.15508
13.	-3.3648	0.05286	38.	2.1726	0.15933
14.	-3.5059	0.05712			
15.	-1.4353	0.06138			
16.	3.9608	0.06564			
17.	1.5608	0.06990			
18.	6.8785	0.07416			
19.	2.7687	0.07842			
20.	2.3922	0.08267			
21.	-1.9216	0.08693			
22.	-3.1451	0.09119			
23.	-7.3491	0.09545			
24.	-8.4472	0.09971			
25.	-6.3923	0.10397			

Figure 88. Time Record Plot



Identification of Spectral Peaks Above Threshold

No.	Amp.	Freq.	Order	No.	Amp.	Freq.	Order
1.	0.3436	1525.0	6.602	9.	0.3186	4287.5	18.561
2.	0.3228	1550.0	6.710	10.	0.6027	4312.5	18.669
3.	3.8028	2037.5	8.820	11.	0.5787	4543.8	19.670
4.	0.4113	3912.5	16.937	12.	0.5003	4581.3	19.832
5.	0.3159	3937.5	17.045	13.	1.1699	6118.8	26.488
6.	0.4208	3975.0	17.208	14.	0.3037	6568.8	28.436
7.	0.3753	3993.8	17.289	15.	0.3157	6637.5	28.734
8.	2.5500	4075.0	17.641	16.	0.3659	8156.3	35.308

Spectral Energy Summary

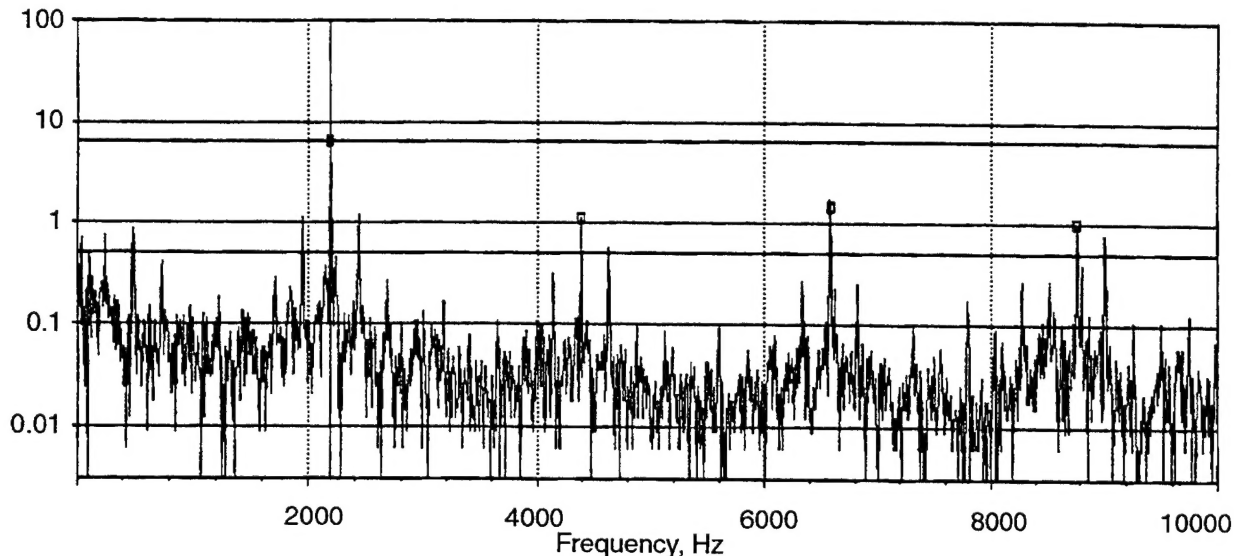
Overall	Sync	Subsync	Nonsync
5.74189	0.671605	0.097599	5.70164

Identification of Harmonic Markers

No.	Amp.	Freq.	Order	No.	Amp.	Freq.	Order
1.	3.8028	2037.5	8.820				
2.	2.5500	4075.0	17.641				
3.	1.0988	6112.5	26.461				
4.	0.3302	8150.0	35.281				

Figure 89. Single-Spectrum Plot: Frequency = 2037.50, Amp = 3.8027, Order = 8.820

Set: Axial Twin GE Type: FTT Date: 17 March 1994 10:18:52
Point ID: Acceleration Enveloping Axial 10K Desc:
Window: Hanning Lines: 1600 Aver: 1 Freq: 0-10000Hz
Detect: RMS Speed: 243.00 Threshold: 0.5000 Units: Gs Env



Identification of Spectral Peaks Above Threshold

No.	Amp.	Freq.	Order	No.	Amp.	Freq.	Order
1.	0.7047	6.3	0.026	9.	0.5620	4631.3	19.059
2.	0.6956	43.8	0.180	10.	1.6559	6575.0	27.058
3.	0.7314	243.8	1.003	11.	1.0186	8768.8	36.085
4.	0.8226	487.5	2.006	12.	0.7603	9012.5	37.088
5.	1.1255	1950.0	8.025				
6.	6.3092	2193.8	9.028				
7.	1.2297	2437.5	10.031				
8.	1.1728	4387.5	18.056				

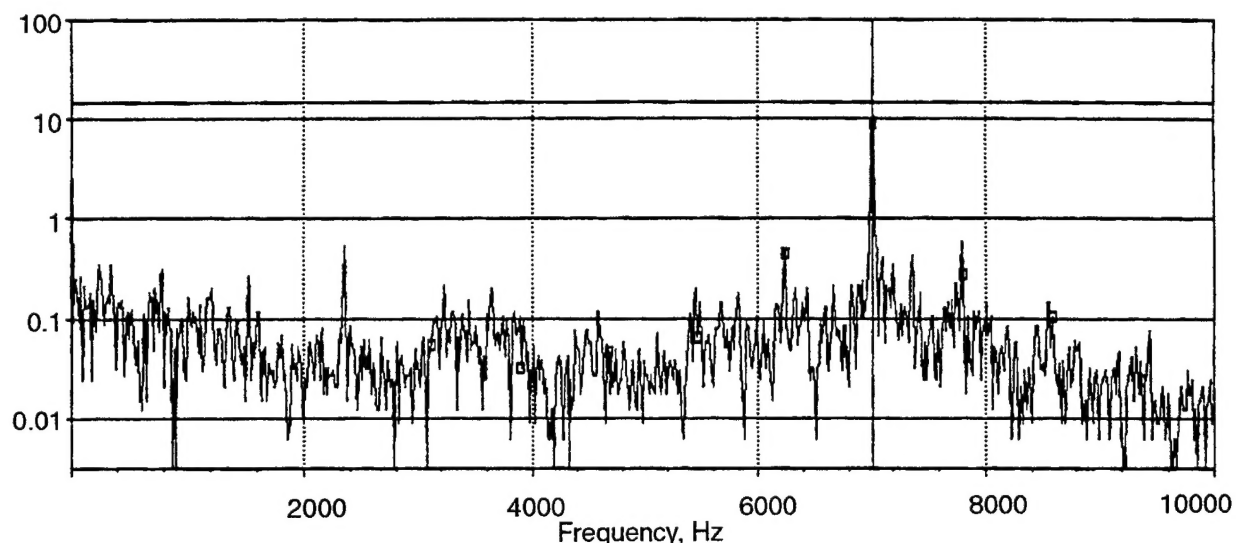
Spectral Energy Summary

Overall	Sync	Subsync	Nonsync
7 8798	6 68269	1 2976	3 96851

Identification of Harmonic Markers

No.	Amp.	Freq.	Order	No.	Amp.	Freq.	Order
1.	6.3092	2193.8	9.028				
2.	1.1728	4385.9	18.049				
3.	1.4660	6578.1	27.070				
4.	1.0186	8768.8	36.085				

Figure 90. Single-Spectrum Plot: Frequency = 2193.75, Amp = 6.3091, Order = 9.028



Identification of Spectral Peaks Above Threshold

No.	Amp.	Freq.	Order	No.	Amp.	Freq.	Order
1.	2.5981	3.8					
2.	14.7620	2103.8					

Spectral Energy Summary

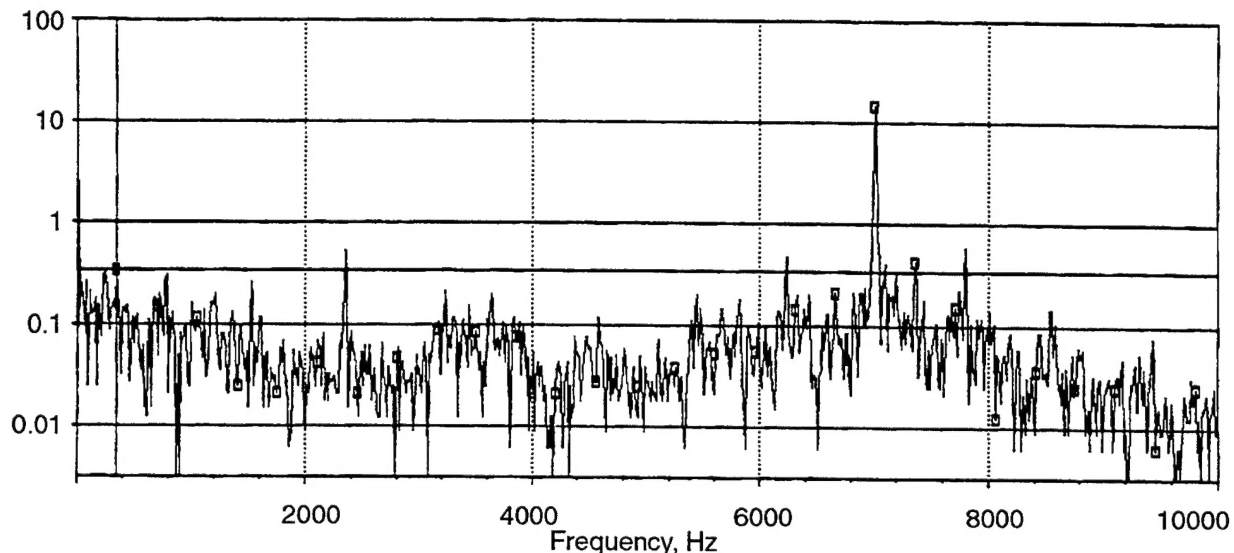
Overall	Sync	Subsync	Nonsync
15.3392	0	0	0

Identification of Harmonic Markers

No.	Amp.	Freq.	Order	No.	Amp.	Freq.	Order
1.	9.3403	2107.5					
2.	0.2784	2342.3					
3.	0.4647	1872.8					
4.	0.1078	2577.0					
5.	0.0686	1638.0					
6.	0.0245	2811.8					
7.	0.0471	1403.3					
8.	1.6275	3046.5					
9.	0.0363	1168.5					
10.	1.6275	3281.3					
11.	0.0578	933.8					

Figure 91. Single-Spectrum Plot: Frequency = 2103.75, Amp = 14.762

Set: Axial Twin GE Type: FTT Date: 17 March 1994 10:20:44
Point ID: Acceleration Enveloping Axial 3K Desc:
Window: Hanning Lines: 800 Aver: 1 Freq: 0-3000Hz
Detect: RMS Speed: 0.00 Threshold: 1.0000 Units: Gs Env



Identification of Spectral Peaks Above Threshold

No.	Amp.	Freq.	Order	No.	Amp.	Freq.	Order
1.	2.5981	3.8					
2.	14.7620	2103.8					

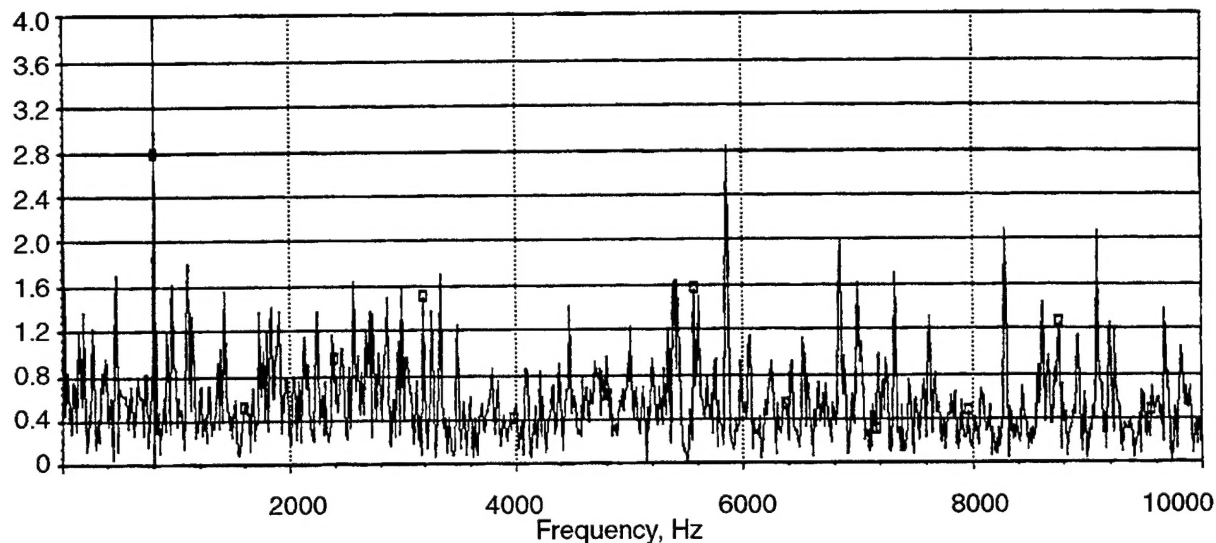
Spectral Energy Summary

Overall	Sync	Subsync	Nonsync
15.3392	0	0	0

Identification of Harmonic Markers

No.	Amp.	Freq.	Order	No.	Amp.	Freq.	Order
1.	0.3412	105.0		14.	0.0245	1471.7	
2.	0.1598	210.1		15.	0.0402	1576.9	
3.	0.1216	315.3		16.	0.0529	1682.0	
4.	0.0245	420.4		17.	0.0559	1787.1	
5.	0.0216	525.5		18.	0.1471	1892.3	
6.	0.0451	630.7		19.	0.2098	1997.4	
7.	0.0225	735.8		26.	0.0265	2733.3	
8.	0.0480	840.9		27.	0.0088	2838.5	
9.	0.0902	946.1		28.	0.0255	2943.8	
10.	0.0882	1051.2					
11.	0.0765	1156.3					
12.	0.0235	1261.5					
13.	0.0284	1366.6					

Figure 92. Single-Spectrum Plot: Frequency = 105.00, Amp = 0.341



Identification of Spectral Peaks Above Threshold

No.	Amp.	Freq.	Order	No.	Amp.	Freq.	Order
1.	2.7486	3.8		9.	1.6304	1620.0	
2.	1.6988	142.5		10.	1.6390	1627.5	
3.	2.7647	240.0		11.	2.8255	1758.8	
4.	1.6160	288.8		12.	2.0174	2055.0	
5.	1.8042	330.0		13.	1.6253	2100.0	
6.	1.6356	768.8		14.	1.7030	2197.5	
7.	1.6074	900.0		15.	2.0961	2486.3	
8.	1.7071	1001.3		16.	2.0821	2726.3	

Spectral Energy Summary

Overall	Sync	Subsync	Nonsync
15.8335	0	0	0

Identification of Harmonic Markers

No.	Amp.	Freq.	Order	No.	Amp.	Freq.	Order
1.	2.7647	240.0		8.	0.5277	1911.3	
2.	0.5064	478.8		9.	0.2980	2150.0	
3.	0.9400	717.5		10.	0.4591	2388.8	
4.	1.5012	956.3		11.	1.2522	2627.5	
5.	0.4017	1195.0		12.	0.4630	2865.0	
6.	0.6101	1433.8					
7.	1.5476	1672.5					

Figure 93. Single-Spectrum Plot: Frequency = 240.00, Amp = 2.7647